

Aus der Klinik für Radiologie
der Medizinischen Fakultät Charité – Universitätsmedizin Berlin

DISSERTATION

Quantification of the biophysical properties of the liver in correlation with
microstructural and vascular changes using multimodal imaging

Quantifizierung der biophysikalischen Eigenschaften der Leber in
Korrelation mit mikrostrukturellen und vaskulären Veränderungen unter
Verwendung multimodaler Bildgebungstechniken.

zur Erlangung des akademischen Grades
Doctor of Philosophy (PhD)

vorgelegt der Medizinischen Fakultät
Charité – Universitätsmedizin Berlin

von

Yasmine Safraou

Datum der Promotion: 28.02.2025

Table of contents

List of tables.....	iv
List of figures.....	v
List of abbreviations	viii
Abstract.....	1
1 Introduction	3
1.1 Historical perspective on diagnostic techniques for hepatic diseases	3
1.2 The emergence of magnetic resonance elastography.....	4
1.3 Hepatic structure	5
1.4 Elucidating liver biophysical properties: previous MRE applications alongside other modalities.....	5
1.5 Study design	6
2 Theory.....	8
2.1 Viscoelastic theory	8
2.2 Electrical analogy	13
2.3 The equation of motion.....	16
2.4 Biphasic poroelasticity in soft liver tissue	18
2.5 Magnetic resonance elastography.....	21
2.6 Diffusion-weighted imaging	24
3 Methods	25
3.1 Animal experiments.....	25
3.1.1. Study 1: Ex vivo liver phantom and fluid inflow preparation	25
3.1.2. Study 2: Rabbit preparation for imaging protocol implementation	29
3.1.3. Study 3: Zebrafish preparation for imaging protocol implementation	29
3.2 Multiparametric MRI and PET measurements.....	30
3.2.1 Study 1: T2-weighted and diffusion-weighted imaging.....	30
3.2.2. Study 2: T1-weighted imaging and PET measurements	30

3.2.3.	Study 3: T2-weighted measurements.....	32
3.3	Multifrequency MRE measurements	33
3.4	Image post-processing	34
3.4.1	Study 1	34
3.4.2	Study 2.....	35
3.4.3	Study 3.....	36
3.5	Post-mortem tissue characterization	37
3.5.1	Study 1: Preparations for macro and microscopic observations.....	37
3.5.2	Study 2: Metabolic characterization of healthy liver samples	37
3.5.3	Study 3: Tissue staining to identify brain subregions and neuroblastoma	38
3.6	Statistical analyses.....	38
3.6.1	Study 1	38
3.6.2	Study 2.....	38
3.6.3	Study 3.....	39
4	Results	40
4.1	mpMRI and multifrequency MRE.....	40
4.1.1	Study 1	40
4.1.2.	Study 2.....	46
4.1.3.	Study 3.....	47
4.2	Post-mortem tissue characteristics.....	49
4.2.1	Study 1: Changes in vascular and extracellular structures under elevated pressure	49
4.2.2	Study 2: Liver stiffness as a potential marker for hepatic metabolic functions.....	49
4.2.3	Study 3: Comparison of high-resolution SWS, φ maps and histology.....	53
4.3	Correlation analyses.....	54
4.3.1	Study 1: Linear mixed model analyses.....	54
4.3.2	Study 2: Correlation of metabolic functions with MRE parameters.....	54

5	Discussion.....	55
5.1	Summary of results	55
5.2	Interpretation of results.....	56
5.2.1	Study 1: The Impact of varied fluid distribution patterns on liver biophysical properties detected through complementary SWS and ADC analysis	56
5.2.2.	Study 2: Metabolic heterogeneity in healthy liver specimen modulates stiffness and viscosity	58
5.2.3.	Study 3: Micromechanical SWS and φ are sensitive to microarchitectural differences constituting the zebrafish brain	60
5.3	Embedding the results into the current state of research	60
5.4	Limitations	64
5.5	Implications for practice and/or future research	64
6	Conclusion	66
	Reference list.....	68
	Statutory declaration.....	75
	Declaration of my contribution to the publications	76
	Publications	79
	List of publications	118
	Curriculum Vitae	120
	Acknowledgments	123

List of tables

Table 1: Rheological models, formulas and schematic representations.....	15
Table 2: All scenarios with liver states, embedding gel consistencies, box dimensions (length (L) x width (W) x height (H)), and inflow solutions utilized for each scenario.....	27
Table 3: MRE hardware and measurement parameters for all studies. SE-EPI stands for spin echo-echo planar.....	33
Table 4: Summary of all baseline values, including group means, standard deviations, and pairwise comparison results for vessel volume, tissue volume, vessel tissue volume fraction (VTVF), apparent diffusion coefficient (ADC) and shear wave speed (SWS) [55] (Table from Safraou <i>et al.</i> (2023)).....	40
Table 5: Values for matrix stiffness (in m/s), fluid dynamic viscosities (η in mPa.s) densities (ρ in kg/m ³) as baseline pressure (0 cmH ₂ O) for all scenarios.....	41
Table 6: Group mean values and standard deviations of vessel volume in cm ³ , tissue volume in cm ³ , VTVF, ADC (with or without vessels) and SWS (with or without vessels) acquired at all static portal pressure levels for all scenarios. p values and effect sizes τ are provided. [55] (Table from Safraou <i>et al.</i> (2023)).....	45
Table 7: The maximum metabolic capacities of fatty acid metabolism and biosynthetic processes in two distinct metabolic clusters of healthy rabbit liver samples. The table presents mean and SD values for various metabolic parameters, along with corresponding p-values indicating significant differences between the two clusters [56].....	52

List of figures

- Figure 1:** (a) Definition of the nomenclature to denote stress tensor elements σ_{ij} . A similar convention is used to represent the strain tensor ϵ_{ij} . The stress and strain symmetric tensors are given as σ_{ij} and ϵ_{ij} . (b) Definition of the nomenclature to illustrate compression and shear strains under compressive or shear forces denoted as F [7] (Figure edited from Hirsch *et al.* (2017)).....10
- Figure 2:** Direct comparison between sinusoidal curves of the purely elastic behavior (red continuous curve) and the purely viscous behavior (blue interrupted curve [7] (Figure edited from Hirsch *et al.* (2017)).....12
- Figure 3:** Poroelastic liver structure. (a) Sketch illustrating the poroelastic nature of the liver, composed of interconnected fluid-filled pores (dark pink) and a solid matrix (light pink). (b) The hepatic lobular structure [10] (Figure inspired from Lorente *et al.* (2020)).....18
- Figure 4:** Stepwise process for generating biomechanical maps for human or animals' liver using multifrequency magnetic resonance elastography (MRE) (Figure inspired from Sack *et al.* [41] (2023)).....23
- Figure 5:** Decolagulation process of the rat liver. (a) Image depicting a bloody liver. (b) Subsequent flushing of blood with a heparinized phosphate buffer saline (PBS) solution resulted in a clean liver appearance. (c) The final image shows the explanted liver with closed vessels except for the cannulated PV (This figure was created specifically for this manuscript).....26
- Figure 6:** Schematic representation of all experimental scenarios: unconfined, confined, confined-fixed and confined-viscous. The illustrations depict differences in inflow solutions, embedding gels and liver states. (b) The technical setup for imaging, conducted on a 3T scanner at room temperature [55] (Figure from Safrdou *et al.* (2023)).....28
- Figure 7:** (a) Experimental setup for healthy liver investigation in female rabbit using 3T PET/MRI (b) Representative MRE magnitude image and wave fields shown at 50 Hz for the three-motion encoding components. PET stands for positron emission

tomography while MRI stands for magnetic resonance imaging [56] (Figure from Shahyari *et al.* (2023)).....31

Figure 8: (a) Setup for zebrafish MRE in a 7T preclinical MRI scanner [57]. (b) The MRE magnitude image is shown in greyscale, while the wave images at 1000, 1200 and 1400 Hz are shown in colour, demonstrating the through-plane wave component encoded by the sequence [57]. (Figure adapted from Jordan *et al.* (2021)).....32

Figure 9: T2 weighted images (T2w), apparent diffusion coefficient (ADC) maps, MRE shear wave field images at 160 Hz and SWS maps, obtained at two portal pressure levels 0 (baseline) and 17.5 cmH₂O, shown for four scenarios [55] (Figure from Safraou *et al.* (2023)).....43

Figure 10: Swarm plots illustrating the evolution of the imaging parameters: (a) vessel tissue volume fraction (VTVF). (b) ADC and (c) SWS over increasing portal pressure (in cmH₂O) of livers in unconfined (green), confined (yellow), confined-fixed (orange), and confined-viscous (blue) [55] (Figure from Safraou *et al.* (2023)).....44

Figure 11: Comparisons between stiff and soft liver groups, with SWS > 1.6 m/s considered as stiff livers, while SWS < 1.6 m/s considered as soft livers. (a) MRE magnitude, and AC PET images with variations in standardized uptake values (SUV). (b) SWS and PR in m/s maps. AC PET stands for attenuated-corrected PET [56] (Figure adapted from Shahyari *et al.* (2023)).....46

Figure 12: From top to bottom, coronal slices of magnitude images, SWS, and phase angle (φ) maps, followed by a lateral view composite microscopy image of the zebrafish [57] (Figure adapted from Jordan *et al.* (2021)).....47

Figure 13: Boxplots of SWS and phase angle (φ) comparisons in (a) and (c), respectively, for skeletal muscle (SM), neuroblastoma (T), and whole brain (B) in transgenic zebrafish. Additionally, (b) and (d) display boxplots of SWS and φ , respectively, comparing group mean values of cerebellum (CB), midbrain (MB), optic tectum (OT), and telencephalon (TC) for the pooled group, including transgenic and wild-type zebrafish [57] (Figure adapted from Jordan *et al.* (2021)).....48

Figure 14: Photos and microscopy images of livers in unconfined, confined, confined-fixed and confined-viscous scenarios. (a) Photographs of livers after mp-MRI

showing the whole liver as well as the cross-sectional area of the median liver lobe. (b) Microscopy images of thin liver pieces (ca. 1 mm) manually sliced from the livers shown in (a), blood vessels are indicated by the arrows, the images were taken at $\times 5$ magnification. Livers in (c) and (d) were processed for histology and stained with Haematoxylin and Eosin (H&E). With $\times 10$ magnification, sinusoids are visible in (c). In (d), the central vein and the surrounding hepatocytes are well depicted with $\times 40$ magnification [55] (Figure from Safraou *et al.* (2023)).....51

Figure 15: (a) Boxplots illustrating significantly different metabolic capacities between the stiff and the soft liver groups. (b) boxplots depicting differences in PR and SWS between stiff and soft liver groups. TAG stands for Triacylglycerol [56] (Figure adapted from Shahryari *et al.* (2023)).....52

Figure 16: Comparison of SWS and φ maps with histology. Tyrosine hydroxylase (TH) and H&E staining highlight cancer tissue in green (TH) and purple (H&E), respectively. [57] (Figure from Jordan *et al.* (2021)).....53

Figure 17: Depicts biological changes occurring across various scales within the liver. [7] (Figure inspired from Hirsch *et al.* (2017)).....63

List of abbreviations

2D	Two-dimensional
3D	Three-dimensional
3T	3-Tesla
7T	7-Tesla
ACAC	Acetylacetone
ADC	Apparent diffusion coefficient
BD	Bile duct
cACLD	Advanced chronic liver disease
CB	Cerebellum
DTI	Diffusion tensor imaging
DWI	Diffusion-weighted imaging
ECM	Extracellular Matrix
FT	Fourier transform
FoV	Field of view
H&E	Hematoxylin and eosin
HA	Hepatic artery
IFP	Interstitial fluid pressure
IVC	Inferior vena cava
k-MDEV	Wavenumber-based multi-frequency dual elasto-visco inversion
LC-MS	Liquid chromatography-mass spectrophotometry
MAFLD	Metabolic-associated fatty liver disease
MB	Midbrain
MDEV	Multi-frequency dual elasto-visco inversion
MEG	Motion encoding gradient

MRE	Magnetic resonance elastography
MRI	Magnetic resonance imaging
Mp-MRI	Multiparametric magnetic resonance imaging
NAFLD/NASH	Non-alcoholic fatty liver disease/non-alcoholic steatohepatitis
NMR	Nuclear magnetic resonance
OT	Optic tectum
PET	Positron emission tomography
PR	Penetration rate
PV	Portal vein
RARE	Rapid acquisition with relaxation enhancement
ROI	Region of interest
SHBC	Suprahepatic vena cava
SM	Skeletal muscle
SNR	signal-to-noise ratio
SWS	Shear wave speed
T1w	T1-weighted
T2w	T2-weighted
TAG	Triacylglycerol
TC	Telencephalon
TE	Echo time
TR	Repetition time
USE	Ultrasound elastography
VLDL	Very Low-density lipoprotein
VTVF	Vessel tissue volume fraction

Abstract

The liver's metabolic function relies on its intricate, fractal matrix architecture with densely packed cells near abundant vasculature. However, the interactions within the liver's solid-fluid compartments, their changes with hemodynamic and metabolic function, and their influence on the coarse-grained biophysical properties of the organ as measured by medical imaging techniques remain poorly understood. To address this gap, we conducted three pre-clinical studies using multi-frequency magnetic resonance elastography (MRE), multiparametric magnetic resonance imaging (mp-MRI), and histological and biochemical tissue characterizations.

Firstly, we investigated hepatic solid-liquid interactions and their impact on liver biophysical properties. Twenty *ex vivo* rat livers were examined by MRE and mp-MRI in four scenarios of liver confinement, tissue crosslinking, and fluid viscosity at different portal pressures (0 to 17.5 cmH₂O). Increased pressure led to significantly higher vessel-tissue volume fraction (VTVF), and water diffusivity, particularly in unconfined livers (VTVF: 300 ± 120 %, $p < 0.05$, water diffusivity: 88 ± 29 %, $p < 0.01$). Hepatic softening was observed in confined and unconfined livers, with and without tissue crosslinking (-12 ± 5 %, $p < 0.05$), while perfusion with high-viscous fluid stiffened the liver (11 ± 4 %, $p < 0.001$).

Secondly, we studied MRE's ability to predict hepatic functional reserve capacity. Nineteen female rabbits were examined using a PET/MRI scanner to quantify hepatic stiffness and viscosity. Proteomics-based modelling assessed the liver's metabolic function. Stiff livers had a low triacylglycerol storage capacity and high glucogenesis and cholesterol synthesis capacities. Soft livers had the opposite profile. Stiffness correlated with glucogenesis ($R = -0.5$, $p < 0.05$), while liver viscosity was associated with urea production ($R = -0.5$, $p < 0.01$) and glutamine exchange ($R = -0.47$, $p < 0.05$). Thirdly, we developed microscopic MRE to investigate the biomechanical properties of healthy and neuroblastoma-bearing zebrafishes with 60 μm in-plane resolution. Using a 7T preclinical scanner, maps of stiffness and fluidity were generated which revealed distinct biomechanical characteristics among different brain subregions and neuroblastoma. Specifically, the midbrain was stiffer than the optic tectum and the telencephalon, while the fluidity of the cerebellum was higher than that of the telencephalon and optic tectum. Neuroblastoma was the softest and the least viscous among all tissues.

Together, the three preclinical MRE-mpMRI studies established the relationship between macroscopic biomechanical properties and structural-functional parameters, such as vascular-fluid properties, metabolic capacities, and microscopic tissue architecture. These findings highlight the sensitivity of biophysics-based imaging to tissue structure-functional properties, essential for developing diagnostic imaging markers for hepatic pathologies and neuroblastoma.

Zusammenfassung

Die Stoffwechselfunktion der Leber hängt von ihrer feinen, fraktalen Matrixarchitektur aus dicht gepackten, von zahlreichen Blutgefäßen versorgten, Zellen ab. Die Wechselwirkungen innerhalb dieser fest-flüssigen Leberkompartimente und ihr Einfluss auf die makroskopischen, biophysikalischen, durch medizinische Bildgebung messbaren Eigenschaften des Organs sind noch unzureichend verstanden. Um diese Wissenslücke zu schließen, führten wir drei präklinische, die Multifrequenz Magnetresonanz-Elastographie (MRE), multiparametrische Magnetresonanztomographie (mp-MRI) sowie histologische und biochemische Gewebecharakterisierungen umfassende Studien durch.

In der ersten Studie untersuchten wir mechanische Wechselwirkungen zwischen den festen und flüssigen Komponenten der Leber und deren Auswirkungen auf die biophysikalischen Eigenschaften. 20 ex vivo Rattenlebern wurden künstlich durchblutet und mittels MRE und mp-MRI, in vier Szenarien mit variiertem Lebereinbettung, Gewebevernetzung, Viskosität des Perfusionsmediums sowie variiertem Portaldruck untersucht. Mit steigendem Druck nahmen, insbesondere bei nicht eingebetteten Lebern, der Gefäß-Gewebe-Volumenanteil (VTVF) und die Wasserdiffusion signifikant zu. In allen Szenarien, außer bei erhöhter Viskosität des Perfusionsmediums, die zu einer Versteifung der Leber führte, wurde eine Lebererweichung beobachtet.

In der zweiten Studie untersuchten wir ob mittels MRE, die funktionelle Reservekapazität der Leber vorhergesagt werden kann. 19 Kaninchen wurden mit einem PET/MRI-Scanner untersucht, um Lebersteifigkeit und -viskosität zu messen. Steife Lebern zeigten eine niedrige Triacylglycerinspeicherkapazität und hohe Glukogenese- und Cholesterinsynthesekapazitäten, während weiche Lebern das gegenteilige Profil aufwiesen. Steifigkeit korrelierte negativ mit der Glukogenese ($R = -0,5$, $p < 0,05$), und Viskosität mit der Harnstoffproduktion ($R = -0,5$, $p < 0,01$) und dem Glutamin-Austausch ($R = -0,47$, $p < 0,05$).

In der dritten Studie entwickelten wir mikroskopische MRE, um die biomechanischen Eigenschaften gesunder und Neuroblastom-befallener Zebrafische zu untersuchen. Mit einem 7T-Scanner wurden hochaufgelöste Steifigkeits- und Fluiditätskarten der Zebrafischhirne erstellt, die unterschiedliche biomechanische Eigenschaften in verschiedenen Hirnsubregionen und bei Neuroblastomen zeigten. Besonders das Mittelhirn war steifer als das optische Tektum und das Telencephalon, während das Kleinhirn eine höhere Fluidität aufwies. Neuroblastome zeigten die geringste Steifigkeit und Viskosität aller untersuchten Gewebe.

Zusammenfassend zeigten die drei präklinischen MRE-mpMRI-Studien, dass makroskopische biomechanische Eigenschaften wie Steifigkeit und Fluidität mit strukturellen und funktionellen Parametern wie Gefäß-Fluidität, Stoffwechselkapazität und mikroskopischer Gewebearchitektur zusammenhängen. Diese Erkenntnisse unterstreichen die Sensitivität und Bedeutung biophysikbasierter Bildgebung für die Entwicklung diagnostischer Marker für hepatische Pathologien und Neuroblastoma.

1 Introduction

1.1 Historical perspective on diagnostic techniques for hepatic diseases

Throughout history, humans have continuously sought to refine diagnostic techniques, such as auscultation, visual observation and manual palpation. Palpation, in particular, has been acknowledged for centuries as a reliable method for detecting superficial abnormalities like nodules and oedema, despite its limitations in reaching deeper tissues [1]. Over the past century, medical imaging has transformed clinical diagnosis by enabling the non-invasive examination of internal tissues and organs. X-ray imaging, ultrasound imaging and computed tomography have granted medical professionals unprecedented insights into organ anatomy and pathology. Concurrently, the discovery of nuclear magnetic resonance (NMR)¹ by Felix Bloch and Edward Purcell in 1940 laid the groundwork for the development of an additional imaging modality: magnetic resonance imaging (MRI) [2].

MRI generates three-dimensional (3D) images of the human body with a greater degree of contrast, allowing for the differentiation of soft tissues, primarily based on their water content. Raymond Damadian's research [3] showcased the utility of tissue proton density and relaxation times in quantifying disparities between microstructurally distinct healthy and tumor tissues [3]. Subsequent advancements continued to refine and expand quantitative imaging methodologies, with techniques such as diffusion-weighted imaging (DWI). The introduction of DWI significantly enhanced the capacity of MRI to detect water mobility within tissues, thereby increasing MRI sensitivity to soft tissue microstructure [4].

The investigation of fibrotic livers by MRI may yield images that appear similar to those of a healthy liver, despite the liver being in advanced disease stages and the presence of underlying microstructural alterations. Consequently, invasive biopsy has been the gold-standard diagnostic tool for many years, enabling the detection and staging of fibrosis. [5, 6]. This highlights the pressing need for the development of a quantitative imaging method that reflects matrix remodelling and tissue alterations across a hierarchy of structural constituents.

¹ In 1940, Felix Bloch and Edward Purcell elucidated the principles of nuclear magnetic resonance (NMR) and demonstrated the impact of radiofrequency pulses on atomic nuclei placed in a magnetic field. This has provided the foundation for magnetic resonance imaging.

The haptic sensations experienced during palpation can be described as either 'soft' or 'stiff' [5]. These diverse tactile perceptions arise from the viscoelastic properties of soft tissues, which are shaped by the hierarchical arrangement of solid and fluid components, along with microstructure. For instance, the sensation of stiffness may be attributed to the abundance of dense collagen fibers in tumors like fibromas, while that of softness could result from fluid accumulation such as in cystic formations. One promising approach to detecting and staging liver disease is the measurement of viscoelasticity, which integrates concepts of elasticity and viscosity, providing a framework for modelling soft tissue responses to external forces. Viscoelastic tissue properties, explicitly depending on soft tissue microstructure, may change with pathological alterations, offering diagnostic potential through comparisons between healthy and diseased tissues. Therefore, magnetic resonance elastography (MRE) was developed as an imaging method for the non-invasive quantification of tissue viscoelastic properties [7, 8].

1.2 The emergence of magnetic resonance elastography

Elastography is based on the following principles: first, applying targeted forces to specific organs or tissues to induce deformation; second, detecting the resulting deformations, typically displacements in the order of micrometer, and third, the reconstruction of maps depicting the viscoelastic properties of the tissue or organ of interest. The applied deformation forces, consisting of time harmonic vibrations that induce shear waves, penetrate organs located deep within the abdominal cavity (e.g. liver and kidneys) or those shielded by bony structures (e.g. brain and heart). The resulting shear wave images are then analyzed to recover the viscoelastic properties of the targeted organ. These properties include the shear wave speed (SWS) which serves as a surrogate for tissue stiffness. Moreover, an assessment of the shear wave's damping properties allows for the estimation of organ inverse viscosity, referred to as the penetration rate (PR).

MRE has emerged as a unique imaging modality for quantifying tissue biomechanical properties. In the liver, MRE was proven effective in staging hepatic fibrosis, revealing a gradual increase in tissue stiffness, concurrent with disease progression [9]. These findings confirmed the sensitivity of MRE to fibrous collagen deposition and alterations in portal pressure, associated with liver fibrosis. Unlike

palpation, MRE is not limited by organ depth and provides quantitative parameters in an image-resolved fashion. Thus, MRE might help to overcome sampling errors of biopsies and avoid repeated invasive examinations for monitoring disease progression.

1.3 Hepatic structure

The liver carries out vital metabolic functions that are reflected in its unique tissue architecture. The liver is perfused by two blood inlets: the hepatic artery (HA), which supplies the liver with nutrient-rich, oxygenated blood at systolic pressure; and the portal vein (PV), which delivers deoxygenated blood at hydrostatic pressure. The inferior vena cava (IVC) acts as the main vessel through which deoxygenated blood exits the liver. Both hepatic inputs converge in the sinusoidal channels, which permeate the entirety of the liver's micro-structure and facilitate the exchange of nutrients between the blood and the hepatocytes. These exchanges drive the metabolic functions within hepatocytes including the regulation of plasma metabolites (e.g. glucose, amino acids and lipoproteins), the detoxification of metabolic end products (e.g. ammonia, urea) and the storage of nutrients (e.g. glycogen, triacylglycerol) [10-12]. Liver lobules, which form hexagonal units, represent the liver's functional unit. They are comprised of sinusoids and hepatocyte cords and are supplied by portal triad structures typically composed of an HA, PV, and bile duct (BD), irrigating the lobule from its vertices and converging towards the center [10-13]. The hepatic architecture could be compared to a poroelastic system. Its solid matrix (hepatocytes, cytoskeleton and extracellular matrix) and fluid component (blood and extracellular fluid) interact on multiple scales to shape the global biophysical properties of the organ [14, 15].

1.4 Elucidating liver biophysical properties: previous MRE applications alongside other modalities

MRE, particularly when paired with multiparametric magnetic resonance imaging (mp-MRI) has shown great potential in diagnosing diffuse liver diseases [16-19]. For instance, hepatic biomechanical properties were demonstrated to be sensitive to changes in cellular matrix composition due to inflammation [20, 21], fat accumulation [22, 23] and fibrosis [16-18, 20, 24-27]. Moreover, hepatic stiffness showed sensitivity to alterations in cellular and stromal integrity [28, 29] extending beyond markers of steatohepatitis and fibrosis. Changes in the fluid component, such as variations in

hydration [28, 29], prandial states [30] and portal pressures [31, 32] have also been shown to influence hepatic stiffness. Furthermore, it was observed that increased portal pressure due to portal hypertension leads to vessel dilation, exerting compression onto the surrounding matrix and resulting in compression stiffening [33]. Prior research using ultrasound elastography (USE) has indicated a potential connection between metabolism and biomechanical properties in cancer patients [34]. On a microscopic scale, it was found that hepatic biomechanical properties are responsive to tissue heterogeneity and single-cell stiffness [35-37].

1.5 Study design

The impact of short-term physiological changes, such as fluctuations in hepatic portal pressure, and long-term metabolic changes on liver stiffness and viscosity, as measured by MRE, remains poorly understood. We hypothesize that MRE is sensitive to alterations in hepatic portal pressure and metabolism. Furthermore, we propose that MRE may be used at different scales, ranging from tens of micrometers to millimeters in image voxel sizes, providing the opportunity to examine soft tissue biomechanical properties across multiple species at high specificity. To address this hypothesis, we designed three preclinical studies aimed at identifying and dissecting the effects of hemodynamics, metabolism, and microstructure on the biomechanical properties of the liver:

- **Study 1:** The influence of static portal pressure on liver biophysical properties

The main purpose of study 1 was to assess the impact of factors associated with poroelastic interactions on the macroscopic biomechanical liver properties. These factors were portal pressure, blood viscosity, organ confinement and tissue crosslinking. This study consisted of four different experimental scenarios designed using ex vivo rat livers to mimic different hepatic pathophysiology. Our specific objectives within this study were:

- (1) To investigate the impact of increasing portal pressure on the biophysical properties of the liver utilizing MRE in combination with diffusion-weighted imaging (DWI).
- (2) To explore the association of macroscopic biophysical imaging parameters and the hepatic microstructure through detailed histology analysis.

(3) To study the influence of interstitial fluid pressure (IFP) on liver biomechanical properties by alteration of the fluid distribution between solid and liquid compartments.

- **Study 2:** On the relationship between metabolic capacities and in vivo viscoelastic properties of the liver

Study 2 was based on the observation that early stages of non-alcoholic fatty liver disease are often associated with metabolic disruptions, which do not necessarily progress to structural abnormalities [38, 39]. Given the limited information on potential associations between hepatic functions and MRE parameters, study 2 aimed to investigate specific metabolic functions that might impact viscoelastic parameters in the healthy liver, thereby aiding in early disease detection. Our objective was threefold:

- (1) To establish a standardized imaging protocol for measuring the in vivo rabbit livers using a hybrid PET/MRI scanner.
- (2) To assess metabolic heterogeneity in healthy rabbit livers by a proteomics-based computational analysis of metabolic capacities.
- (3) To investigate the relationship between specific metabolic functions and their potential impact on liver viscoelastic parameters, as measured by MRE.

- **Study 3:** Microscopic multifrequency MR elastography for mapping viscoelasticity in zebrafish

Study 3 aims to examine the sensitivity of macroscopic viscoelastic properties, as measured by MRE, to different organ subregions characterized by their distinct microarchitecture. The primary goal was to optimize MRE parameters to approach a microscopic viscoelastic mapping resolution, allowing for an improved characterization of the microstructural variability. To achieve this, we investigated the zebrafish, exploiting its optical transparency for high-resolution imaging, and the availability of a neuroblastoma-bearing transgenic strain allowing comparative analyses between healthy and tumor tissues. Within this study, we outlined three specific objectives.

- (1) To establish an MRI/MRE experimental setup and imaging protocol to scan adult zebrafish.
- (2) To generate near-microscopic biomechanical maps with in-plane resolution similar to histology images, providing initial reference values of the viscoelastic properties of zebrafish muscles, brain subregions and neuroblastoma.
- (3) To explore the relationship between diverse microarchitectures within different brain subregions and their impact on macroscopic biophysical imaging parameters.

2 Theory

The following section details the theoretical framework underlying our three studies. It will cover viscoelastic and poroelastic theories, followed by an exploration of the fundamental principles of MRE.

2.1 Viscoelastic theory

Soft materials exhibit complex responses to external, time-dependent forces, governed by two fundamental physical properties: elasticity and viscosity. The interaction between an object and external forces can be elucidated in terms of 'stress' and 'strain'. Stress refers to the force applied to an object's surface, while strain represents the resulting deformation. Both stress and strain are quantifiable variables [8]. Stress is defined as the external force per unit area acting on an infinitesimal surface at a given point. In its tensorial form, stress is expressed in a cartesian coordinate system by nine components σ_{ij} , where $(i, j) \in (1, 2, 3)$. Each stress component is calculated as:

$$\sigma_{ij} = \frac{F_i}{A_j} \quad (1)$$

Where F_i is the applied force in the direction of i in Newtons (N) and A_j is the area (m^2) subjected to the applied force. Stress components may be classified as either diagonal elongation components ($i = j$), or off-diagonal, shear components ($i \neq j$). The stress tensor σ is symmetric ($\sigma_{ij} = \sigma_{ji}$) [8, 40].

Strain refers to the deformation of a continuous medium, characterized by the displacement field u . In simpler terms, each point r undergoes a positional shift within infinitesimal distances, thereby acquiring a new position $r' = r + u(r)$.

The deformation of a purely elastic solid is a fully reversible phenomenon: Once the external force is removed, the material regains its original shape without any energy dissipation. In the one-dimensional case, a purely elastic deformation σ_e can be modelled as a massless spring, where stress and strain are related as follows:

$$\sigma_e = E \epsilon \quad (2)$$

E symbolizes Young's modulus whereas ϵ denotes the strain. Under the principle of Cauchy deformation, strain changes relatively to the initial length of the spring L_0 , such that:

$$\epsilon = \frac{\Delta L}{L_0} \quad (3)$$

In three-dimensional objects and similar to the stress tensor, the strain tensor ϵ may be decomposed into diagonal components ($i = j$) representing elongation, compression or volumetric deformation; and off-diagonal components ($i \neq j$) depicting shear deformation with volume preservation. The strain tensor, like the stress tensor, is symmetric ($\epsilon_{ij} = \epsilon_{ji}$). In a linear elastic material, the Hooke's law models the relationship between all stress and strain components as follows:

$$\sigma_{ij} = \sum_{k,l=1}^3 \mathbf{C}_{ijkl} \epsilon_{kl} \quad (4)$$

According to this relationship, the stress σ_{ij} is a linear function of the strain ϵ_{kl} . \mathbf{C} is the elasticity tensor, initially composed of 81 independent elements. Under the assumption of intrinsic symmetries between the stress and strain tensors ($\mathbf{C}_{ijkl} = \mathbf{C}_{jikl} = \mathbf{C}_{ijkl}$), and the consequent symmetry within the elasticity tensor itself, \mathbf{C} reduces to 21 independent elements. Moreover, under the additional assumption of isotropy, the Hooke's law may be simplified in terms of the Lamé first and second constants, respectively λ and μ :

$$\sigma_{ij} = \lambda \theta \delta_{ij} + 2 \mu \epsilon_{ij} \quad (5)$$

Where δ_{ij} ² is the Kronecker delta and θ ³ is the volumetric strain ($\frac{dV}{V}$) [8, 41]. The parameter μ , synonymous with the shear modulus, quantifies the material's resistance to simple shear strain. Another important parameter is the compression

² $\delta_{ij} = 1$ for $i = j$; $\delta_{ij} = 0$ for $i \neq j$

³ $\theta = \epsilon_{11} + \epsilon_{22} + \epsilon_{33}$

modulus (K), which measures a material's ability to resist uniform compression in the form of isotropic pressure. The compression modulus may be expressed as $K = -\frac{p}{\theta}$, where p is the isotropic pressure [8, 41, 42]. Figure 1.a shows the elements of the stress tensor in a cartesian coordinate system, while figure 1.b illustrates the distinction between compression and shear deformation on a 3D cubic object [43].

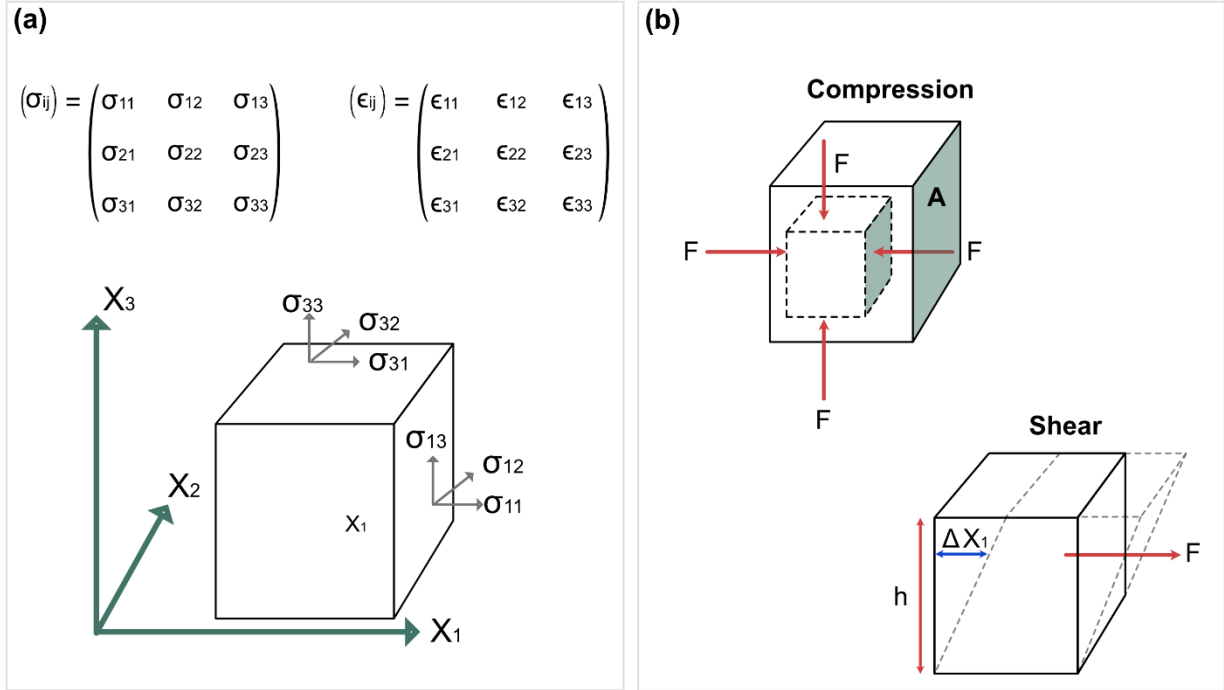


Figure 1: (a) Definition of the nomenclature to denote stress tensor elements σ_{ij} . Similar convention is used to represent the strain tensor ϵ_{ij} . The stress and strain symmetric tensors are given as σ_{ij} and ϵ_{ij} . (b) Definition of the nomenclature to illustrate compression and shear strains under compressive or shear forces denoted as F [8] (Figure edited from Hirsch *et al.* (2017)).

Given our focus on incompressible soft tissue consisting mostly of water (75%) [41, 44], the deformation becomes nearly solely dependent on the shear stress ($\theta \rightarrow 0$, $K \rightarrow \infty$). This simplifies the Hooke's law to:

$$\sigma_{ij} = 2\mu\epsilon_{ij} \quad (6)$$

Unlike purely elastic solids, purely viscous objects retain their deformation and do not return to their original shape when the external force is withdrawn. Friction between material layers during deformation converts mechanical energy into irreversibly dissipated thermal energy. This behavior is represented by a dashpot,

which consists of a piston submerged in a viscous fluid that exerts restraining forces as the piston travels. In purely viscous materials, the stress σ_v and strain rate ($\dot{\epsilon} = \frac{d\epsilon}{dt}$) are related by Newton's viscosity law [8]:

$$\sigma_v = \eta \dot{\epsilon} \quad (7)$$

Here, η is a quantitative representation of the fluid's viscosity, an intrinsic fluid property. $\dot{\epsilon}$ is also referred to as deformation velocity.

In real life, soft tissues exhibit simultaneously linear elastic and purely viscous properties, hence described as "viscoelastic": When an external load is applied, a viscoelastic object deforms and, upon load removal, the object gradually returns back to its original shape. However, a complete shape recovery is normally hindered by the viscous component [8].

Under oscillatory load, the time-harmonic shear stress can be modelled as a sinusoidal function of time with an angular frequency $\omega = 2\pi f$. Due to the proportional relationship between shear stress and strain, the strain can also be expressed as a sinusoidal function of time, lagging behind the stress with a phase shift ϕ . The complex representation of both the stress and strain yields:

$$\sigma^* = \sigma_0 e^{i(\omega t + \phi)} \quad (8)$$

$$\epsilon^* = \epsilon_0 e^{i\omega t} \quad (9)$$

σ_0 and ϵ_0 being the amplitudes of shear stress and strain respectively and $i = \sqrt{-1}$. In the context of the Laplace domain, the parameter $\overline{G^*}$ represents the complex shear modulus, which is the ratio of the Laplace transforms of the stress $\overline{\sigma}(s)$ to the strain $\overline{\epsilon}(s)$:

$$\overline{G^*} = \frac{\overline{\sigma}(s)}{\overline{\epsilon}(s)} \quad (10)$$

G^* serves as a unified measure of the viscous and elastic properties of a homogenous isotropic material. To reach a frequency-resolved form of the complex shear modulus, (s) can be substituted by $i\omega$ and G^* can be further expressed as [8]:

$$G^* = \frac{\sigma_0 e^{i(\omega t + \phi)}}{\epsilon_0 e^{i\omega t}} = \frac{\sigma_0}{\epsilon_0} e^{i\phi} \quad (11)$$

$$G^* = \frac{\sigma_0}{\epsilon_0} (\cos \phi + i \sin \phi) = \frac{\sigma_0}{\epsilon_0} \cos \phi + i \frac{\sigma_0}{\epsilon_0} \sin \phi$$

$$G^* = G' + i G'' = |G^*| \cdot e^{i\phi} \quad (12)$$

We identify from equation (12), two distinct components within the complex shear modulus: G' the storage modulus or elastic modulus, and G'' the loss modulus, or the viscous modulus. $|G^*|$ is calculated as $|G^*| = \sqrt{G'^2 + G''^2}$ and represents the magnitude of the complex shear modulus. ϕ is the phase of the complex shear modulus and varies in the range of $[0, \frac{\pi}{2}]$. For $\phi = 0$, $G'' = 0$, yielding a real-valued G^* associated with a purely elastic solid. Conversely, for $\phi = \frac{\pi}{2}$, $G' = 0$, resulting in a complex-valued G^* associated with a purely viscous fluid. ϕ is calculated as [8] :

$$\phi = \tan^{-1} \frac{G''}{G'} \quad (13)$$

Figure 2 below depicts the response of a viscoelastic material to a shear stress, and the resulting shear strain sine curves of a purely elastic solid and a purely viscous fluid [8, 41, 45].

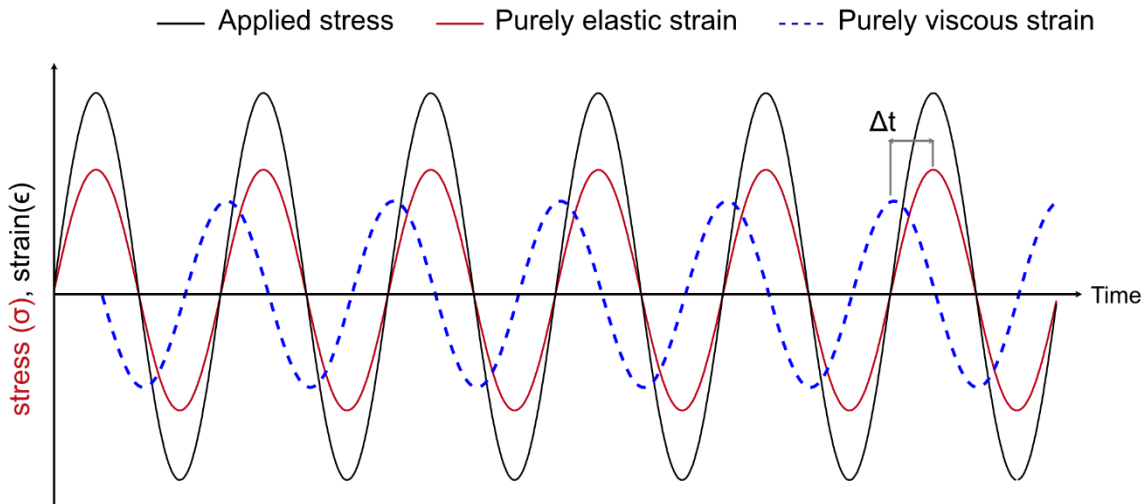


Figure 2: Direct comparison between sinusoidal curves of the purely elastic behavior (red continuous curve) and the purely viscous behavior (blue interrupted curve). The purely elastic behavior exhibits no phase shift between the preset and response sine curves, while the purely viscous behavior displays a phase shift between the two curves [8] (Figure edited from Hirsch *et al.* (2017)).

2.2 Electrical analogy

In the previous section, we discussed modelling a purely elastic solid as a massless spring, yielding the relation $G' = \mu$ where the purely elastic, complex shear modulus is independent of frequency. Conversely, a dashpot is commonly used to model purely viscous fluids. For time-harmonic excitation with an angular frequency ω and an amplitude ϵ_0 , the deformation is $\epsilon = \epsilon_0 e^{i\omega t}$ and the strain rate reads as $\dot{\epsilon} = i\omega\epsilon$. Consequently, the stress-strain relationship may be re-written as:

$$\sigma_{ij} = 2\eta i\omega\epsilon_{ij} \quad (14)$$

The complex shear modulus for a purely viscous fluid G'' can be expressed as frequency-dependent parameter: $G'' = i\omega\eta$.

To effectively model the viscoelastic properties of soft biological tissues, it is essential to combine the features of springs and dashpots into a unified model. Like components in electrical circuits, these mechanical elements can be assembled either in series or parallel. The Maxwell model stands for the arrangement of spring and dashpot elements in series. In this configuration, the total strain is equivalent to the sum of partial individual strains across all circuit elements. The stress-strain relation gives:

$$\epsilon_{ij} = \epsilon_{ij,el} + \epsilon_{ij,vis} \quad (15)$$

$$\epsilon_{ij} = \frac{\sigma_{ij}}{2} \left(\frac{1}{G'} + \frac{1}{G''} \right) \quad (16)$$

And the complex shear modulus for the Maxwell model is:

$$G_M^* = \frac{i\omega\eta\mu}{i\omega\eta + \mu} \quad (17)$$

The Maxwell model is more akin to a viscous fluid than a solid medium since it displays greater loss modulus at low frequencies.

Another model depicts the arrangement in parallel of spring and dashpot elements: the Kelvin Voight model. Following this configuration, the total stress equals the sum of partial stresses across the model.

$$\sigma_{ij} = \sigma_{ij,el} + \sigma_{ij,vis} \quad (18)$$

$$\sigma_{ij} = G' + G'' \quad (19)$$


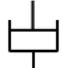

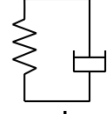

Consequently, the complex shear modulus of this model is:

$$G_{KV}^* = \mu + i \omega \eta \quad (20)$$

While the Kelvin-Voigt model provides a more precise representation of viscoelastic solid behavior, it does not account for frequency dependence in the storage modulus, commonly found in soft biological tissues.

Other models use several spring and dashpot elements arranged in more elaborate configurations to represent the complex interactions between elastic and viscous components [8, 46]. Previously mentioned models in addition to other rheological models of interest are shown in Table 1.

Table 1: Rheological models, formulas and schematic representations.

Rheological model	G^* formula	Schematic
Spring (Hookean)	μ	
Dashpot (Newtonian)	η	
Kelvin-Voigt	$\mu + i \omega \eta$	
Maxwell	$\frac{i \omega \eta \mu}{i \omega \eta + \mu}$	
Springpot	$\mu^{1-\alpha} \eta^\alpha (i \omega)^\alpha$	

2.3 The equation of motion

In the context of time-harmonic motion, the Navier equation is derived by merging the expressions for axial and shear stresses, given by

$$\sigma_{ii} = \sum_{k=1}^3 \left(K - \frac{2}{3} \mu \right) \epsilon_{kk} + 2 \mu \epsilon_{ii} \text{ and } \sigma_{ij} = 2 \mu \epsilon_{ij} \text{ respectively.}$$

These stress components are multiplied by the Kronecker symbol δ and then substituted into the balance momentum equation [8]. The assumption of local homogeneity eliminates the spatial derivatives of μ and K , simplifying the Navier equation to its version for isotropic homogeneous solids to:

$$\rho \ddot{\mathbf{u}} = \left(K + \frac{4}{3} \mu \right) \nabla(\nabla \cdot \mathbf{u}) - \mu \nabla \times (\nabla \times \mathbf{u}) \quad (21)$$

Equation (21) is a second-order partial differential equation describing the displacement field. The algebraic Helmholtz decomposition separates the three-dimensional motion field into two distinct terms: A longitudinal curl-free $\nabla(\nabla \cdot \mathbf{u})$ term, and transversal divergence-free $(\nabla \times \mathbf{u})$ term. When applied to the Navier equation, this decomposition unveils fundamental characteristics of wave propagation within the material, elucidating two distinct types of motion: c_{\perp} , representing transversely polarized, divergence-free waves associated with shear motion; and c_{\parallel} , longitudinally polarized, curl-free wave component depicting compression. For a viscoelastic medium, the wave equation of c_{\perp} can be expressed in terms of the complex shear modulus G^* :

$$\ddot{\mathbf{u}} - \frac{G^*}{\rho} \Delta \mathbf{u} = 0 \quad (22)$$

According to the standard wave equation and equation (22), the following calculation of shear wave velocity is then possible:

$$\text{SWS} = \sqrt{\frac{\mu}{\rho}} \quad (23)$$

With ρ^4 the mass density for soft tissue, we introduce SWS and PR as:

$$\text{SWS} = \frac{1}{\text{Re} \left(\sqrt{\frac{\rho}{G^*}} \right)} = \sqrt{\frac{2|G^*|}{\rho \cdot (1 + \cos \varphi)}} \quad (24)$$

$$\text{PR} = \frac{1}{2\pi} \sqrt{\frac{2|G^*|}{\rho \cdot (1 - \cos \varphi)}} \quad (25)$$

SWS (m/s) serves as a surrogate for tissue stiffness, hence an increase in SWS corresponds to a stiffer material. PR (m/s) surrogates for inverse viscosity, meaning that a higher PR indicates a less viscous medium. Furthermore, φ in equation (13) provides a measure for medium fluidity. These parameters are crucial in describing the viscoelastic behavior of soft tissue with varying constitutions. They can be frequency-dependent.

⁴ For liver tissue, $\rho = 1000 \text{ Kg/m}^3$

2.4 Biphasic poroelasticity in soft liver tissue

Due to its structure, the liver can be described using a biphasic poroelastic model. This model captures its mechanical response to loading while accounting for fluid pressure and viscosity, pore size and pore permeability [10, 11, 33, 47].

The poroelastic medium is defined by a biphasic structure comprising a solid matrix permeated by a fluid-filled pore space. In biological tissues, the solid compartment typically consists of cells or ECM, while the fluid compartment is often represented by the vascular tree and the interstitial fluid. The lumped poroelastic model simplifies this system by assuming that all fluids within the fluid compartment are collectively represented as a single entity, while the solid compartment includes all structural elements. At each infinitesimal point within the poroelastic material, there exists either the solid or the fluid component such as $V = V_s + V_f$.

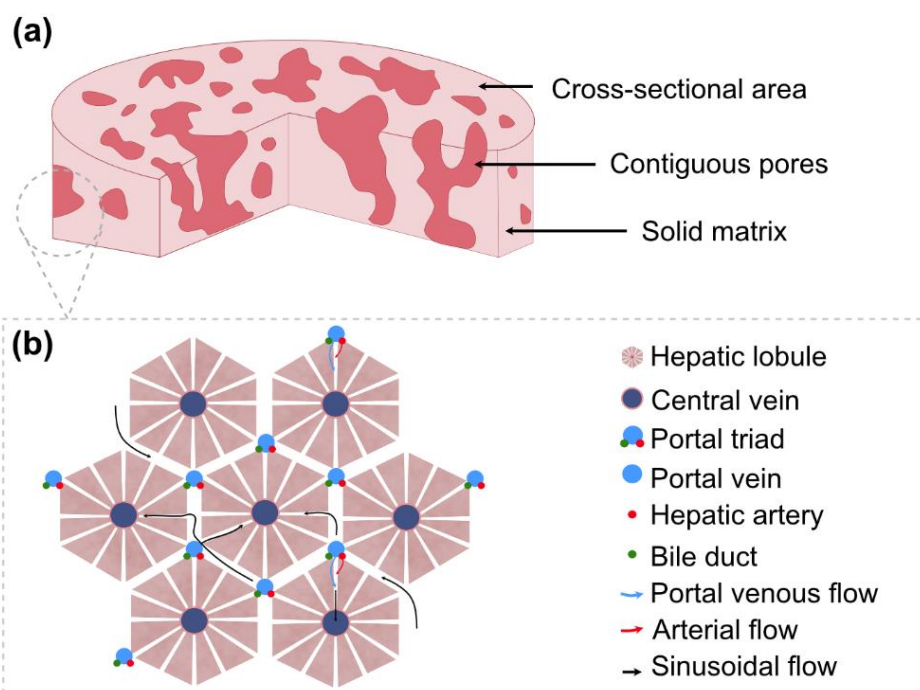


Figure 3: Poroelastic liver structure. (a) Sketch illustrating the poroelastic nature of the liver, composed of interconnected fluid-filled pores (dark pink) and a solid matrix (light pink). (b) Hepatic lobular structure consisting of hepatocytes (light pink) vascularized with the portal triad (the hepatic artery (HA) is represented in red, the portal vein (PV) in cyan blue, the bile duct (BD) in green and the central vein in purple). The Hepatocytes within one lobule receive nutrient-rich blood flow through the sinusoidal structure (in white). The fluid motion within one lobule is depicted by arrows in red and cyan blue, while interlobular fluid exchanges are represented by black arrows [10] (Figure inspired from Lorente *et al.* (2020)).

In a poroelastic medium in equilibrium, the porosity parameter β , which represents the volume ratio occupied by the fluid compartment, describes the distribution of both fluid and solid compartments such as:

$$\beta = \frac{V_f}{V} \quad (26)$$

Where V_f is the volume of the fluid compartment, and V is the total volume. Because of material continuity, the volume ratio of the solid compartment can be calculated as $1 - \beta$ [8, 41].

Both compartments of the poroelastic object are considered purely elastic with real-valued moduli. They are assumed to deform independently. However, their deformation fields are coupled. Moreover, in soft tissue, the fluid is assumed to be highly incompressible ($K_f \rightarrow \infty$) and less prone to shear deformation compared to the solid, cellular and cytoskeletal structure ($\mu_f \ll \mu_s$). Consequently, the poroelastic response to external pressure may be dictated by the solid compartment's response [48, 49]. Using the above, the linear stress-strain relationship can be described by Hooke's law as follows:

$$\sigma_{ij} = M_{ijkl} \epsilon_{kl} - \alpha_{ij} p \quad (27)$$

M_{ijkl} and α_{ij} are constitutive Hookean constants. The pore pressure is denoted by the dynamic variable p . In the drained or relaxed scenario, where excess pore pressure is dissipated ($p = 0$), equation (27) could be simplified to the following [49]:

$$\sigma_{ij} = M_{ijkl} \epsilon_{kl} \quad (28)$$

When investigating the biomechanical properties of soft tissues like the liver, the choice between viscoelastic and poroelastic models depends on the specific mechanisms under investigation. Viscoelastic models capture tissue response to shear stress, accounting for energy storage and dissipation, thereby offering a nuanced understanding of tissue behavior over time. Conversely, poroelastic models are valuable for exploring the interaction between solid and fluid compartments in porous tissues with significant fluid content, shedding light on how mechanical

loading influences fluid flow and distribution. For example, in study 1, we will utilize the viscoelastic model to analyze time-dependent behavior under shear stress, while also considering the liver's poroelastic properties [8, 15, 41, 42, 50].

2.5 Magnetic resonance elastography

Magnetic resonance elastography (MRE) allows the non-invasive, multiscale mapping of viscoelastic parameters in soft biological tissues. As introduced in previous sections, MRE replaces traditional palpation with acoustic waves propagating into the region of interest and offers an examination of the deep-seated organs with higher sensitivity to microstructural and hemodynamic alterations. It is based on three main principles: excitation of the region of interest, motion encoding, and the reconstruction of parameter maps [19, 42].

Acoustic excitation of the region of interest can be achieved using either compressed air drivers in clinical settings or piezoelectric drivers in preclinical settings, particularly for small animals. The use of piezoelectric drivers can extend the frequency range applied in smaller preclinical experiments. MRE is achieved by applying harmonic mechanical vibrations at different frequency and amplitude combinations, with higher frequencies coupled to higher amplitudes. The recommended frequency range for measuring liver in human subjects is typically between 30 and 50 Hz. However, for animals as small as rats, mice, or zebrafish, the frequency range may be extended to 1400 Hz to generate shorter wavelengths [1, 42, 51].

The Motion Encoding Gradient (MEG), which can take a multitude of forms, can be used to encode time-harmonic motion. Static offset phases, particle flow velocities, and particle acceleration are suppressed using zero, first, and second moment nulling, respectively. To capture the vector wave displacement, these motion-sensitizing gradients are placed in the phase, readout, and slice selection encoding directions. Accurate determination of phase variations within the complex MRI signal requires multiple acquisitions, each sampling the wave with a different phase shift. In the same context, synchronization between MEGs and vibration hardware is required to ensure that the wave is sampled at specific points of the oscillation cycle [42].

During the acquisition process, various interferences to the intended shear waveform may arise. These include the generation of a mix of shear waves and compression waves by the vibration actuators, alongside the liver pulsations induced by the

dynamic perfusion of the heart. As shear deformations provide the most accurate representation of biomechanical tissue properties, compression waves and noise should be suppressed in subsequent image post-processing steps. Firstly, the complex MR signal undergoes smoothing followed by the extraction of its real-valued phase. The detected soft tissue displacement, modulated by the applied vibration frequency, fluctuates in the range of tens of microns. When the displacement amplitude exceeds a certain threshold, the encoded phase is wrapped back inside the interval $(-\pi, \pi]$. To recover accurate phase values, a 2-dimensional (2D) in-plane unwrapping algorithm is applied across all three encoding directions. Subsequently, the temporal Fourier transform (FT) is performed on the unwrapped phase to extract the harmonics corresponding to the driving frequency, which is stored in the first bin of the Fourier spectrum. This transformation results in a complex wave field where the motion is encoded for each frequency and each MEG direction [1, 42, 51]. Following the temporal FT, spatial high-pass filtering is applied to the 2D k-space to suppress low-frequency compression waves. The k-MDEV algorithm [52] introduces a novel method to determining the complex wave vector k_j for each of the wave field components u_j , assuming isotropy and local homogeneity. The complex wave vector is denoted as $k_j^* = k_j' + i k_j''$ where k_j' and k_j'' being its real and the imaginary parts. To decompose the wave field into plain waves with multiple propagation directions (e.g. $n = 4$), a directional radial filter can be used. SWS averaged over all field components (j) and vibration frequencies (ω_i) is then calculated as an amplitude-weighted average:

$$\text{SWS}(\mathbf{r}) = \left(\frac{\sum_{i,j,n} \frac{k_j'(\mathbf{r}, \omega_i, \vartheta_n)}{\omega_i} W(\mathbf{r}, \omega_i, \vartheta_n)}{\sum_{i,j,n} W(\mathbf{r}, \omega_i, \vartheta_n)} \right)^{-1} \quad (29)$$

and PR is calculated as:

$$\text{PR}(\mathbf{r}) = \left(\frac{\sum_{i,j,n} \frac{2\pi k_j''(\mathbf{r}, \omega_i, \vartheta_n)}{\omega_i} W(\mathbf{r}, \omega_i, \vartheta_n)}{\sum_{i,j,n} W(\mathbf{r}, \omega_i, \vartheta_n)} \right)^{-1} \quad (30)$$

With \mathbf{r} the spatial coordinate vector, and $W^5(\mathbf{r}, \omega_i, \vartheta_n)$ an empirical weight function

⁵ $W_{i,j,n} = |\mu_j(\mathbf{r}, \omega_i, \vartheta_n)|^4$

[8, 42]. Figure 4 illustrates the MRE measurement methodology and the subsequent post-processing steps used for the generation of biomechanical maps via the k-MDEV algorithm.

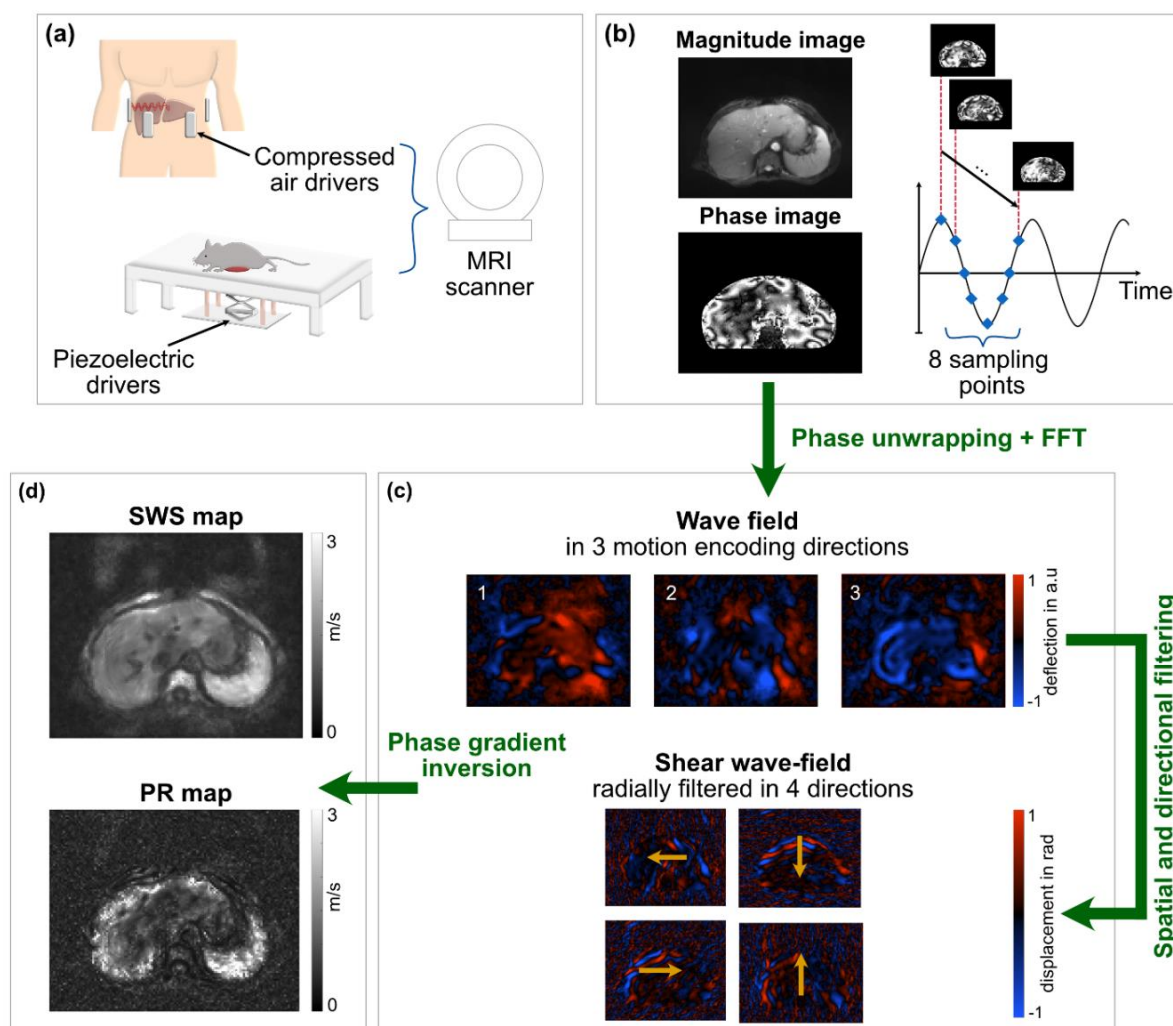


Figure 4: Stepwise process for generating biomechanical maps for human or animal liver using multifrequency magnetic resonance elastography (MRE). (a) Several compressed air drivers (four in this example) are strategically positioned on the abdomen to target the liver. Alternatively, in preclinical settings such as rodent studies, piezoelectric drivers are employed. Vibration is applied during the multifrequency MRE measurement. (b) Vibration induced motion is encoded in three directions: in-plane (longitudinal and transversal) and through-plane (slice direction). The data acquired includes magnitude and multiple phase images captured at eight different phase shifts. (c) Wave field reconstruction is accomplished through phase unwrapping and fast Fourier transform (FFT). A wave field is collected in the three encoded motion directions. Further steps involve radial directional filtering in four (or more) directions and subsequent spatial high-pass filtering to recover a shear wave field. (d) Resultant maps of shear wave speed (SWS) and penetration rate (PR), presented in meters per second (m/s), illustrate the biomechanical properties of a healthy human liver, respectively its stiffness and viscosity (Figure inspired from Sack *et al.* [41] (2023)).

2.6 Diffusion-weighted imaging

Diffusion-weighted imaging encodes incoherent motion of water molecules, also known as Brownian motion or water diffusion. The information of water diffusivity in soft tissues offers valuable insights into the integrity of cellular structures and the exchange of fluids between intracellular and extracellular environments processes that also influence the tissue biomechanical properties [53].

To detect diffusion, DWI employs a bipolar diffusion sensitizing gradient with two short, high-gradient lobes separated by a time interval (Δ) and a zeroth moment nulling [53, 54]. The first gradient dephases the magnetization of isochromats, causing spins in each voxel to accrue varying phase offsets. During the time interval between the two bipolar gradient lobes, these spins travel along a variety of random trajectories [53, 54]. As the particles move farther away from their initial position, they accumulate to a higher phase. The second lobe of the bipolar gradient with opposite polarity is intended to partially cancel out the spin's magnetization vector. However, it cannot fully reverse the effect of the first gradient, resulting in imperfect refocusing and signal attenuation quantified by the Stejskal-Tanner equation [53, 54]:

$$\frac{S}{S_0} = e^{-bD} \quad (31)$$

Here, S and S_0 represent the signal intensity with and without diffusion weighting, respectively. D is the diffusion coefficient (mm^2/s), also designated as apparent diffusion coefficient (ADC). The parameter b denotes the b-value, indicating the strength and length of the diffusion weighting gradient (in mm^2/s). For each voxel in the image, a diffusion tensor D of 3×3 elements can be determined. Local ADC is then calculated by averaging the eigenvalues of D such as $(\lambda_{11} + \lambda_{22} + \lambda_{33})/3$. An ADC map is subsequently generated, illustrating the signal attenuation due to molecular diffusion. For instance, the hypercellular nature of a tumor restricts the movement of water molecules, leading to increased signal intensity in the diffusion-weighted image, manifested by low ADC values [53, 54].

3 Methods

3.1 Animal experiments

This section describes the animal experimentation conducted in our studies. We used rabbits, rats, and zebrafish as animal models. Each model required specific sedation, imaging protocols, and post-mortem organ analyses designed to meet the specific objectives of the study.

All experiments were conducted in accordance with European, national and institutional regulations on the welfare, husbandry and accommodation of animals used for scientific purposes. Experimental protocols followed the 3Rs principle of replacement, reduction and refinement. Approval for these experiments was obtained from the local animal ethics committee. All animals were housed under standard conditions and given food and water ad libitum. Their health was monitored routinely. The experiments were conducted at a room temperature of 23 ± 1 °C [55-57].

3.1.1. Study 1: Ex vivo liver phantom and fluid inflow preparation

Liver phantom design

This section describes the methodology presented in [55] for creating four distinct liver phantoms, each mimicking a different hepatic pathology. Each phantom study involved unique protocols for liver preparation, embedding, and the use of inflow solutions with varying viscosities. Five livers were utilized for each study, and a total of twenty livers were used throughout the experiment.

- The first phantom group consisted of native livers embedded in a soft matrix, with a low viscosity fluid used as the inflow solution. This group is referred to as the 'unconfined' scenario.
- The second phantom group comprised native livers embedded in a stiff matrix and infused with a low viscosity fluid, referred to as the 'confined' scenario.
- For the third phantom group, in-situ formaldehyde-fixed livers were embedded in a stiff matrix, and a low viscosity fluid was utilized as inflow solution. This group was termed 'confined-fixed'.
- Lastly, the fourth phantom group consisted of fresh livers embedded in a stiff matrix and infused with a high viscosity fluid, termed as the 'confined viscous' scenario [55].

Liver preparation

In study 1, organ harvesting was approved by the local authorities, the Berlin State Office for Health and Social Affairs, under registration no: T-CH 0030/21.

Twenty young healthy adult male Wistar rats were procured from by the Forschungseinrichtungen für Experimentelle Medizin, FEM, Berlin, Germany (Janvier Labs, Le Genest-Saint-Isle, France). The rats used in study 1 were 13.6 ± 1.6 weeks old and had an average weight of 440 ± 58 g at the time of the experiment. Anesthesia was induced by administering an overdose of isoflurane vapor. Following a U-shaped abdominal incision, the animals were exsanguinated via the IVC. The cannulation of the portal vein (PV) was conducted using a 4G \times 19 mm BD Neoflon cannula (Eysins, Switzerland). Subsequently, the livers underwent an in-situ perfusion with a 10 mL solution of 1X phosphate buffer saline (PBS) (life technologies, Carlsbad, California, USA) heparinized at 2500 U/L (Heparin-Natruim-250000 ratiopharm GmbH, Ulm, Germany). An additional 150 mL of PBS was pumped in-situ through the portal vein to ensure complete blood clearance and prevent clotting. Out of all the harvested livers, five were selected for an additional in situ perfusion with a 4% formaldehyde solution (Carl Roth, Karlsruhe, Germany). All in situ perfusions were administered at a flowrate of 1ml/min/g. Once the liver appeared to be cleared from blood, HA, bile duct (BD), IVC and suprahepatic vena cava (SHBC) were sutured to close the circulatory system within the organ. The prepared livers were then stored under static cold storage conditions for approximately two hours [55].

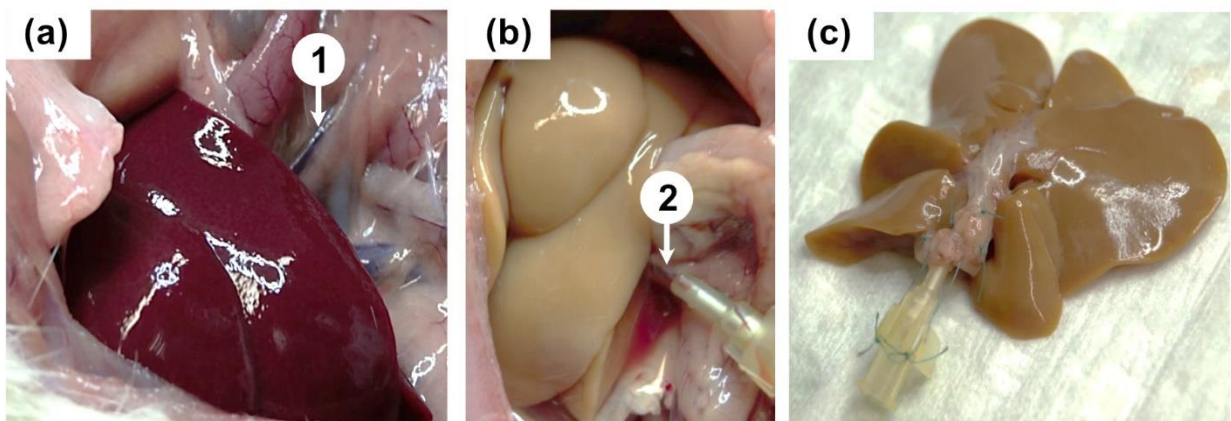


Figure 5: Decolagulation process of the rat liver. (a) Image depicting a bloody liver. (b) Subsequent flushing of blood with a heparinized phosphate buffer saline (PBS) solution results in a clean liver appearance. (c) The final image shows the explanted liver with closed vessels except for the cannulated portal vein (PV). Annotations: (1) PV located in the rat abdomen, (2) Cannulated PV.

Embedding matrix and inflow fluid characteristics

Table 2 below summarizes the different experimental conditions set for each scenario, as illustrated in figure 6.a.

Table 2: All scenarios with liver states, embedding gel consistencies, box dimensions (length (L) x width (W) x height (H)), and inflow solutions utilized for each scenario. Wt% stands for percentage by weight.

Scenarios	Liver	Embedding gel	Box dimensions (cm)	Inflow solution
Unconfined	Native	0.5 wt% agar-agar	5 L x 8.5 W x 3.0 H	PBS
Confined	Native	1:1 WiroGel /water	9.5 L x 9.5 W x 7.0 H	PBS
Confined-fixed	Crosslinked	1:1 WiroGel /water	9.5 L x 9.5 W x 7.0 H	PBS
Confined-viscous	Native	1:1 WiroGel /water	9.5 L x 9.5 W x 7.0 H	20% Arabic gum in PBS

The inflow solution was consistently prepared with addition of 0.05 percentage by weight (wt%) of alanine blue, a tissue stain serving as a visual indicator of the extent to which perfusion flow penetrated either the vascular tree or the liver tissue [55].

The kinematic viscosity (ν) for all fluid solutions was acquired at room temperature (23°C). PBS solutions were measured using an Ubbelohde viscometer while the Arabic gum solution was measured with Cannon-Fenske viscometer. The choice of different viscometers allowed accommodation of a wide range of viscosities. Subsequently, the dynamic viscosity of all inflow solution was calculated by multiplying the kinematic viscosity (ν), by the density measured using a floating hydrometer, following the formula [55]:

$$\eta = \nu \times \rho \quad (32)$$

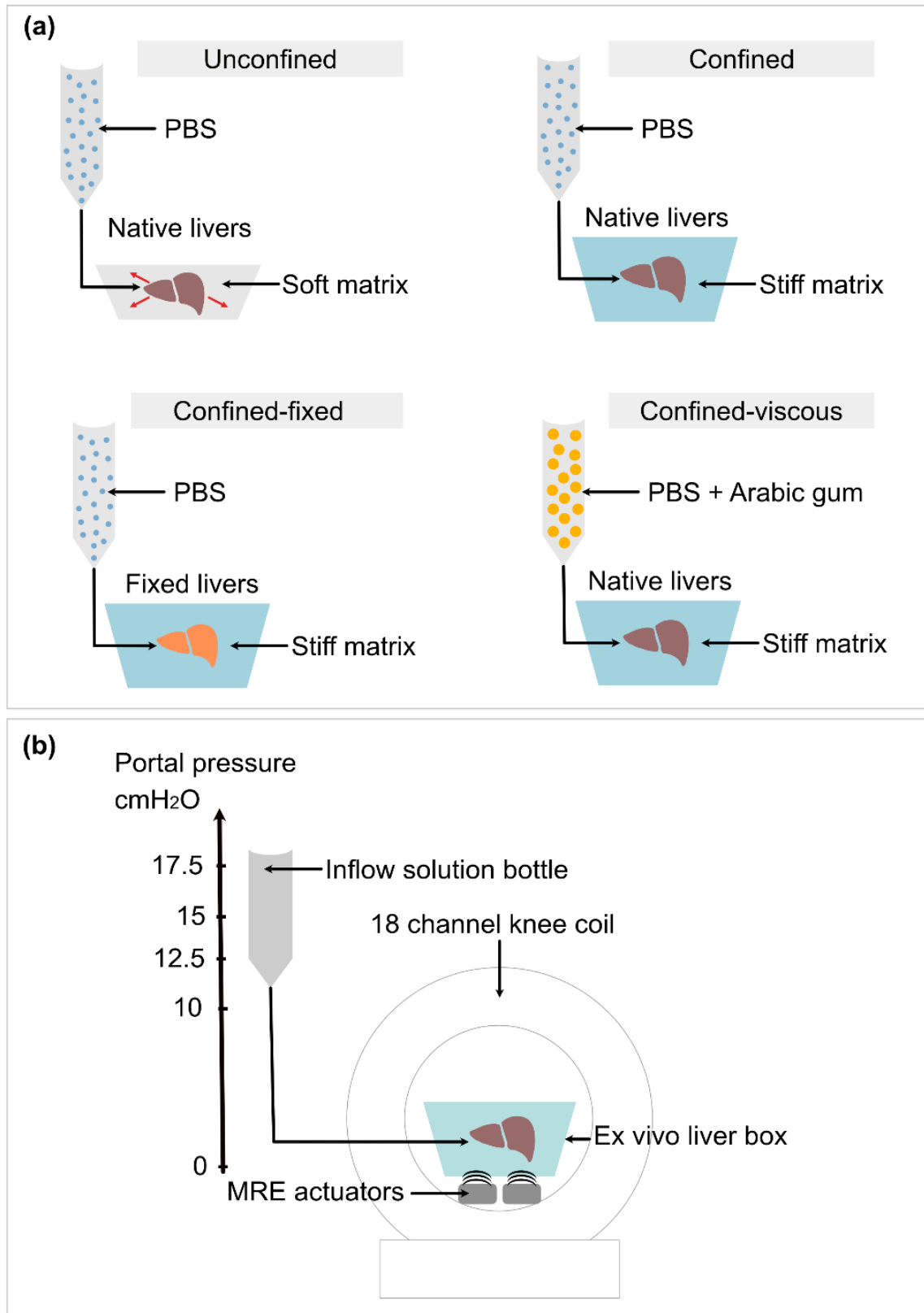


Figure 6: Schematic representation of all experimental scenarios: unconfined, confined, confined- fixed and confined-viscous. The illustrations depict differences in inflow solutions, embedding gels and liver states. (b) Technical setup for imaging, conducted on a 3 Tesla (T) scanner at room temperature [55] (Figure from Safrauo *et al* (2023)).

3.1.2. Study 2: Rabbit preparation for imaging protocol implementation

In vivo experiments in study 2 were approved by the local authorities under the registration number T-0178/17. This study involved 19 young adult female New Zealand rabbits (Charles River Laboratories in Sulzfeld, Germany) aged 11 to 15 weeks and weighing 3.2 ± 2.7 kg. Blood glucose levels were measured in the rabbits after a two-hour fasting period before the MRI scanning. To facilitate the MRI measurement, the animals were sedated with a subcutaneous injection of medetomidine hydrochloride (Cepetor KH 1mg/ml, CP-Pharma, Burgdorf, Germany) at a dose of 200 mg/kg of body weight and ketamine (Anesketin 100 mg/mL, Eurovet Animal Health B.V., Netherlands) at 300 mg/kg of body weight. Rabbits were euthanized by intravenous injection of pentobarbital sodium at 300 mg/kg of body weight (Narcofen®, Boehringer Ingelheim Vetmedica GmbH, Ingelheim am Rhein, Germany) at the end of the measurements [56].

3.1.3. Study 3: Zebrafish preparation for imaging protocol implementation

Zebrafish experiments in study 3 were approved by local authorities under two registration numbers: ZH76 and G0325/19. A total of fifteen wild-type zebrafish, aged 2 to 24 (mean age = 14 months), and eleven transgenic neuroblastoma zebrafish (MYCN), aged 6 to 25 months (mean age = 14 months) were examined. Euthanasia was carried out prior to the MRI/MRE measurement by hypothermic shock, achieved by placing the tube containing the floating fish on ice for approximately 10 minutes. The sacrificed fish were placed firmly against the wall of a 4 mm inner diameter glass tube. To minimize susceptibility artefacts caused by air to tissue interfaces, the glass tubes were filled by ultrasound (US) gel (Gello GmbH Geltechnik, Germany) [57].

3.2 Multiparametric MRI and PET measurements

3.2.1 Study 1: T2-weighted and diffusion-weighted imaging

Inducing static portal pressure in ex vivo livers

The embedded livers were connected to a water reservoir via the PV cannula. The reservoir was elevated to attain hydrostatic pressures of 0 (baseline), 10, 12.5, 15, and 17.5 cmH₂O (equivalent to 0, 7.4, 9.2, 11.0, and 12.9 mmHg, respectively). Portal perfusion continued for three minutes at each pressure level before imaging. Subsequently, the flow was stopped to maintain static pressure during the measurement. Figure 6.b illustrates the technical setup dedicated for imaging [55].

T2-weighted imaging

All images in study 1 were acquired using a 3-Tesla (3T) scanner (Magnetom Lumina, Siemens, Erlangen, Germany) with an 18-channel knee coil in coronal orientation. To provide anatomical reference, 25 to 41 contiguous coronal slices of T2-weighted (T2w) images were acquired to fully cover the liver volume and capture any potential variations in liver positioning during the embedding operation. The in-plane resolution was $0.5 \times 0.5 \text{ mm}^2$. The field of view (FoV) was set to $120 \times 108 \text{ mm}^2$, and the echo time (TE) to 64 ms. As for the repetition time (TR), it varied from 2760 ms for 25 slices to 4450 ms for 41 slices [55].

Diffusion-weighted imaging

Twenty-seven isotropic DWI slices (voxel size = $1.5 \times 1.5 \times 1.5 \text{ mm}^3$) with no slice gap were acquired at three b-values (50, 400 and 800 s/mm²) using as acquisition parameters, TE = 81 ms, TR = 1500 ms and FoV = $120 \times 90 \text{ mm}^2$. The scanner workstation automatically computed the ADC maps (in $\mu\text{m}^2/\text{s}$) using all b-values [55, 58].

3.2.2. Study 2: T1-weighted imaging and PET measurements

T1-weighted imaging

All liver measurements in study 2 were performed using a 3T hybrid PET/MR scanner (Magnetom Biograph mMR, Siemens Healthineers, Erlangen, Germany) combined with a 20-channel head coil. The animals were fixed in a prone position, and images were

acquired in the transverse orientation to ensure complete coverage of the liver. A fat-saturated Dixon sequence acquired T1-weighted (T1w) images with the following parameters: TE = 1.49 ms, TR = 4.76 ms, with an in-plane resolution of $0.5 \times 0.5 \text{ mm}^2$ and a slice thickness of 2.0 mm. The FoV was $512 \times 512 \text{ mm}^2$ [56]. The experimental setup is depicted in figure 7.

PET measurement

In a subset of 10 rabbits, PET measurements were performed following intravenous injection of ^{18}F -FDG radiotracer (average $75.88 \pm 14.35 \text{ MBq}$). The PET scan covered the entire thorax and abdomen. Reconstruction of PET images utilized the ordered-subset expectation maximization (OSEM) algorithm with parameters set to 3 iterations and 21 subsets. The image matrix was $512 \times 512 \times 127$, with a voxel size of $1.0 \times 1.0 \times 2.0 \text{ mm}^3$. Attenuation and scatter correction (AC) were carried out using an ultrashort echo-time sequence (UTE) implemented by the vendor [56].

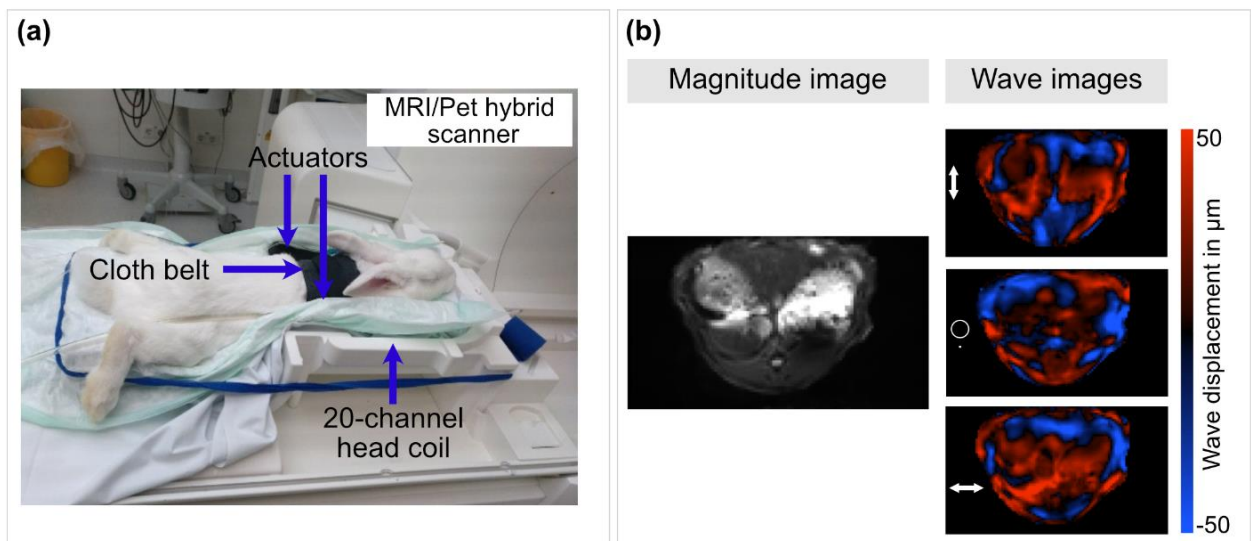


Figure 7: (a) Experimental setup for healthy liver investigation in female rabbit using 3T PET/MRI. (b) Representative MRE magnitude image and wave fields shown at 50 Hz for the three-motion encoding components, head-feet, ventral-dorsal and left-right, represented by the symbols \updownarrow , \odot , \leftrightarrow respectively. PET stands for positron emission tomography while MRI stands for magnetic resonance imaging [56] (Figure from Shahryari *et al.* (2023)).

3.2.3. Study 3: T2-weighted measurements

All images in study 3 were acquired at the 7T Bruker, Biospec scanner (Bruker Corporation, Billerica, MA, USA) with 5 mm-bore, transverse electromagnetic, quadrature volume resonator coil in coronal orientation. High-resolution T2w images were acquired using a rapid acquisition with relaxation enhancement (RARE) fast spin-echo (SE) sequence. Imaging parameters were: FoV = $68 \times 68 \times 1.0 \text{ mm}^2$; TE = 17.91 ms and TR = 3000 ms. The in-plane resolution was $0.06 \times 0.06 \text{ mm}^2$, and the slice thickness was 0.6 mm [57]. T2w images in study 3 were solely utilized for anatomical orientation and will thus not be presented in the framework of this manuscript. The technical setup designed to conduct T2w and MRE measurements is shown in figure 8 below [57].

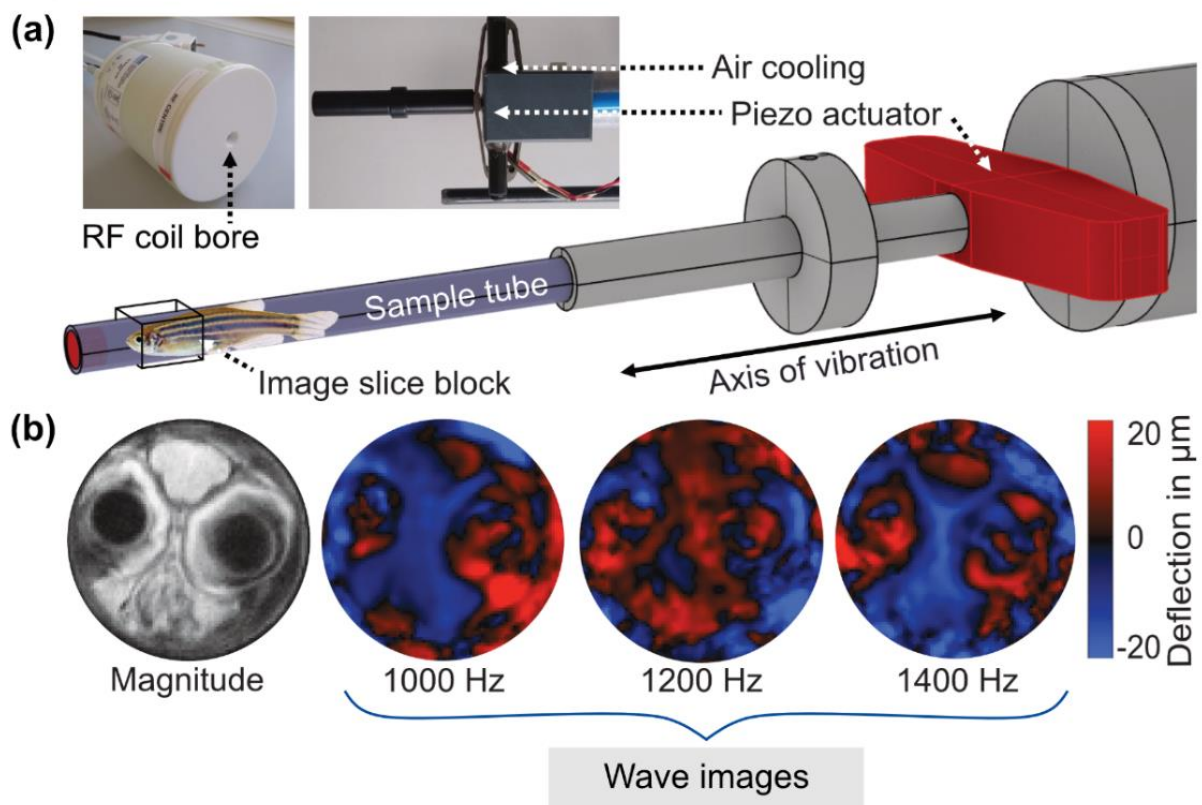


Figure 8: (a) Setup for zebrafish MRE in a 7T preclinical MRI scanner [57]. A piezoelectric actuation unit, depicted in red, generates harmonic oscillations synchronized with the MRE sequence. The primary direction of vibration is aligned with the cylinder axis, resulting in predominantly cylindrical waves. The area covered by the imaging slab is outlined by the box, next to the custom volume resonator coil. (b) The MRE magnitude image is shown in grey scale, while the wave images at 1000, 1200 and 1400 Hz are shown in color, demonstrating the through-plane wave component encoded by the sequence [57]. (Figure adapted from Jordan *et al.* (2021)).

3.3 Multifrequency MRE measurements

MRE hardware and image measurement parameters for all three studies are summarized in table 3 below [55-57].

Table 3: MRE hardware and measurement parameters for all studies. SE-EPI: spin echo-echo planar

MRE parameters	Study 1	Study 2	Study 3
Vibration actuators	Two compressed air drivers	Two compressed air drivers	One piezo actuator (ATA 200, Cedrat Technologies, France)
Sequence	Single shot SE-EPI	Single shot SE-EPI	SE, motion sensitized
Position of vibration actuator	Beneath the container	Upper abdomen region	Parallel to the cylinder axis
Vibration frequencies (Hz)	130, 140, 150, 160	40, 50, 60, 70, 80	1000, 1200, 1400
Timepoints	8	8	4
TE (ms)	44	40	38
TR (ms)	2070	1000	3000
MEG			
Encoded directions	3	3	1, slice select only
Amplitude in mT/m	34	42	392
In-plane resolution (mm²)			
Thickness (mm)	1.5	5.0	0.6
Slice			
number	20	6	8
orientation	Coronal	Transversal	Coronal
FoV (mm²)	120 × 90	104 × 60	4 × 4
Measurement time (min)	10:30	8:00	16:00

3.4 Image post-processing

This section describes post-processing methods utilized for segmentation, quantification of imaging parameters, and reconstruction of maps for biomechanical parameters across all studies.

3.4.1 Study 1

Vessel and tissue volume segmentation based on T2 weighted images

Vessel and total liver segmentation were conducted for each pressure step and in every liver. Total liver volume was segmented manually on T2w images using ITK SNAP (3.0.8). In contrast, vascular segmentation was performed automatically using an unsharp masking-based segmentation algorithm. This algorithm primarily relied on two key segmentation parameters: the image contrast threshold and the size of the median smoothing kernel. Initially, median-smoothed versions of the T2-weighted (T2w) image were created using smoothing kernels ranging from size 3 to 30. Subsequently, each original T2w image was subtracted from its respective smoothed version, resulting in sharper edges and enhanced contrast. A total of 10^4 incremental contrast thresholds, spanning from the lowest to the highest contrast value within the image, were then iteratively applied to the sharpened T2w version. Consequently, a vessel mask was generated for each combination of smoothing kernel size and contrast threshold in [55]. The F1 similarity score was computed to determine the optimal combination of segmentation parameters as described in [55]. In order to improve the accuracy of the vessel detection algorithm, ten vessel masks were manually drawn, then the F1 score was calculated based on the similarity between the automatically generated mask and the corresponding manually drawn one. The improved algorithm was thereafter utilized so that a final 3D vessel mask was selected for each liver at each pressure level, based on the highest F1 similarity score. The selected vessel mask was subsequently used for further volumetric analysis. Now, the vessel tissue volume fraction (VTVF) was calculated as the ratio of the vessel volume to the tissue volume, with the tissue volume being the vessel volume subtracted from the total liver volume [55]:

$$\text{VTVF} = \frac{\text{vessel volume}}{\text{total volume} - \text{vessel volume}} = \frac{\text{vessel volume}}{\text{tissue volume}} \quad (33)$$

Vascular segmentation and VTVF calculation were performed on MATLAB 2022b [55].

Biomechanical parameter reconstruction

MRE parameters were computed using the wavenumber-based inversion method k-MDEV executed on MATLAB 2022b (MathWorks, Natick, MA) [59]. An empirical Gaussian low-pass filter with a sigma equal to 2.75×10^{-3} was utilized to smooth the complex MR signal and suppress the noise before phase unwrapping. A high-pass, Gaussian directional radial filter was subsequently applied to extract the single-plane wave data information in eight different directions and suppress low-frequency compressional waves. Frequency-compound SWS maps in m/s were obtained the entire liver and surrogated liver stiffness [52, 55] .

Image registration

Magnitude, SWS and ADC maps were registered to the T2w images using a sequence of rigid, B-spline, and affine registration [55]. To avoid edge artefacts resulting from registration, liver masks were applied to SWS and ADC maps with a 2 mm erosion, allowing accurate calculations [55]. Mean values of SWS in m/s and ADC in $\mu\text{m}^2/\text{s}$ were calculated based on the manually drawn and eroded liver masks.

3.4.2 Study 2

Biomechanical parameter reconstruction

A low-pass Butterworth filter with an order of 3 and a threshold of 250 m^{-1} was applied on the MR complex data to suppress noise. Following image unwrapping, a Butterworth bandpass filter of the same order (thresholds: 15 m^{-1} , 300 m^{-1}) was utilized as a directional filter. Frequency-compound SWS and PR maps (both in m/s) were computed using the k-MDEV algorithm [56]. PR maps surrogated hepatic inverse viscosity.

Standardized uptake values calculations

To visualize in vivo glucose metabolism indicated by the ^{18}F -FDG-based PET measurement, maps of the standardized uptake value (SUV) were generated for the corresponding subset of rabbits using:

$$SUV = \frac{A(t) \cdot W}{ID \cdot d} \quad (34)$$

With $A(t)$ represents the activity concentration (in kBq/mL), W denotes the body weight (in kg), ID is the injected ^{18}F -FDG dose (in MBq), and d is the dose and decay correction factor derived from the half-life of the radiotracer and the time delay between injection and the start of the measurement [56].

The liver was delineated on all MRE magnitude images; and the resulting regions of interest (ROIs) were employed to calculate the mean values of SWS (m/s) and PR (m/s) on the corresponding maps [56]. In contrast, mean SUVs were derived from manually delineated masks on the AC PET images outlining the liver. The manual mask drawing process was performed using ITK SNAP (3.0.8).

3.4.3 Study 3

To optimize the MRE image quality for study 3, an initial assessment was conducted using the tabletop MRI with various resolutions ($40 \times 40 \mu\text{m}^2$, $60 \times 60 \mu\text{m}^2$, $80 \times 80 \mu\text{m}^2$, and $100 \times 100 \mu\text{m}^2$) within a $4 \times 4 \text{mm}^2$ FoV. The setup, similar to that used for zebrafish measurements, utilized ultrasound gel to produce wave images. These images guided the adjustment of filtering parameters, described in the following section, ensuring accurate biomechanical reconstructions.[57].

Biomechanical parameter reconstruction

A spatial Butterworth bandpass filter of seventh order and a higher threshold of 250m^{-1} was applied to filter out any minor impact of compression waves from the resulting complex-valued wave images. SWS maps were reconstructed based on the k-MDEV algorithm [59] whereas fluidity (φ) maps were reconstructed based on the MDEV algorithm [57, 60]. ROIs covering the entire brain volume (B), cerebellum (CB), midbrain (MB), optic tectum (OT), skeletal muscle (SM), and telencephalon (TC) were manually delineated on the corresponding MRE magnitude images using MATLAB 2022b. Similarly, ROIs were created for neuroblastoma (T) which was identified in transgenic fish [57]. Mean values of SWS (m/s) and φ (rad) were calculated for all the aforementioned ROIs in the zebrafish brain. φ maps surrogated tissue fluidity.

3.5 Post-mortem tissue characterization

In this context, post-mortem tissue analyses were conducted to comprehensively characterize the tissue microstructure and metabolic profile, particularly in relation to imaging and biomechanical parameters [55-57].

3.5.1 Study 1: Preparations for macro and microscopic observations

Following imaging, the perfused livers were separated from the embedding gel. Thin slices, less than 1.0 mm thick, were prepared for direct observation under a light microscope. The remaining liver was stored in formaldehyde overnight then histologically processed to obtain 5 μm -thick liver sections stained with hematoxylin and eosin (H&E) [55].

3.5.2 Study 2: Metabolic characterization of healthy liver samples

Following sacrificing the rabbit, the liver was immediately explanted, and a small tissue section per liver (100 g maximum) was rapidly sampled and snap-frozen in liquid nitrogen at -80°C for proteomics analysis. Lysates were then prepared from the samples allowing for protein extraction and purification as described in [56]. The supernatant of the digested solution was subjected to nano-flow reverse liquid chromatography (LC), allowing for gradual elution and high-resolution separation of peptides. Subsequently, as the separated peptides eluted in nanoliter flow from the separation column, they were directed through the mass spectrometer (MS). Here, the mass spectrometer measured the mass-to-charge ratios (m/z) of the eluted peptides, thereby enabling their identification and quantification.

Following the acquisition of quantitative LC-MS results, metabolic capacity was investigated by applying the HEPATOKIN1 biochemistry-based model of liver metabolism [24]. Based on the 6000 proteins identified and quantified within the samples, individualized kinetic models were employed to depict metabolic maximal capacities, while maintaining plasma nutrient levels at diurnal averages. Two physiological states were used to describe metabolism in healthy rabbits: The fasted state, characterized by low glucose and insulin levels alongside elevated fatty acid glucagon levels; and the fed state, characterized by elevated glucose and insulin levels coupled with reduced fatty acid glucagon levels [56].

3.5.3 Study 3: Tissue staining to identify brain subregions and neuroblastoma

Caudal fins of zebrafish were dissected to optimize the subsequent formaldehyde fixation process. The fish underwent initial fixation in a 4% paraformaldehyde solution, followed by a second fixation with a decalcification buffer (0.5 M EDTA, pH: 7.2). Histological processing was carried out to prepare paraffin sections for staining. Two staining methods were used to differentiate brain structures from the tumor: sections were stained with H&E or with tyrosine hydroxylase (TH) fluorescence staining, an adrenergic tissue marker, which required additional tissue processing as described in [57].

3.6 Statistical analyses

Statistical significance was defined as $p < 0.05$ in all studies. Standard deviation was used for error estimation. Statistical analyses were performed using either R Studio (RStudio, PBC, Boston, MA) or MATLAB 2022b [21-23], depending on the specific analysis requirements.

3.6.1 Study 1

Considering the limited sample number in each group ($n = 5$) normality could not be assumed [55]. Effect sizes were determined using Kendall's coefficient of concordance (τ). The Friedman test was used to evaluate differences between various imaging parameters across all portal pressures. Subsequently, comparisons among all scenarios were conducted using the Kruskal-Wallis test, followed by the Dunn-Sidak test for post-hoc analysis. Post-hoc pairwise comparisons of baseline liver phantom imaging parameters were performed using the Nemenyi test. A linear mixed model accounting for both, random and fixed effects within the data set was used to analyze the correlations between static portal pressure and imaging parameters [55].

3.6.2 Study 2

Normality within the analyzed groups was assessed using a 95% confidence interval. Group differences for normally distributed data were determined using unpaired two-sided Student's *t*-tests, while the Wilcoxon signed-ranked test was used for non-normally distributed data. The cluster analysis was performed using the clustergram function on MATLAB's 2022b Bioinformatics toolbox. Additionally, a linear regression

model was used to analyze the correlation between metabolic and MRE parameters [22].

3.6.3 Study 3

Group differences were assessed using the Wilcoxon rank sum test, while multiple comparisons were conducted using a one-way analysis of variance along with the Bonferroni correction. Initially, the fish were categorized into three groups: wild type (group 1), tumor-bearing (group 2), and a pooled group, consisting of group 1 and group 2. As no significant differences between all brain region values in group 1 and 2 were found, comparisons between the different brain regions were analyzed in the pooled group. Within the tumor group, differences among muscle tissue, tumor tissue, and brain tissue were analyzed. Pearson correlation analysis was used to assess relationship between SWS or φ values with age and tumor sizes. However, effects of sex on MRE parameters were not investigated [57].

4 Results

4.1 mpMRI and multifrequency MRE

4.1.1 Study 1

Liver properties comparison at baseline pressure

As previously stated, we assessed the stiffness of embedded livers and embedding gels, as well as the viscosities of inflow fluids at baseline pressure (0 cmH₂O). This evaluation was conducted to detect any relevant biophysical disparities or potential interferences with the mechanical effect of the static portal pressure. Initially, significant differences among all imaging parameters were identified, as detailed in Table 4 below [55].

Table 4: Summary of all baseline values, including group means, standard deviations, and pairwise comparison results for vessel volume, tissue volume, vessel tissue volume fraction (VTVF), apparent diffusion coefficient (ADC) and shear wave speed (SWS) [55] (Table from Safraou et al. (2023)).

	Vessel volume (cm ³)	Tissue volume (cm ³)	VTVF	ADC (μm ² /s)	SWS (m/s)
Unconfined	0.6 ± 0.2	16.2 ± 1.7	0.036 ± 0.014	411 ± 21	4.3 ± 0.5
Confined	0.6 ± 0.3	12. ± 1.7	0.054 ± 0.020	370 ± 90	3.2 ± 0.4
Confined-fixed	1.2 ± 0.3	18.5 ± 3.0	0.065 ± 0.017	521 ± 18	5.5 ± 0.9
Confined-viscous	0.4 ± 0.2	14.8 ± 1.6	0.023 ± 0.017	330 ± 50	3.3 ± 0.3
p	0.0085	0.0054	0.0123	0.0029	0.0014
Post-hoc comparison	Confined-fixed vs. Confined-viscous: <i>p</i> = 0.0085	Confined-fixed vs. Confined: <i>p</i> = 0.0054	No significant differences between the groups	Confined-fixed vs. Confined-viscous: <i>p</i> = 0.0028 Confined-fixed vs. Confined: <i>p</i> = 0.0321	Confined-fixed vs. Confined-viscous: <i>p</i> = 0.0096 Confined-fixed vs. Confined: <i>p</i> = 0.0055

Embedding gels and inflow fluids

Stiffness values for all embedding matrices were determined by calculating the average SWS across the matrix area identified on the MRE magnitude image. Table 5 below provides a detailed characterization of matrix stiffness, dynamic viscosity η and density ρ at baseline pressure [55].

Table 5: Values for matrix stiffness (in m/s), fluid dynamic viscosities (η in mPa.s) densities (ρ in kg/m³) as baseline pressure (0 cmH₂O) for all scenarios. The fluid inflow solution has the same viscosity and density values for the unconfined, confined and confined-fixed scenarios. However, in the confined-viscous scenario, unique density and viscosity values were measured.

	Matrix stiffness (m/s)	η (mPa.s)	ρ (kg/m³)
Unconfined	2.3 ± 0.3		
Confined	7.5 ± 0.9	0.0157 ± 0.005	1005
Confined-fixed	8.6 ± 0.2		
Confined-viscous	8.4 ± 0.4	23.72 ± 0.19	1070

The evolution of biophysical imaging parameters upon increasing pressures

In figure 9 we show the T2w images, ADC maps, shear wave images at 160 Hz and the corresponding SWS maps at baseline pressure and 17.5 cmH₂O for all four experimental scenarios: unconfined (figure 9.a), confined (figure 9.b), confined-fixed (figure 9.c) and confined-viscous (figure 9.d) [55]. Across all scenarios, an increase in signal intensity within the liver tissue (dashed blue outline) as well as vascular dilatation (red outline) was observed with elevated portal pressure. Remarkably, a consistent increase in ADC occurred, particularly in the unconfined scenario. Both the unconfined and confined-fixed scenarios showed a decrease in shear wavelength at 160 Hz, indicating a tendency towards softening as portal pressure increased. This observation was corroborated by the apparent decrease in the corresponding SWS maps. In contrast, confined-viscous livers exhibited an increase in shear wavelength at higher pressures, suggesting a stiffening tendency. The confined livers, however, did not exhibit any changes in stiffness as pressure increased [55].

Figure 10 shows the evolution of group mean values for all imaging parameters: VTVF (figure 10.a), ADC (figure 10.b), SWS (figure 10.c) with increasing static portal pressure levels across all scenarios. Notably, elevated portal pressure resulted in a significant increase in VTVF in all groups, with the most pronounced effect

observed in unconfined livers ($300 \pm 120\%$, $p < 0.05$). Confined-viscous livers exhibited the second highest increase in VTVF ($210 \pm 110\%$, $p < 0.0152$), followed by confined ($53 \pm 32\%$, $p < 0.01$) and confined-fixed ($52 \pm 20\%$, $p < 0.001$) scenarios with almost similar increases in VTVF [55].

ADC showed a significant increase at 17.5 cmH₂O compared to baseline. The effect of portal pressure on ADC was most pronounced in the unconfined livers ($88 \pm 29\%$, $p < 0.01$), with lesser effects observed in the confined ($28 \pm 19\%$, $p < 0.05$), confined-viscous ($26 \pm 9\%$, $p < 0.001$) then confined-fixed ($11 \pm 2\%$, $p < 0.01$) scenarios [55].

Under pressure elevation, SWS exhibited different tendencies across all scenarios. In unconfined livers, SWS decreased by $12 \pm 5\%$ ($p < 0.05$), while a similar decrease of $11 \pm 7\%$ was observed in the confined-fixed scenario ($p < 0.01$). Conversely, confined-viscous livers showed an opposite response to higher portal pressure, with an increase in SWS by $11 \pm 4\%$ ($p < 0.001$). SWS values remained unchanged in confined livers ($p = 0.52$) [55].

To address potential artifacts that could arise from fluid filling in vessels during portal pressure elevation, we compared mean values of imaging parameters within liver masks with and without vessels. Absolute ADC values significantly decreased in the absence of segmented vascular area ($p < 0.001$). In contrast, absolute values of SWS at all pressure levels for all scenarios remained unchanged after the vascular segmented area was removed ($p = 0.21$). Table 6 provides mean and standard deviation values of tissue volume, vascular volume, VTVF, ADC (with and without vessels) and SWS (with and without vessels) for all scenarios and pressure levels [55].

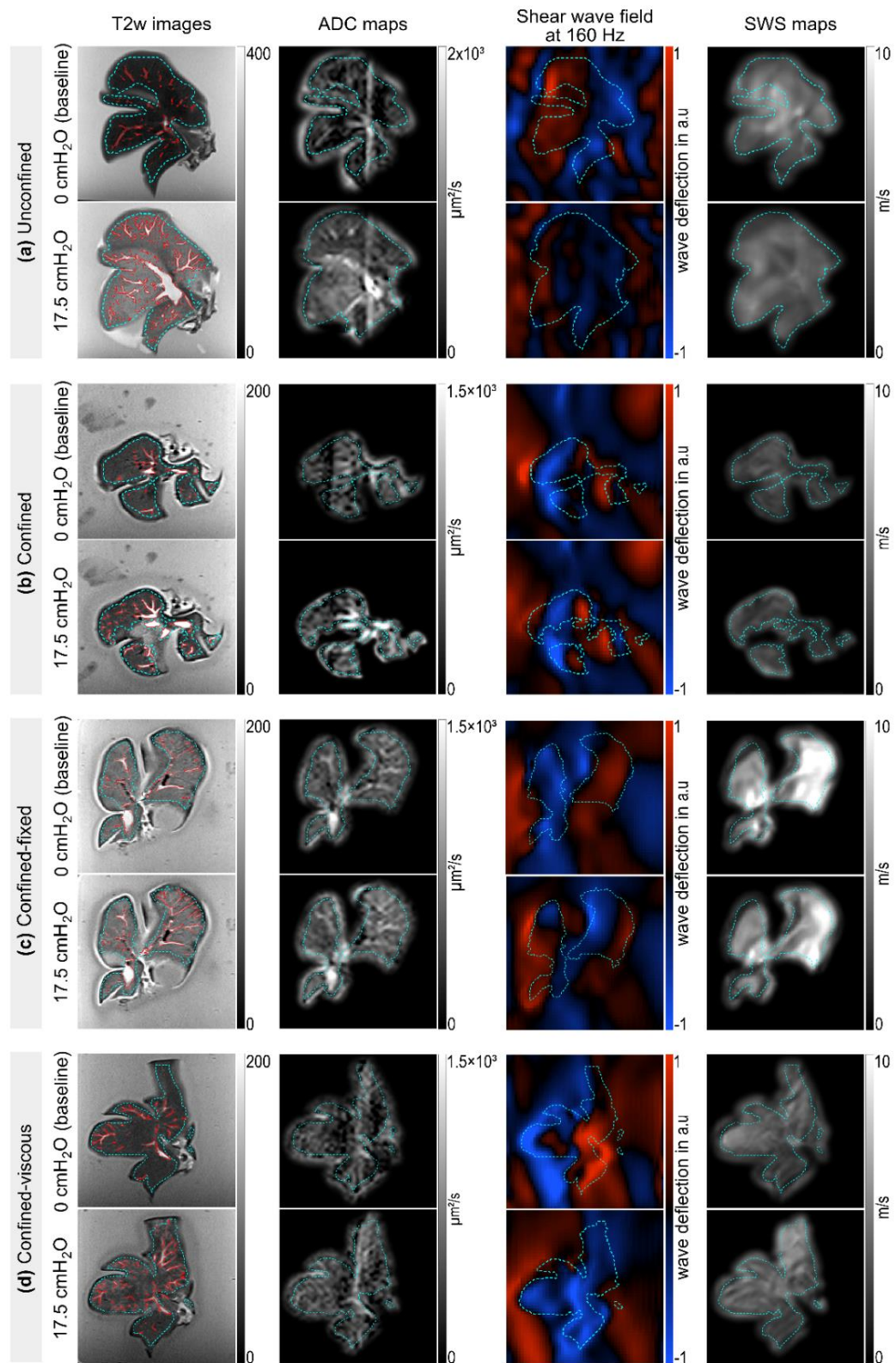


Figure 9: T2 weighted images (T2w), Apparent diffusion coefficient (ADC) maps, MRE shear wave field images at 160 Hz and SWS maps, obtained at two portal pressure levels 0 (baseline) and 17.5 cmH₂O, shown for four scenarios: unconfined (a), confined (b), confined-fixed (c), and confined-viscous (d). Masks for the entire liver and the segmented vessels are outlined with dotted cyan and solid red lines, respectively. ADC surrogates for water diffusivity, while SWS surrogates for hepatic stiffness [55] (Figure from Safraou *et al.* (2023)).

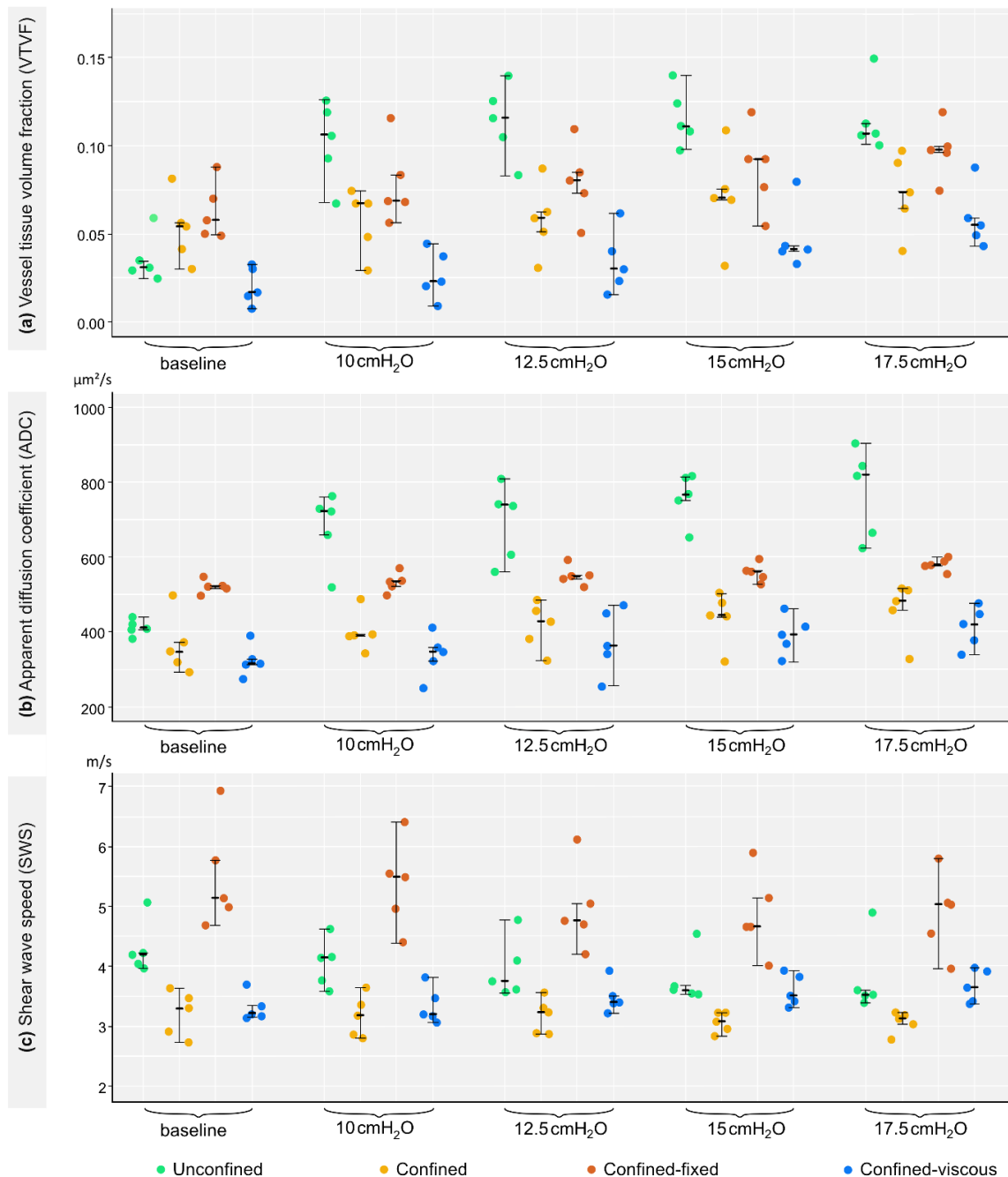


Figure 10: Swarm plots illustrating the evolution of the imaging parameters: (a) vessel tissue volume fraction (VTVF). (b) ADC and (c) SWS over increasing portal pressure (in cmH₂O) of livers in unconfined (green), confined (yellow), confined-fixed (orange), and confined-viscous (blue). The plots include the lower and upper quartiles as well as the mean values [55] (Figure from Safraou *et al.* (2023)).

Table 6: Group mean values and standard deviations of vessel volume in cm³, tissue volume in cm³, VTVF, ADC (with or without vessels) and SWS (with or without vessels) acquired at all static portal pressure levels for all scenarios. *p* values and effect sizes *τ* are provided. Changes in the imaging parameters over increased pressure were assessed. SD stands for standard deviation [55] (Table from Safraou *et al.* (2023)).

	Pressure in cmH ₂ O	Vessel volume (cm ³)	Tissue volume (cm ³)	VTVF	ADC in μm ² /s	SWS in m/s	ADC vessels excluded in μm ² /s	SWS vessels excluded in m/s	
	mean ± SD	mean ± SD	mean ± SD	mean ± SD	mean ± SD	mean ± SD	mean ± SD	mean ± SD	
Unconfined	0	0.6 ± 0.2	16.2 ± 1.7	0.036 ± 0.014	411 ± 21	4.3 ± 0.5	384 ± 11	4.3 ± 0.5	
	10	2.0 ± 0.6	18.8 ± 2.6	0.102 ± 0.024	680 ± 100	4.1 ± 0.4	613 ± 88	4.1 ± 0.4	
	12.5	2.4 ± 0.6	20.8 ± 3.6	0.114 ± 0.022	690 ± 110	4.0 ± 0.5	629 ± 100	4.0 ± 0.5	
	15	2.6 ± 0.3	22.3 ± 3.0	0.116 ± 0.017	780 ± 70	3.8 ± 0.4	715 ± 64	3.8 ± 0.5	
	17.5	2.7 ± 0.6	23.5 ± 2.1	0.115 ± 0.020	770 ± 120	3.8 ± 0.7	719 ± 122	3.8 ± 0.7	
	Post-hoc	0 vs.15 <i>p</i> = 0.0230	0 vs.15 <i>p</i> = 0.030	0 vs.17.5 <i>p</i> = 0.002	0 vs.15 <i>p</i> = 0.007	0 vs.15 <i>p</i> = 0.005	0 vs.15 <i>p</i> = 0.007	0 vs.17.5 <i>p</i> = 0.023	
		0 vs.17.5 <i>p</i> = 0.003	0 vs.17.5 <i>p</i> = 0.003		0 vs.17.5 <i>p</i> = 0.003	0 vs.17.5 <i>p</i> = 0.012	0 vs.17.5 <i>p</i> = 0.003		
	<i>p</i>	0.002	0.002	0.028	0.001	0.015	0.001	0.027	
	<i>τ</i>	0.59	0.57	0.43	0.60	-0.45	0.61	-0.41	
	Confined	0	0.7 ± 0.3	12.1 ± 1.7	0.054 ± 0.020	370 ± 90	3.2 ± 0.4	349 ± 71	3.2 ± 0.4
10		0.7 ± 0.3	12.0 ± 1.7	0.057 ± 0.019	400 ± 60	3.2 ± 0.4	381 ± 45	3.1 ± 0.3	
12.5		0.8 ± 0.3	12.6 ± 1.7	0.058 ± 0.021	410 ± 70	3.2 ± 0.3	393 ± 58	3.2 ± 0.3	
15		0.9 ± 0.4	12.4 ± 1.7	0.071 ± 0.028	440 ± 70	3.0 ± 0.2	404 ± 62	3.2 ± 0.3	
17.5		1.1 ± 0.4	12.4 ± 1.7	0.082 ± 0.027	460 ± 80	3.0 ± 0.2	421 ± 65	3.2 ± 0.3	
Post-hoc		0 vs.17.5 <i>p</i> = 0.012	-	0 vs.17.5 <i>p</i> = 0.02 10 vs. 17.5 <i>p</i> = 0.03 12.5 vs.17.5 <i>p</i> = 0.04	0 vs.17.5 <i>p</i> = 0.007	-	0 vs.17.5 <i>p</i> = 0.006	-	
<i>p</i>		0.005	0.49	0.003	0.01	0.52	0.02	0.6	
<i>τ</i>		0.32	-0.05	0.37	0.36	-0.15	-0.06	0.32	
Confined-fixed		0	1.2 ± 0.3	18.5 ± 3.0	0.065 ± 0.017	521 ± 18	5.5 ± 0.9	495 ± 15	5.6 ± 0.9
		10	1.4 ± 0.4	18.3 ± 3.1	0.075 ± 0.023	534 ± 26	5.4 ± 0.8	503 ± 22	5.4 ± 0.8
	12.5	1.5 ± 0.4	18.2 ± 3.1	0.082 ± 0.022	550 ± 27	5.0 ± 0.7	515 ± 21	5.0 ± 0.7	
	15	1.6 ± 0.4	18.1 ± 3.1	0.087 ± 0.024	557 ± 25	4.9 ± 0.7	522 ± 21	4.9 ± 0.7	
	17.5	1.7 ± 0.3	17.5 ± 3.5	0.097 ± 0.016	578 ± 18	4.9 ± 0.7	537 ± 15	4.9 ± 0.7	
	Post-hoc	0 vs.17.5 <i>p</i> = 0.012	0 vs. 17.5 <i>p</i> = 0.002	0 vs. 17.5 <i>p</i> = 0.001 0 vs. 15 <i>p</i> = 0.01 10 vs. 17.5 <i>p</i> = 0.041 10 vs. 17.5 <i>p</i> = 0.05	0 vs. 17.5 <i>p</i> = 0.014 10 vs. 17.5 <i>p</i> = 0.041	0 vs. 15 <i>p</i> = 0.041 0 vs. 17.5 <i>p</i> = 0.012	0 vs. 17.5 <i>p</i> = 0.009 10 vs. 17.5 <i>p</i> = 0.023	0 vs. 15 <i>p</i> = 0.009 0 vs. 17.5 <i>p</i> = 0.041	
	<i>p</i>	0.0006	0.002	0.0006	0.002	0.003	0.002	0.003	
	<i>τ</i>	0.43	-0.22	0.45	0.57	-0.24	0.51	-0.24	
	Confined-viscous	0	0.4 ± 0.2	14.8 ± 1.6	0.023 ± 0.011	330 ± 40	3.3 ± 0.2	316 ± 40	3.3 ± 0.3
		10	0.4 ± 0.3	14.9 ± 1.7	0.027 ± 0.015	340 ± 60	3.4 ± 0.3	324 ± 54	3.4 ± 0.3
12.5		0.5 ± 0.3	15.0 ± 1.6	0.034 ± 0.018	380 ± 90	3.5 ± 0.3	357 ± 75	3.5 ± 0.3	
15		0.7 ± 0.3	15.0 ± 1.6	0.047 ± 0.019	390 ± 60	3.6 ± 0.3	368 ± 55	3.6 ± 0.3	
17.5		0.9 ± 0.3	15.1 ± 1.8	0.059 ± 0.018	410 ± 60	3.7 ± 0.3	382 ± 56	3.7 ± 0.3	
Post-hoc		0 vs. 15 <i>p</i> = 0.04 0 vs. 17.5 <i>p</i> = 0.0014 10 vs. 17.5 <i>p</i> = 0.012	-	0 vs. 15 <i>p</i> = 0.04 0 vs. 17.5 <i>p</i> = 0.0014 10 vs. 17.5 <i>p</i> = 0.012	0 vs. 17.5 <i>p</i> = 0.0061 10 vs. 17.5 <i>p</i> = 0.023	0 vs. 17.5 <i>p</i> = 0.003 10 vs. 17.5 <i>p</i> = 0.0061	0 vs. 17.5 <i>p</i> = 0.007 10 vs. 17.5 <i>p</i> = 0.023	0 vs. 15 <i>p</i> = 0.002 10 vs. 17.5 <i>p</i> = 0.009	
<i>p</i>		0.0007	0.4	0.0007	0.003	0.0008	0.004	0.0008	
<i>τ</i>		0.51	0.084	0.56	0.40	0.43	0.35	0.43	

4.1.2. Study 2

Creating clusters based on liver stiffness

Figure 11 illustrates the MRE magnitude and PET images (Figure 11.a) alongside SWS and PR maps (figure 11.b) of the scanned rabbit liver for two distinct subgroups: stiff and soft. Livers were categorized as stiff if their SWS exceeded 1.6 m/s, while those with SWS below this threshold were considered soft, in accordance with the median SWS value observed across all rabbits. The visual inspection of the SWS maps for both subgroups supported the choice of this threshold value. Interestingly, the PR maps showed a similar trend to the SWS maps, indicating that stiffer livers tended to have higher PR values compared to softer livers. The stiff group consisted therefore of 10 rabbits with a mean stiffness of 1.66 ± 0.06 m/s and a PR of 1.06 ± 0.08 m/s, whereas the soft group consisted of 9 rabbits with a mean stiffness of 1.52 ± 0.08 m/s and a PR of 0.93 ± 0.10 m/s. No significant differences could be detected in SUV between the stiff and soft groups ($p = 0.11$). Using this stiffness-based classification, a comparative analysis of metabolic functions and non-invasive imaging markers between the two groups was performed. This was intended to investigate the potential of liver stiffness as a marker of hepatic metabolic functionality [56]. Individual SWS and PR values for each rabbit are provided in [56].

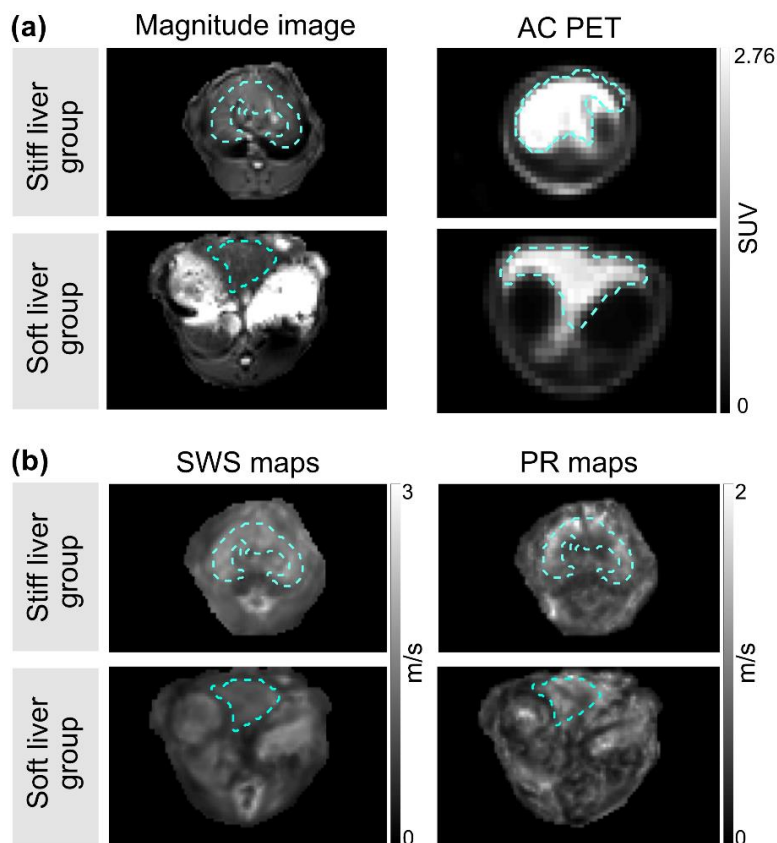


Figure 11: Comparisons between stiff and soft liver groups, with SWS > 1.6 m/s considered as stiff livers, while SWS < 1.6 m/s considered as soft livers. (a) MRE magnitude, and AC PET images of stiff and soft liver groups. (b) SWS and penetration rate (PR) maps of stiff and soft liver groups. Regions of interest within the liver are outlined with dotted cyan. All images are provided in grey scale. AC PET stands for attenuation-corrected PET [56] (Figure adapted from Shahryari *et al.* (2023)).

4.1.3. Study 3

Phantom experiment

Wave fit analysis on the unfiltered wave obtained in the gel phantom for each frequency and resolution allowed to recover ground truth reference values of $SWS = 0.77 \pm 0.09$ m/s and $\varphi = 0.30 \pm 0.08$ rad. While the phantom MRE values remained unaffected by resolution, SNR for $40 \times 40 \mu\text{m}^2$ voxels was significantly lower compared to larger voxel sizes ($p < 0.05$). Therefore, we opted for a resolution of $60 \times 60 \mu\text{m}^2$ for all animal experiments to ensure a stable SNR range unaffected by resolution [57].

Multifrequency MRE in zebrafish

Figure 12 from [57] depicts maps of magnitude, SWS and φ in coronal orientation for multiple slices of the adult zebrafish brain. Brain subregions including CB, MB, OT, SM and TC are contoured with ROIs outlined on the MRE magnitude images. Additionally, a composite microscopy image is provided to demonstrate the positioning of slices in the fish brain and highlight the tumor which is marked by green fluorescence [57].

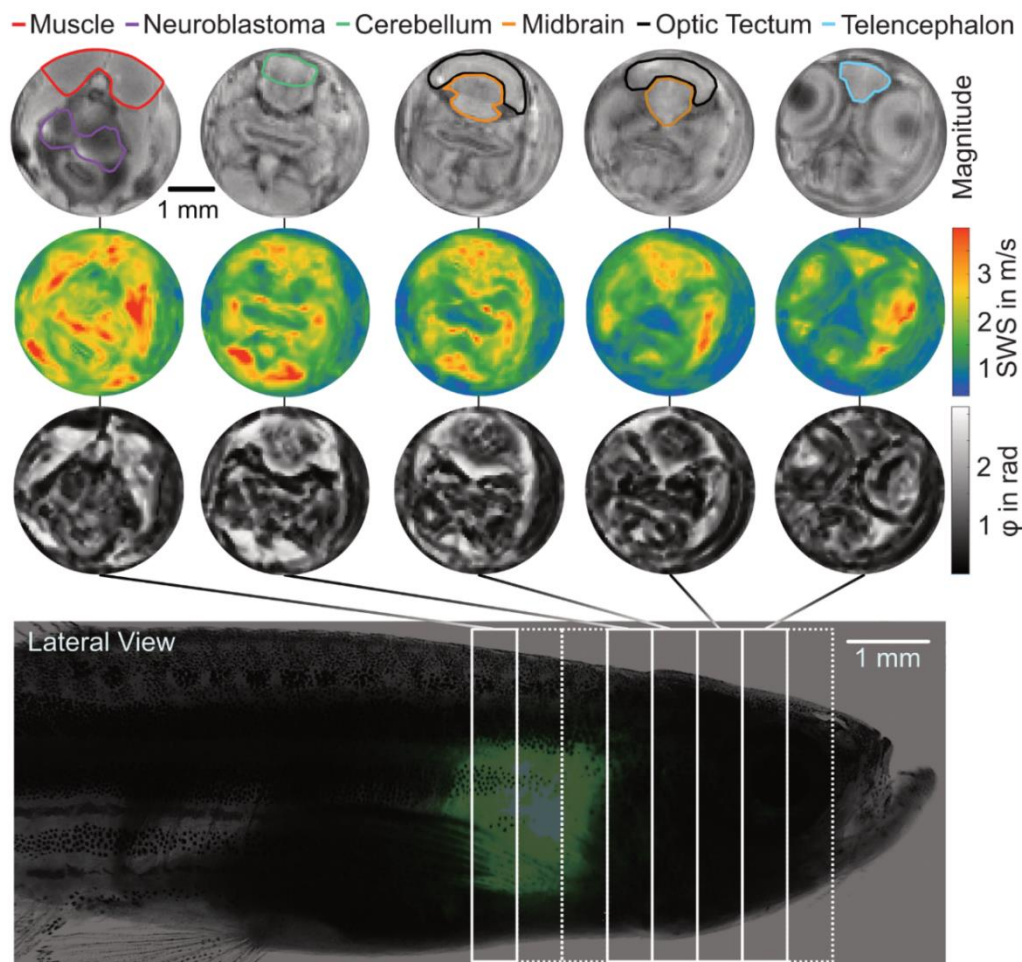


Figure 12: From top to bottom, coronal slices of MRE magnitude images, SWS, phase angle (φ) maps, and a lateral view composite microscopy image of the zebrafish. The white rectangles with continuous lines indicate approximate slice positions within the transgenic fish brain. Notably, the tumor location is highlighted by the green fluorescence, which is visible through the semi-transparent skin of the fish [57] (Figure adapted from Jordan *et al.* (2021)).

Figure 13 displays boxplots of SWS and φ for wild-type and transgenic zebrafish (pooled group) as well as transgenic fish only. The comparison included SM, T and B in figures 13.a and 13.c for transgenic fish, while pooled subregional analyses are shown in figures 13.b and 13.d.

SWS values were significantly higher in the MB region compared to the OT and TC (SWS_{MB} : 3.1 ± 0.7 m/s; SWS_{OT} : 2.6 ± 0.5 m/s; SWS_{TC} : 2.6 ± 0.5 m/s, $p < 0.05$). The CB had significantly lower φ values compared to the TC and OT (φ_{CB} = 0.9 ± 0.4 rad; φ_{TC} = 1.4 ± 0.2 rad; φ_{OT} = 1.3 ± 0.4 rad; $p < 0.05$). While comparing subregions in the pooled group, we found that values of SWS and φ in T were lower than those in SM (SWS_T = 2.4 ± 0.3 m/s, φ_T = 0.7 ± 0.1 rad; SWS_{SM} 2.9 ± 0.5 m/s, φ_{SM} = 1.4 ± 0.2 rad) [57].

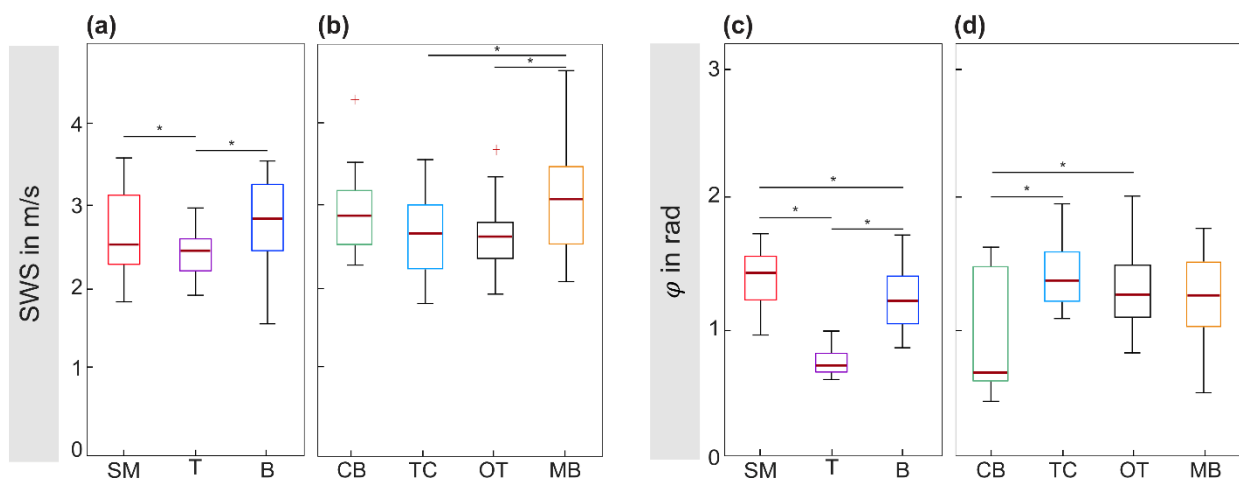


Figure 13: Boxplots of SWS and phase angle (φ) comparisons in (a) and (c), respectively, for skeletal muscle (SM), neuroblastoma (T), and whole brain (B) in transgenic zebrafish. Additionally, (b) and (d) display boxplots of SWS and φ , respectively, comparing group mean values of cerebellum (CB), midbrain (MB), optic tectum (OT), and telencephalon (TC) for the pooled group, including transgenic and wild-type zebrafish. Median values per plot are indicated in red, while boxplot whiskers are outlined in black. Statistical significance ($p < 0.05$) is denoted by asterisks [57] (Figure adapted from Jordan *et al.* (2021)).

4.2 Post-mortem tissue characteristics

4.2.1 Study 1: Changes in vascular and extracellular structures under elevated pressure

Histology findings presented in figure 14 are categorized into gross, macroscopic and microscopic observations for all scenarios. In section (a), liver photographs taken immediately after MRI imaging revealed distinct fluid distribution patterns for each scenario. Remarkably, unconfined livers exhibited a prominent blue color, indicating a widespread distribution of the inflow solution in the whole organ. In contrast, the confined liver displayed partial perfusion, with low fluid presence in the vessels as seen in the liver cross-section. The confined-fixed liver appeared to have a denser structure, with fluid distribution in both vessels and surrounding tissue, although at a lower amount compared to the unconfined liver. Lastly, the confined-viscous liver exhibited significant fluid amounts primarily within the vascular lumen [55]. Section (b) in figure 14 displays macroscopic observation of freshly sectioned liver slices of approximately 1 mm thickness, revealing visible vascular structures. In the unconfined scenario, significant amounts of fluid were observed within the vessel and surrounding tissue. Similarly, the confined-fixed liver exhibited fluid within both the vessel and the densely packed surrounding tissue, although in lower amounts. However, the confined liver revealed minimal fluid within the vessel lumen. As for the confined-viscous liver, it displayed an intense blue color within the vessel lumen but not in the surrounding tissue, suggesting a notably higher amount of fluid confined to the vascular spaces [55]. Upon examination of the H&E-stained slides shown in figure 14.c, we noted a relatively preserved trabecular arrangement within the liver lobe, with tightly packed hepatocytes in all scenarios except the unconfined one, where a sinusoidal enlargement was apparent. On closer inspection (as shown in figure 14.d, magnification x40), it became clear that in addition to structural changes, micro-vascular changes were more pronounced in the unconfined scenario, with compromised central veins observed [55].

4.2.2 Study 2: Liver stiffness as a potential marker for hepatic metabolic functions

Metabolic modelling conducted after LC-MS analysis revealed substantial differences within the healthy rabbit liver samples, delineating two distinct subgroups with significant

metabolic divergences. The first metabolic cluster comprising 10 rabbits, showed an increase in fatty acid metabolism including heightened fatty acid uptake, higher triacylglycerol (TAG) synthesis and storage, and increased ketone body synthesis. Alternatively, this subgroup displayed attenuated biosynthetic activity, including capacities for glucose synthesis, fatty acid production, and cholesterol synthesis. In contrast, the second metabolic subgroup, consisting of 9 rabbits, displayed an opposite metabolic profile activity to the first cluster, meaning a reduced fatty acid metabolism and increased biosynthetic activity. In detail, metabolic cluster 1 was marked by a higher fatty acid uptake ($p = 0.001$), very low-density lipoprotein (VLDL) export ($p = 0.002$), TAG synthesis ($p = 0.001$) and TAG content ($p = 0.01$), ketone body production ($p = 0.001$), acetylacetoacetic acid (ACAC) production ($p = 0.001$) and glutamine exchange ($p = 0.001$), although it exhibited lower cholesterol synthesis ($p < 0.01$). No significant differences were found in SWS ($p = 0.89$) between the two metabolic clusters. However, there was a tendency towards higher PR values in the first metabolic cluster compared to the second ($p = 0.065$), although not statistically significant. Table 7 below summarizes the significant differences observed in the wide range of metabolic capacities analyzed. Regarding the distinction between stiff and soft livers in terms of metabolic differences, stiffer livers demonstrate a significantly higher capacity for gluconeogenesis (-52.8 ± 9.5 vs. -42.6 ± 6.2 $\mu\text{mol/g/h}$ in soft livers, $p = 0.016$), increased cholesterol synthesis (0.25 ± 0.04 vs. 0.23 ± 0.01 $\mu\text{mol/g/h}$ in soft livers), and lower TAG content (35.3 ± 2.5 vs. 37.3 ± 1.3 mM vs in soft livers, $p = 0.043$). Figure 15 illustrates the significant differences in maximum metabolic capacities between soft and stiff liver clusters [56].

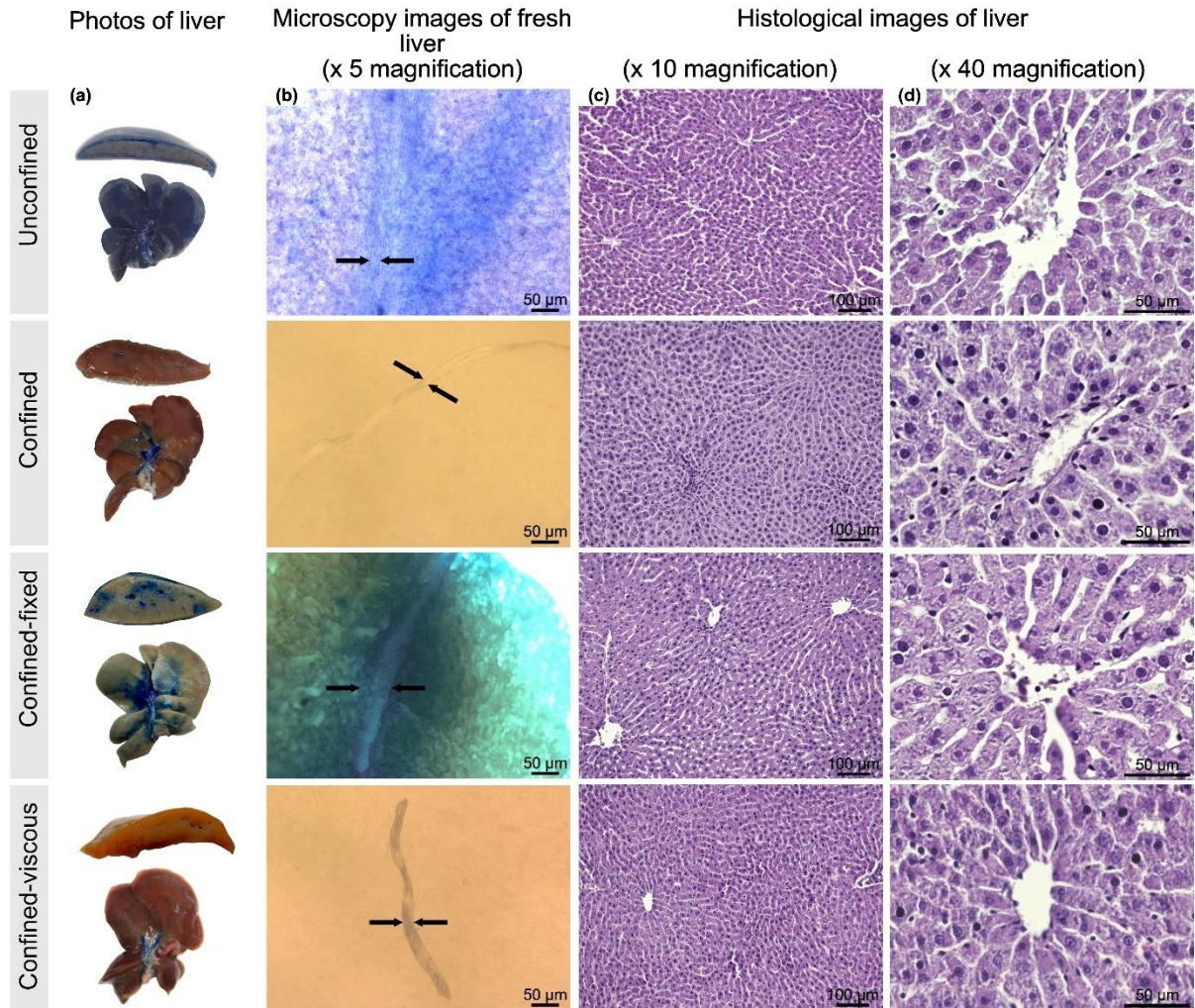


Figure 14: Photos and microscopy images of livers in unconfined, confined, confined-fixed and confined-viscous scenarios. (a) Photographs of livers after mp-MRI showing the whole liver as well as the cross-sectional area of the median liver lobe. (b) Microscopy images of thin liver pieces (ca. 1 mm) manually sliced from the livers shown in (a), blood vessels are indicated by the arrows, the images were taken at $\times 5$ magnification. Livers in (c) and (d) were processed for histology and stained with H&E. With $\times 10$ magnification, sinusoids are visible in (c). In (d), central vein and the surrounding hepatocytes are well depicted with $\times 40$ magnification [55] (Figure from Safranou *et al.* (2023)).

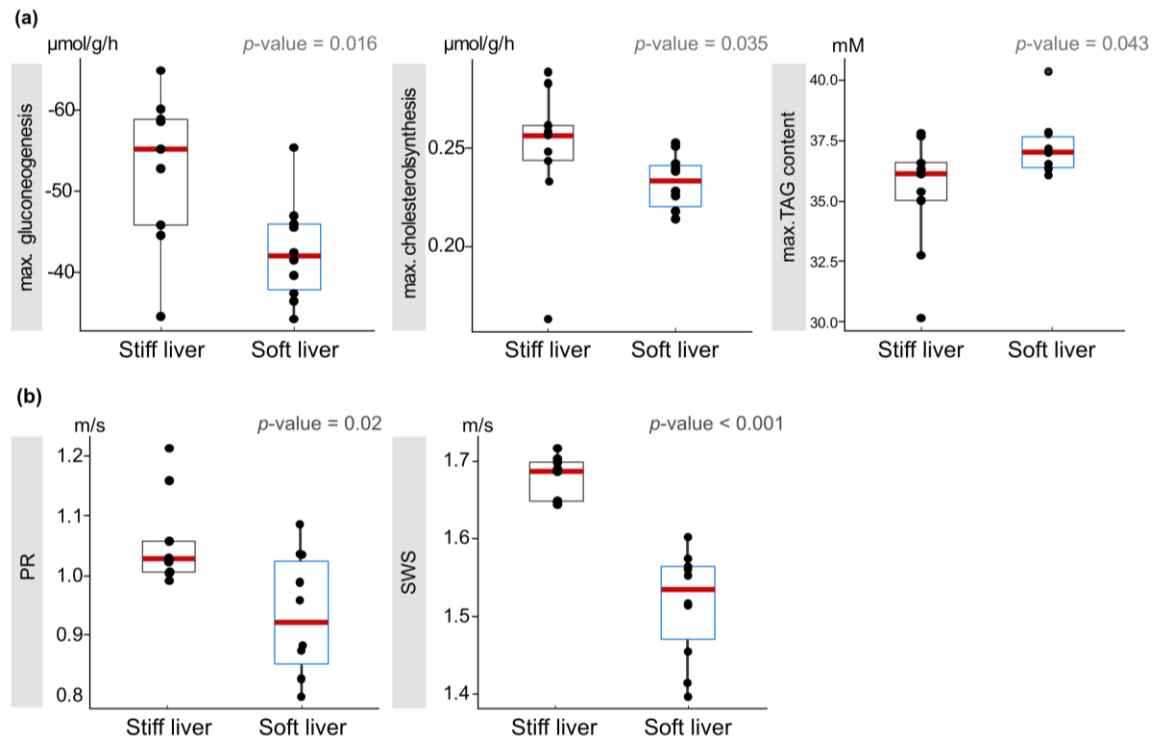


Figure 15: (a) Boxplots illustrating significantly different metabolic capacities between the stiff and the soft liver groups. (b) Boxplots depicting differences in PR and SWS between stiff and soft liver groups. The center line in red represents the median value. The box represents the interquartile range, and the whiskers extend to values within 1.5 times the interquartile range. Outliers are shown as dots. TAG stands for Triacylglycerol [56] (Figure adapted from Shahryari *et al.* (2023)).

Table 7: The maximum metabolic capacities of fatty acid metabolism and biosynthetic processes in two distinct metabolic clusters of healthy rabbit liver samples. The table presents mean and SD values for various metabolic parameters, along with corresponding p -values indicating significant differences between the two clusters [56].

Maximum metabolic capacity	Metabolic cluster 1		Metabolic cluster 2		p -value
	mean	SD	mean	SD	
	Fatty acid uptake (µmol/g/h)	34.7	1.6	31.6	
VLDL export (µmol/g/h)	5.2	0.5	4.6	0.6	0.002
TAG synthesis (µmol/g/h)	16.3	1.4	14.2	1.7	0.001
TAG content (mM)	37.5	1.3	35.4	2.3	0.01
Ketone body production (µmol/g/h)	32.9	4.0	23.3	6.3	0.001
ACAC production (µmol/g/h)	22.0	3.6	12.6	2.3	0.001
Ammonia uptake (µmol/g/h)	16.5	0.7	17.3	0.5	0.013
Glutamine exchange (µmol/g/h)	-7.6	3.0	-13.0	3.2	0.001
Urea production (µmol/g/h)	21.0	3.9	14.3	3.9	0.002

4.2.3 Study 3: Comparison of high-resolution SWS, φ maps and histology

Figure 16 depicts a comparison between SWS and φ maps with histological images stained using H&E and TH. Both H&E and TH fluorescent antibody staining successfully identified neuroblastoma cells, with cancerous cells stained in purple on the H&E-stained slides and by fluorescent green in the TH-stained slides. Anatomical and cellular features identified on the zebrafish histological slides agreed remarkably well with features visible in the SWS and φ maps.

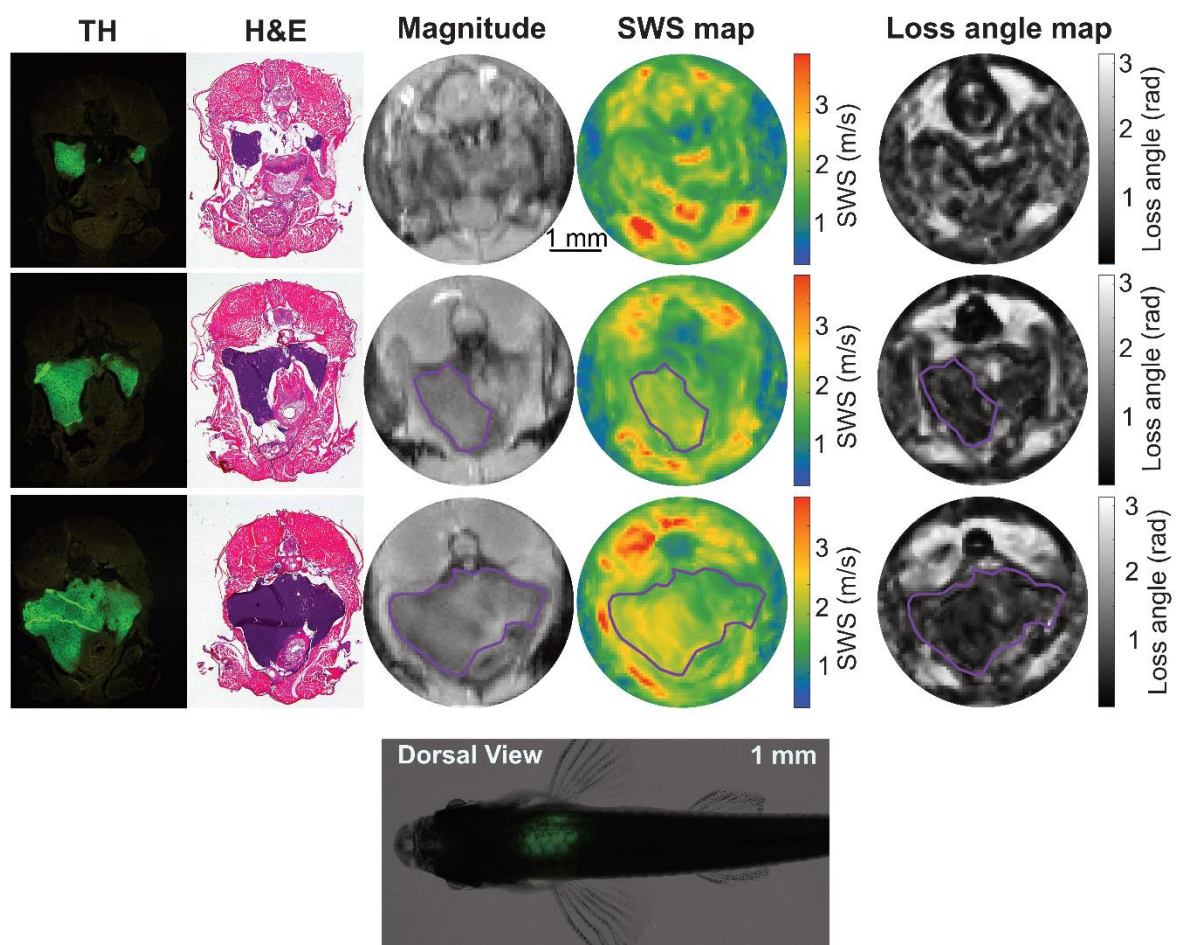


Figure 16: Comparison of SWS and φ maps with histology. Tyrosine hydroxylase ((TH) and H&E staining highlight cancer tissue in green (TH) and purple (H&E), respectively. It is important to note the difference in slice thicknesses between both methods, as histology images being significantly thinner ($< 4 \mu\text{m}$) compared to MRE slices ($600 \mu\text{m}$). Cancer tissue is contoured in purple [57] (Figure from Jordan *et al.* (2021)).

4.3 Correlation analyses

4.3.1 Study 1: Linear mixed model analyses

Linear mixed model analysis with inflow pressure as a fixed effect showed a positive correlation between portal pressure and VTVF in all groups (unconfined: $p < 0.001$; confined: $p < 0.001$; confined-fixed: $p < 0.001$; confined-viscous: $p < 0.001$) and ADC (unconfined: $p < 0.001$; confined: $p < 0.001$; confined-fixed: $p < 0.001$; confined-viscous: $p < 0.001$). The correlation between hepatic stiffness and portal pressure was negative in unconfined and confined-fixed livers, while positive in confined-viscous livers. No correlation was observed between SWS and pressure in confined scenarios. Significant correlations were found between every imaging parameter pair in all groups except for the correlation between SWS and ADC in confined livers [55]

4.3.2 Study 2: Correlation of metabolic functions with MRE parameters

Although not statistically significant, a declining trend in PR was observed alongside a significant increase in fatty acid metabolism and a reduction in biosynthetic capacities. Furthermore, a linear correlation between PR and SWS was identified, suggesting that such imaging parameters may be related to hepatic metabolic activity in the healthy rabbits. Our findings suggest that liver inverse viscosity, as measured by MRE, can distinguish between subclasses within healthy livers based on metabolic functionality. Moreover, the differentiation between stiff and soft livers could aid in the classification of metabolic functionality. However, it remained unclear whether MRE is effective in evaluating individual metabolic functions. To address this uncertainty, correlation between specific metabolic liver functions and liver stiffness and inverse viscosity were investigated. PR was found to correlate with urea production ($R = -0.5$, $p = 0.029$) and glutamine exchange ($R = -0.47$, $p = 0.042$). Furthermore, a significant correlation between SWS and gluconeogenesis ($R = -0.5$, $p = 0.028$) was found. Notably, a significant correlation between SUV and gluconeogenesis ($R = -0.72$, $p = 0.02$), but not with glucose uptake was observed.

5 Discussion

5.1 Summary of results

Within the scope of this thesis, we have designed experiments to address three main research questions:

In study 1, we aimed to define the distinct contributions of the poroelastic fluid and solid compartments to the macroscopic biomechanical liver properties. To achieve this, we designed four experimental scenarios with variations in fluid viscosity, organ confinement and tissue crosslinking. Our findings revealed hepatic softening across all scenarios, marked by elevated ADC and VTFV, except in the confined-viscous livers where stiffening occurred. This stiffening was attributed to the use of a higher viscosity inflow solution, leading to the retention of fluid primarily within the vessels. This highlighted the pivotal role of inflow viscosity in modulating macroscopic biophysical properties and demonstrated how alterations in fluid content and vascular permeability substantially influenced liver stiffness. When analyzing biomechanical liver properties, combining SWS and ADC measurements was essential to understand the complex macro-interactions between fluid and solid components as well as the underlying microstructural alterations [55].

Expanding on our initial investigation, study 2 explored the influence of hepatic metabolic activity on liver viscoelastic properties, particularly focusing on stiffness and viscosity. To this end, we imaged healthy female rabbits using a PET/MRI scanner, followed by ex vivo tissue analysis for metabolic capacities. Our findings revealed differences among healthy subjects in fatty acid metabolism and biosynthetic activity, which were associated with variations in liver PR. Furthermore, a potential second cluster based on the SWS cut-off value of 1.6 m/s distinguished groups of soft and stiff livers with differences in TAG content, glucogenesis capacity and cholesterol synthesis. These findings suggested the potential implication of metabolic alterations in shaping the biophysical properties of the healthy and possibly, diseased liver [56].

Building upon our results in studies 1 and 2 on the effects of macro poroelastic interactions and metabolic influences on liver mechanics, study 3 aimed to improve the sensitivity of MRE to heterogeneous tissue composition and various microarchitectures.

This was achieved by increasing the image resolution to a near microscopic scale, enabling a more specific examination of mechanical properties. In adult zebrafish, maps of SWS and φ generated at 60 μm in-plane resolution and a slice thickness of 600 μm demonstrated substantial mechanical differences between brain subregions and revealed consistent anatomical features with histology. Leveraging a neuroblastoma-bearing zebrafish strain allowed us to conclude that tumor tissue was softer and less fluid than muscle and whole brain tissue, further demonstrating the sensitivity of macroscopic MRE parameters to tissue cellular composition. [57].

5.2 Interpretation of results

5.2.1 Study 1: The Impact of varied fluid distribution patterns on liver biophysical properties detected through complementary SWS and ADC analysis

In study 1, we observed different biophysical responses emerging from distinct fluid distribution patterns. The unconfined scenario where livers were embedded in a soft matrix exhibited the most pronounced vascular dilatation coupled with a substantial increase in fluid volume, as evidenced by ADC measurements. Histological observations conducted in unconfined livers revealed severe disruption of cellular and vascular structural components. The highest vascular leakage was observed, resulting in the accumulation of significant fluid amounts within the ECM space. This led to a notable impairment of hepatic trabecular arrangement and central venous membranes, attributed to the fluid transfer from the vessel lumen to the ECM [55].

Previous studies [33, 61, 62] have demonstrated that compression of biological tissues could result in the alignment of deformable structural networks and stiff inclusions (such as fibrous networks, cells and ECM) resulting in tissue stiffening. However, our unconfined livers exhibited significant softening in response to vascular dilatation. It is plausible that the unconfined livers experienced compression stiffening due to vascular dilation under increasing pressure. However, In this context, it was believed that the compromised ECM integrity leading to macroscopic softening had a greater effect than compression stiffening [55].

For all three confined scenarios, the livers were embedded in a stiffer medium to prevent volumetric expansion beyond non-physiological levels. This setup created conditions similar to encapsulated, pressurized livers in vivo, thereby intensifying the

compressive effect of vascular dilation on the surrounding tissue. However, despite similar embedding, livers responded differently to increasing portal pressures.

The confined-viscous liver showed the highest increase in VTVF and ADC among all scenarios. The gum Arabic-based inflow solution tested in this scenario differed from the PBS used in all other scenarios, due to its higher molecular weight, hydrophilic nature and elevated viscosity. The (-OH) groups present in the sugar polymers forming the gum macromolecule prompted the formation of hydrogen bonds with water molecules, effectively binding them to its molecular structure. Based on the full liver and lobe cross-section images, along with microscopic observations depicted in figures 14.a, b, c and d respectively, it appeared that the restricted diffusion of free water molecules through the vessel walls prevented their accumulation within the ECM. This resulted in macroscopic tissue stiffening, which is the opposite biomechanical response compared to the other scenarios [55]. Furthermore, the compression-induced rearrangement of hepatocytes, likely imposed as the liver tissue underwent progressive vascular dilation, may have contributed to the observable stiffening effect [33, 51, 55, 61, 62].

In the confined-fixed scenario, in-situ formaldehyde fixation induced multiple structural alterations in the livers. Initially, lower vascular compliance and elevated baseline stiffness were observed. Vascular remodeling included dilatation and cross-linking under the influence of portal perfusion at physiological flow rates. This resulted in markedly high vessel volumes leading to the highest VTVF and ADC values observed at baseline compared to other scenarios [63, 64]. At a microscopic level, formaldehyde might have potentially dissolved lipids in cellular membranes during the fixation process, resulting in increased cell permeability [33, 34]. Consequently, and similar to the unconfined livers, the accumulation of fluid in the ECM, facilitated by the expanded vascular spaces might have resulted in macroscopic softening upon portal pressure increase [55].

Finally, in the confined scenario where no significant changes in hepatic stiffness were noted, the strong confinement appeared to diminish the mechanical effect of increased portal pressures, despite a significant elevation in VTVF and ADC. Our analysis suggests these alterations were insufficient to prompt either compression stiffening or changes in vascular permeability, resulting in insignificant biomechanical effects [55].

We examined in study 1, the impact of short-term fluctuations in physiological factors, such as inflow pressure, on liver biomechanics. We demonstrated how alterations in

parameters pertaining to poroelasticity in the liver may affect the cellular structure and vascular permeability, resulting in distinct fluid amounts and distribution that modulate the macro-mechanical responses. Our first study underlines the importance of ADC and SWS as complementary imaging markers in understanding the intricate fluid to solid dynamics. Elevated hydrostatic pressure directly correlated with increased vessel volume and higher ADC values. However, the response of stiffness showed variability. We propose that ADC is a more specific imaging parameter for assessing the integrity of hepatic cellular structure and the compliance of vessels in response to increased fluid amounts. Conversely, SWS provided insight into tissue composition, hinting at the fluid to solid ratio, and the fluctuations in vascular permeability [55, 65].

5.2.2. Study 2: Metabolic heterogeneity in healthy liver specimen modulates stiffness and viscosity

In our subsequent study 2, we aimed to address the long-term metabolic adaptations [56, 66] and their impact on liver biomechanics, expanding on our findings in study 1. Previous research has highlighted the association between excessive fibrotic deposition in the ECM and the dysfunctions in various central metabolic pathways [44, 67-69]. It was also reported that hepatic stiffness increased in patients with liver fibrosis due to fibroblast activation and the consequent matrix remodeling and collagen accumulation [16, 21, 25, 27, 33, 44, 70-72]. Hence, it is plausible to examine whether alterations in liver biomechanical parameters could originate from alterations in metabolic functions. To meet our long-term metabolic monitoring needs, we have opted to measure metabolic liver capacities instead of metabolic fluxes, a method which considers the variability in physical activity, plasma nutrients and hormone profiles [73-75]. Our analysis facilitated a more comprehensive approach by evaluating 16 different metabolic capacities based on protein abundance. [66]. In genetically identical healthy female rabbits fed the same diet and fasted two hours before the measurement, we observed large heterogeneities in metabolic profiles [56, 76, 77]. The differences observed in metabolic capacities led to the identification of two distinct clusters: Cluster 1 had increased fatty acid metabolism and reduced biosynthetic capacity, while cluster 2 had the opposite metabolic profile. The biomechanical properties of the two metabolic clusters also differed, as cluster 1 had a higher viscosity (lower PR) than cluster 2, although this difference was not statistically

significant, likely due to the low number of animals recruited in the study [56]. A similar trend, albeit non-significant, was noted in PET measurements, with cluster 1 exhibiting slightly higher SUV values compared to cluster 2. However, due to the limited subset of only 10 rabbits used in this analysis, definitive conclusions on SUV could not be drawn. In addition to the metabolic clustering, our findings introduced a second method of classification based on hepatic stiffness, by applying a cutoff value of SWS (1.6 m/s). Consistent with prior research [42, 78-82], stiffness values below 1.6 m/s indicated healthy livers, whereas values exceeding 1.6 m/s suggested a potential predisposition for compensated advanced chronic liver disease (cACLD) or hepatic fibrosis in apparently healthy subjects [42, 78-82]. Stiffer livers in our study were marked by metabolic differences compared to softer ones, as they exhibited reduced TAG content versus an increased capacity for gluconeogenesis and cholesterol synthesis. This observation aligns with previous research conducted by Abuharum *et al.*, which associates hepatic adipose tissue, characterized by excessive lipid accumulation, with higher stiffness [83]. Moreover, the impairment of TAG synthesis resulting in abnormally low TAG content, might contribute to the pathogenesis of fatty liver disease [84]. Higher hepatic stiffness values may serve as a potential predisposing factor for NAFLD, preceding liver fibrosis in the progression of non-alcoholic steatohepatitis (NASH). However, it is important to note that this association represents a potential relationship, and further research is required to establish causality.

We also investigated the direct correlations between liver metabolic functions and biomechanical parameters as depicted in figure 15. Notably, lower viscosity (higher PR) was associated with lower urea production and glutamine exchange. Glutamine plays a crucial role in nitrogen regulation working in conjunction with ammonia from portal venous blood to enhance the urea cycle [85]. This metabolic interdependence may explain the correlation findings related to PR. In subjects with non-alcoholic fatty liver disease/non-alcoholic steatohepatitis (NAFLD/NASH), greater effects would be anticipated, as larger differences in biomechanical parameters would be observed [24, 26, 30, 86]. For example, MRE analysis conducted in children with NAFLD has shown an increase in microscopically detected steatosis that correlated with a decrease in hepatic stiffness and, with an increase in viscosity. These findings are in line with our correlation results, in which stiffer livers exhibited increased viscosity, and fatty acid metabolism but impeded biosynthetic capacity [23].

Study 2 uncovers the potential association between metabolic capacities assessed through proteomics-based modelling and hepatic biomechanical parameters as measured by MRE in vivo. Our findings suggest that variations in metabolic functions are correlated with biomechanical differences. Consequently, hepatic stiffness and viscosity could serve as non-invasive, sensitive markers of crucial liver functions. Moreover, they may serve as early indicators of metabolic abnormalities.

5.2.3. Study 3: Micromechanical SWS and φ are sensitive to microarchitectural differences constituting the zebrafish brain

Our results in study 3 suggested the zebrafish as an advantageous model to examine the relationship between cellular and microarchitectural factors, and macroscopic biomechanical properties of soft tissue [37, 87, 88]. The zebrafish's compact size made it well-suited for simultaneous MRI/MRE imaging and histology analyses, both performed on comparable regions. Additionally, the zebrafish brain exhibited diverse neuronal connectivity patterns across its various subregions, which potentially influenced its mechanical properties [89, 90]. Indeed, stiffness was found to be higher in the MB region compared to the OT, likely due to differences in microstructure: while the OT structure is described as laminar and consists of fewer, well-aligned neuronal fibers, the mesencephalic, MB structure is dominated by abundantly crosslinked neuronal fibers [91]. In addition, our experiment further revealed that neuroblastoma was significantly softer and less viscous than healthy muscle and whole brain tissue. This is consistent with the glioblastoma signature in the human brain, characterized by low collagen content, contributing to its fluid-like behavior [92]. Our high-resolution method demonstrated sensitivity to microstructural variability by capturing heterogeneities identifiable in both, histological images and mechanical maps of SWS and φ .

5.3 Embedding the results into the current state of research

In all three studies, our experiments were designed to decipher the complex interplay between vascular hemodynamics, pluricellular structure and metabolic function, and their influence on soft tissue biomechanics. All these factors hold clinical significance, as they are interrelated in hepatic disease diagnosis, [93, 94].

In study 1, hemodynamic parameters such as the portal pressure, vascular compliance and viscosity of the inflow solution were experimentally manipulated. Previous research

conducted among cirrhotic patients has substantiated the clinical relevance of these factors, as manifested by pathologically elevated portal pressures [80, 81], increased effective vascular compliance [82, 83], and reduced plasma viscosity [84, 85]. Moreover, it was proven that [95], a more accurate prediction of portal hypertension can be achieved by combining hepatic structural measures (such as liver T1 mapping) with hemodynamic examinations (such as splanchnic flow) instead of solely relying on T1 mapping, phase-contrast MRI and arterial spin labeling. This underscores the importance of considering solid-fluid tissue interactions in understanding pathologies like portal hypertension, where vascular resistance, influenced by the distortion of hepatic architecture due to fibrogenesis impacts both hepatic and splanchnic circulation [55, 96].

As for study 2, the clinical relevance underlies understanding the long-term architectural changes associated with metabolic alterations in the liver that can have significant implications in disease diagnosis and prevention. For instance, detecting increased TAG storage could serve as a biomarker for disrupted fatty acid metabolism indicating a potential risk of developing conditions like NAFLD/NASH [97]. A second example is the effect of fibrosis progression on hepatic perfusion and blood flow availability within hepatocytes. By assessing alterations in glucose metabolism resulting from changes in blood flow dynamics, clinicians may better monitor disease progression or customize prevention strategies.

Although our findings from study 3 may not directly impact clinical diagnosis in patients, it is noteworthy to acknowledge the similarities between zebrafish and humans in developmental biological processes, rendering zebrafish valuable for researching various conditions including cancer, liver diseases, and blood disorders [98]. Moreover, the conservation of human structural and mechanical tumor signatures supports the utility of these vertebrate models in translational research [98]. The zebrafish model, which is biologically simple, of relatively small size and transparent, allowed us to achieve the highest possible resolution in MRE imaging and to reach a greater mechanical specificity.

The proposed redefinition of NAFLD to metabolic-associated fatty liver disease (MAFLD) provides compelling grounds to explore the complexity of hepatic diseases using MRE [98, 99]. MAFLD diagnosis covers a wider spectrum of hepatic conditions and accurately reflects their metabolic origins. It involves liver biopsy, imaging (such as

ultrasound or MRI), assessment of portal hypertension, and analysis of blood biomarkers for metabolic dysregulation. This novel diagnostic approach provides a comprehensive characterization of MAFLD by investigating three key factors: hemodynamic properties, metabolic abnormalities, and microstructural alterations, all central to our research within this thesis [98, 99]. The redefinition of NAFLD to MAFLD highlights the relevance of our experimental design and findings. The combination of MRE and mp-MRI measurements used in this thesis has consistently revealed distinct viscoelastic responses to increased portal pressure, heterogenous hepatic metabolism in healthy livers, and variations in cytoskeletal and cellular structure aligning with tissue and metabolic characterization. Based on our findings, biomechanical properties obtained by MRE holds promise as noninvasive biomarkers which provide insights into liver functionality.

At a resolution comparable to that of histological images or higher, the molecular basis of viscoelastic properties remains largely unknown. For instance, it would be interesting to explore the sinusoidal and peri-sinusoidal effects on cellular mechano-sensing towards a more specific understanding of cellular function and structure through viscoelastic principles [1, 99]. In figure 17 we sketch the approach adopted within this thesis to simplify the complexity of hepatic pathophysiology and collect parameters of clinical significance, that potentially alter liver biophysical parameters.

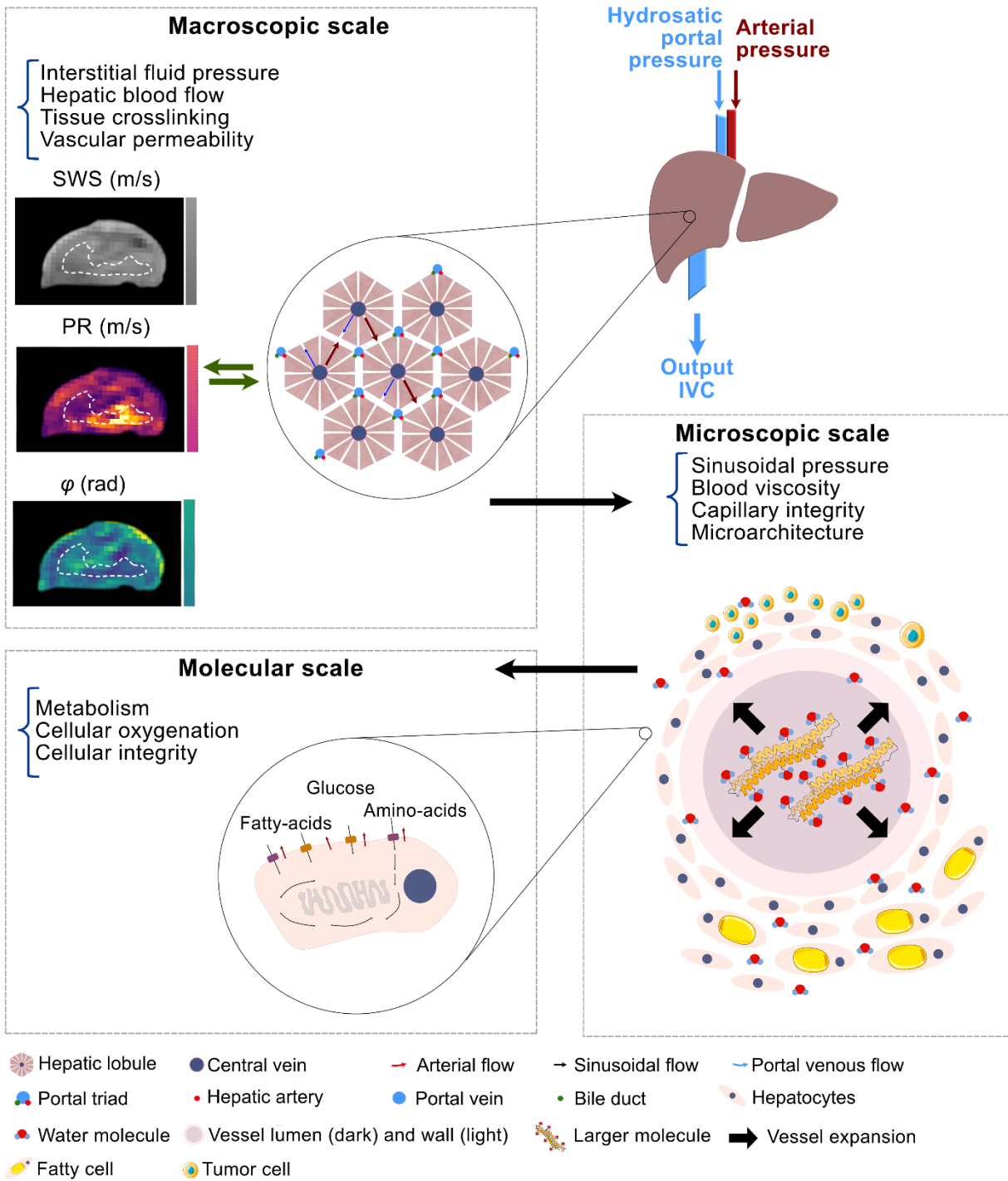


Figure 17: Depicts biological changes occurring across various scales within the liver. Starting with an overview of the liver, the diagram progressively zooms in to the macrostructural level, showing how alterations in poroelastic properties translate into changes in liver biomechanical parameters, represented on a rodent abdomen (SWS, PR, and ϕ). Further magnification reveals microscopic changes in sinusoidal pressure, microarchitecture, and the overall exchange between sinusoids and the extracellular matrix (ECM). Metabolic alterations taking place at the molecular level are also illustrated. These different scales collectively contribute to the overall changes in hepatic biophysical properties, a pattern applicable to organs with comparable structures [7] (Figure inspired from Hirsch *et al.* (2017)).

5.4 Limitations

While the findings of this thesis are promising, there are limitations.

In study 1, mp-MRI and MRE measurements on ex vivo livers were conducted at room temperature, rather than at physiological temperatures. Hence, a thorough investigation into the thermic impact on liver mechanical and metabolic parameters is crucial before extrapolating to in vivo measurements. While liver fat content was not quantified, it is worth noting that we exclusively examined young adults and healthy rats and post-mortem histology analyses revealed no significant presence of hepatic fat. Moreover, potential post-mortem tissue alterations such as minor blood occlusions in ex vivo livers should be considered. However, given our focus on relative variations in mechanical parameters, any effects if existing, were likely minimal [55].

Regarding the tissue samples used post-mortem in study 2, their small sizes may result in disregarding possible metabolic heterogeneities within the same liver. Nevertheless, as we studied healthy animals, it is unlikely that such heterogeneity will affect our experimental outcomes. Moreover, in vivo measurements were performed in anesthetized rabbits and their heart rate and blood flow might be affected by the sedation process. However, with consistent conditions across all measured animals, such effects are believed to be negligible [56].

As for study 3, similar limitations may arise from post-mortem tissue alterations (blood coagulation) requiring similar considerations as previously mentioned in study 1. In terms of mapping SWS and φ , in-plane resolution comparable to microscopic resolution was achieved. However, due to the limitations of the scanner, achieving microscopic slice thickness remained challenging. Therefore, our interpretation of the mechanical effects on the microscopic level should consider this limitation in slice thickness [57].

For all our studies, it is necessary to acknowledge that we applied multifrequency MRE measurements with higher frequency ranges adjusted for preclinical studies on small animals. Therefore, comparisons of our data with human studies should be made with caution [57].

5.5 Implications for practice and/or future research

To the best of my knowledge, each of the three studies addressed novel research questions using innovative methodologies that were not documented before. Further studies are planned to support the findings presented in this manuscript.

In study 1, it would be relevant to investigate the influence of fluid viscosity within the range of PBS viscosity to that of a 20% Arabic gum solution for each pressure level and scenario. Further research could explore the influence of inflow solutions containing molecules of increasing weights on vascular permeability, and how this affects hepatic stiffness and water diffusivity. Moreover, exploring the compression modulus as a novel biophysical marker for pressure elevation or vascular compliance may further expand the scope of the study. Correlating hepatic compression modulus with changes in tissue stiffness under compression-stiffening conditions could provide valuable insights into the vessel-to-tissue interactions.

In study 2, investigating pathological metabolic variations on liver biomechanical parameters, such as SWS and PR, may be a promising continuation. To achieve this, a cross-sectional NAFLD/NASH preclinical model could be investigated. Utilizing a well-documented feeding animal model would allow for the observation of the mechanical progression of NAFLD/NASH. At each timepoint, conducting histopathological scoring for fat, inflammation, and fibrosis could provide valuable insights into microstructural alterations. Furthermore, using proteomics-based modelling of metabolic capacities could offer valuable information regarding the correlation between metabolic pathways in NAFLD/NASH and changes in liver viscoelastic properties as measured by MRE.

For study 3, a highly valuable continuation would involve replicating similar measurements in in-vivo zebrafish and larvae, utilizing a sedative solution dissolved in water. This approach would enable further quantitative biomechanical research on the zebrafish as a clinically relevant animal model. Additionally, it would be of high interest to develop a method capable of directly analyzing viscoelastic parameters from very small tissue samples and cell cultures. One potential approach could involve inducing shear waves in small tissue samples and capturing motion optically using a high-speed camera [100]. Viscoelastic parameter reconstruction could then be pursued based on optical flow motion algorithms. This would allow access to a novel approach that will overcome the resolution limit set by the MRI scanners, offering a more refined analysis of viscoelastic properties.

6 Conclusion

The detection and diagnosis of liver disease can be challenging due to the complex underlying pathological processes that result in subtle and overlapping structural and functional changes. In addition to standard serum markers and invasive biopsy-based histopathology, non-invasive quantitative imaging is promising for examining patients with liver diseases. MRI and ultrasound techniques are highly desirable to comprehensively characterize the diseased liver, from both structural and functional perspectives. MRE is an MRI technique that quantifies hepatic viscoelastic properties which are sensitive to matrix alterations or portal hypertension. However, the individual contribution and corresponding biomechanical manifestation of disease features, such as liver composition, structure, and hemodynamics, remain incompletely understood and require further study. Therefore, this thesis focused on conducting preclinical experiments to study isolated hemodynamic, metabolic and microstructural effects, and their influence onto the coarse-grained mechanical properties of the liver, to better understand the parameter changes measured by MRE.

In study 1, we investigated the correlation between portal pressure and hepatic biophysical properties using *ex vivo* rat livers and multiparametric MRI techniques, including MRE and DWI. By controlling portal pressure and fluid content, we quantified vascular dilatation, tissue stiffness and water diffusion. Our findings suggested a correlation between elevated portal pressures and increased vascular volumes and water diffusivity. We also demonstrated that hepatic stiffening occurred as portal pressure increased, particularly when inflow perfusion fluid was retained within the vessels, similar to conditions observed in patients with portal hypertension. Furthermore, we showed that increased vascular permeability and microstructural damage led to hepatic softening. Based on our experimental results, we propose SWS and ADC as novel non-invasive imaging markers for evaluating liver parenchymal injury and hepatic sinusoidal hyperpermeability associated with portal hypertension.

In study 2, we demonstrated the correlations between liver metabolism assessed by proteomics-based modeling, and MRE-measured *in vivo* liver biomechanical parameters in rabbits. Our results showed metabolic variations in healthy livers, particularly in carbohydrate metabolism, ketone body synthesis, and fatty acid metabolism. By establishing a stiffness cutoff value, we could distinguish between stiff and soft livers with quantifiable differences in TAG content, gluconeogenesis capacity,

and cholesterol synthesis. Our findings suggested that liver stiffness and viscosity derived from MRE hold promise as non-invasive markers for assessing metabolic reserve capacity in the liver.

In study 3, we introduced a novel MRE protocol utilizing a 7T animal scanner for post-mortem evaluation of biomechanical tissue parameters in zebrafish, achieving an unprecedented in-plane resolution of $60 \mu\text{m}^2$. Through our post-processing method, we were able to obtain high-resolution SWS and φ maps as proxies of stiffness and tissue fluidity respectively. These maps allow the visualization of distinct anatomic features comparable to those revealed by histology images. Our findings demonstrated significant heterogeneity in stiffness and tissue fluidity and allowed the differentiation between brain subregions, as well as healthy versus tumor tissues. Furthermore, they indicated that microstructure may influence MRE-measured macroscopic parameters, which are closer to microscopic resolutions than standard clinical and preclinical MRE parameters. This provides a foundation for further exploration of biomechanical tissue parameters at the cellular scale.

In conclusion, this thesis examined the impact of alterations in pathological parameters, particularly those pertaining to vascular function, microstructure, and metabolism, on the macroscopic biophysical properties of the liver, as assessed by mp-MRI and MRE. Additionally, it demonstrated the viability and sensitivity of MRE across diverse species. For future clinical translation, our research demonstrates the potential to identify specific effects within the mechanical complexities of multilayered liver diseases, which could lead to more accurate diagnoses and effective disease monitoring.

Reference list

- [1] S. Mueller, *Liver Elastography*, Springer 2020.
- [2] J. Smith, Nuclear magnetic resonance absorption, *Quarterly Reviews, Chemical Society* 7(3) (1953) 279-306.
- [3] R. Damadian, Tumor detection by nuclear magnetic resonance, *Science* 171(3976) (1971) 1151-1153.
- [4] D.S. Tuch, T.G. Reese, M.R. Wiegell, N. Makris, J.W. Belliveau, V.J. Wedeen, High angular resolution diffusion imaging reveals intravoxel white matter fiber heterogeneity, *Magnetic Resonance in Medicine: An Official Journal of the International Society for Magnetic Resonance in Medicine* 48(4) (2002) 577-582.
- [5] R.K. Sterling, A. Duarte-Rojo, K. Patel, S.K. Asrani, M. Alsawas, J. Dranoff, M.I. Fiel, M.H. Murad, D.H. Leung, D. Levine, AASLD Practice Guideline on imaging-based non-invasive liver disease assessments of hepatic fibrosis and steatosis, *Hepatology* (2024) 10.1097.
- [6] A.B. Chowdhury, K.J. Mehta, Liver biopsy for assessment of chronic liver diseases: a synopsis, *Clinical and experimental medicine* 23(2) (2023) 273-285.
- [7] S. Mueller, *Liver elastography, Clinical Use and Interpretation*: Springer, Cham (2020).
- [8] S. Hirsch, J. Braun, I. Sack, *Magnetic resonance elastography: physical background and medical applications*, John Wiley & Sons 2017.
- [9] M. Yin, J.A. Talwalkar, K.J. Glaser, A. Manduca, R.C. Grimm, P.J. Rossman, J.L. Fidler, R.L. Ehman, Assessment of hepatic fibrosis with magnetic resonance elastography, *Clinical Gastroenterology and hepatology* 5(10) (2007) 1207-1213. e2.
- [10] A.M. Torres Rojas, S. Lorente, M. Hautefeuille, A. Sanchez-Cedillo, Hierarchical modeling of the liver vascular system, *Frontiers in physiology* (2021) 1946.
- [11] S. Lorente, M. Hautefeuille, A. Sanchez-Cedillo, The liver, a functionalized vascular structure, *Scientific Reports* 10(1) (2020) 1-10.
- [12] D. Sasse, U.M. Spornitz, I.P. Maly, Liver architecture, *Enzyme* 46(1-3) (1992) 8-32.
- [13] J. Birnie, J. Grayson, Observations on temperature distribution and liver blood flow in the rat, *The Journal of physiology* 116(2) (1952) 189.
- [14] M.R. Islam, J. Virag, M.L. Oyen, Micromechanical poroelastic and viscoelastic properties of ex-vivo soft tissues, *Journal of Biomechanics* 113 (2020) 110090.
- [15] P.R. Perriñez, F.E. Kennedy, E.E. Van Houten, J.B. Weaver, K.D. Paulsen, Modeling of soft poroelastic tissue in time-harmonic MR elastography, *IEEE transactions on biomedical engineering* 56(3) (2008) 598-608.
- [16] P. Asbach, D. Klatt, B. Schlosser, M. Biermer, M. Mucche, A. Rieger, C. Lodenkemper, R. Somasundaram, T. Berg, B. Hamm, J. Braun, I. Sack, Viscoelasticity-based staging of hepatic fibrosis with multifrequency MR elastography, *Radiology* 257(1) (2010) 80-6.
- [17] R. Reiter, M. Shahryari, H. Tzschätzsch, D. Klatt, B. Siegmund, B. Hamm, J. Braun, I. Sack, P. Asbach, Spatial heterogeneity of hepatic fibrosis in primary sclerosing cholangitis vs. viral hepatitis assessed by MR elastography, *Sci Rep* 11(1) (2021) 9820.
- [18] S.K. Venkatesh, M. Yin, R.L. Ehman, Magnetic resonance elastography of liver: clinical applications, *J Comput Assist Tomogr* 37(6) (2013) 887-96.
- [19] A. Manduca, P.J. Bayly, R.L. Ehman, A. Kolipaka, T.J. Royston, I. Sack, R. Sinkus, B.E. Van Beers, MR elastography: Principles, guidelines, and terminology, *Magn Reson Med* 85(5) (2021) 2377-2390.
- [20] Y. Qu, M.S. Middleton, R. Loomba, K.J. Glaser, J. Chen, J.C. Hooker, T. Wolfson, Y. Covarrubias, M.A. Valasek, K.J. Fowler, Magnetic resonance elastography

- biomarkers for detection of histologic alterations in nonalcoholic fatty liver disease in the absence of fibrosis, *European radiology* 31 (2021) 8408-8419.
- [21] M. Yin, K.J. Glaser, A. Manduca, T. Mounajjed, H. Malhi, D.A. Simonetto, R. Wang, L. Yang, S.A. Mao, J.M. Glorioso, F.M. Elgilani, C.J. Ward, P.C. Harris, S.L. Nyberg, V.H. Shah, R.L. Ehman, Distinguishing between Hepatic Inflammation and Fibrosis with MR Elastography, *Radiology* 284(3) (2017) 694-705.
- [22] S.B. Reeder, C.B. Sirlin, Quantification of liver fat with magnetic resonance imaging, *Magn Reson Imaging Clin N Am* 18(3) (2010) 337-57, ix.
- [23] C.A. Hudert, H. Tzschätzsch, B. Rudolph, C. Loddenkemper, H.-G. Holzhütter, L. Kalveram, S. Wiegand, J. Braun, I. Sack, J. Guo, How histopathologic changes in pediatric nonalcoholic fatty liver disease influence in vivo liver stiffness, *Acta biomaterialia* 123 (2021) 178-186.
- [24] M. Yin, K.J. Glaser, A. Manduca, T. Mounajjed, H. Malhi, D.A. Simonetto, R. Wang, L. Yang, S.A. Mao, J.M. Glorioso, Distinguishing between hepatic inflammation and fibrosis with MR elastography, *Radiology* 284(3) (2017) 694-705.
- [25] R. Reiter, M. Shahryari, H. Tzschätzsch, M. Haas, C. Bayerl, B. Siegmund, B. Hamm, P. Asbach, J. Braun, I. Sack, Influence of fibrosis progression on the viscous properties of in vivo liver tissue elucidated by shear wave dispersion in multifrequency MR elastography, *J Mech Behav Biomed Mater* 121 (2021) 104645.
- [26] B. Zhu, L. Wei, N. Rotile, H. Day, T. Rietz, C.T. Farrar, G.Y. Lauwers, K.K. Tanabe, B. Rosen, B.C. Fuchs, Combined magnetic resonance elastography and collagen molecular magnetic resonance imaging accurately stage liver fibrosis in a rat model, *Hepatology* 65(3) (2017) 1015-1025.
- [27] S. Singh, S.K. Venkatesh, R. Loomba, Z. Wang, C. Sirlin, J. Chen, M. Yin, F.H. Miller, R.N. Low, T. Hassanein, Magnetic resonance elastography for staging liver fibrosis in non-alcoholic fatty liver disease: a diagnostic accuracy systematic review and individual participant data pooled analysis, *European radiology* 26 (2016) 1431-1440.
- [28] A.A. de Schellenberger, H. Tzschätzsch, B. Polchlopek, G. Bertalan, F. Schrank, K. Garczynska, P.A. Janmey, J. Braun, I. Sack, Sensitivity of multifrequency magnetic resonance elastography and diffusion-weighted imaging to cellular and stromal integrity of liver tissue, *Journal of Biomechanics* 88 (2019) 201-208.
- [29] K. Garczyńska, H. Tzschätzsch, A.A. Köhl, A.S. Morr, L. Lilaj, A. Häckel, E. Schellenberger, N. Berndt, H.-G. Holzhütter, J. Braun, Changes in liver mechanical properties and water diffusivity during normal pregnancy are driven by cellular hypertrophy, *Frontiers in Physiology* 11 (2020) 605205.
- [30] A. Berzigotti, A. De Gottardi, R. Vukotic, S. Siramolpiwat, J.G. Abraldes, J.C. García-Pagan, J. Bosch, Effect of meal ingestion on liver stiffness in patients with cirrhosis and portal hypertension, *PLoS One* 8(3) (2013) e58742.
- [31] T. Meyer, H. Tzschätzsch, B. Wellge, I. Sack, T. Kröncke, A. Martl, Valsalva maneuver decreases liver and spleen stiffness measured by time-harmonic ultrasound elastography, *Frontiers in Bioengineering and Biotechnology* 10 (2022) 886363.
- [32] J. Guo, C. Büning, E. Schott, T. Kröncke, J. Braun, I. Sack, C. Althoff, In Vivo Abdominal Magnetic Resonance Elastography for the Assessment of Portal Hypertension Before and After Transjugular Intrahepatic Portosystemic Shunt Implantation, *Investigative Radiology* 50(5) (2015) 347-351.
- [33] M. Perepelyuk, L. Chin, X. Cao, A. Van Oosten, V.B. Shenoy, P.A. Janmey, R.G. Wells, Normal and fibrotic rat livers demonstrate shear strain softening and compression stiffening: a model for soft tissue mechanics, *PLoS one* 11(1) (2016) e0146588.

- [34] N. Heucke, T. Wuensch, J. Mohr, M. Kaffarnik, R. Arsenic, B. Sinn, T. Müller, J. Pratschke, M. Stockmann, I. Sack, Non-invasive structure–function assessment of the liver by 2D time-harmonic elastography and the dynamic Liver MAXimum capacity (LiMAx) test, *Journal of gastroenterology and hepatology* 34(9) (2019) 1611-1619.
- [35] G. Millonig, S. Friedrich, S. Adolf, H. Fonouni, M. Golriz, A. Mehrabi, P. Stiefel, G. Pöschl, M.W. Büchler, H.K. Seitz, Liver stiffness is directly influenced by central venous pressure, *Journal of hepatology* 52(2) (2010) 206-210.
- [36] G. Wang, W. Mao, R. Byler, K. Patel, C. Henegar, A. Alexeev, T. Sulchek, Stiffness dependent separation of cells in a microfluidic device, *PloS one* 8(10) (2013) e75901.
- [37] D. Mitrossilis, J. Fouchard, A. Guiroy, N. Desprat, N. Rodriguez, B. Fabry, A. Asnacios, Single-cell response to stiffness exhibits muscle-like behavior, *Proceedings of the National Academy of Sciences* 106(43) (2009) 18243-18248.
- [38] F. Bril, A. Sanyal, K. Cusi, Metabolic syndrome and its association with nonalcoholic steatohepatitis, *Clinics in Liver Disease* 27(2) (2023) 187-210.
- [39] T. Kawada, Nonalcoholic Fatty Liver Disease Without Metabolic-Associated Fatty Liver Disease and Metabolic Syndrome, *Clinical Gastroenterology and Hepatology* 21(9) (2023) 2435.
- [40] W.D. Means, *Stress and strain: basic concepts of continuum mechanics for geologists*, Springer Science & Business Media 2012.
- [41] I. Sack, T. Schaeffter, *Quantification of biophysical parameters in medical imaging*, Springer 2018.
- [42] I. Sack, *Magnetic resonance elastography from fundamental soft-tissue mechanics to diagnostic imaging*, *Nature Reviews Physics* (2022) 1-18.
- [43] Y.-c. Fung, *Biomechanics: mechanical properties of living tissues*, Springer Science & Business Media 2013.
- [44] R.G. Wells, *Tissue mechanics and fibrosis*, *Biochimica et Biophysica Acta (BBA)-Molecular Basis of Disease* 1832(7) (2013) 884-890.
- [45] O. Posnansky, J. Guo, S. Hirsch, S. Papazoglou, J. Braun, I. Sack, Fractal network dimension and viscoelastic powerlaw behavior: I. A modeling approach based on a coarse-graining procedure combined with shear oscillatory rheometry, *Phys Med Biol* 57(12) (2012) 4023-40.
- [46] J.M. Carcione, *Wave fields in real media: Wave propagation in anisotropic, anelastic, porous and electromagnetic media*, Elsevier 2007.
- [47] K. Parker, A microchannel flow model for soft tissue elasticity, *Physics in Medicine & Biology* 59(15) (2014) 4443.
- [48] A.H.-D. Cheng, *Poroelasticity*, Springer 2016.
- [49] A.-D. Cheng, Material coefficients of anisotropic poroelasticity, *International journal of rock mechanics and mining sciences* 34(2) (1997) 199-205.
- [50] L. Lilaj, T. Fischer, J. Guo, J. Braun, I. Sack, S. Hirsch, Separation of fluid and solid shear wave fields and quantification of coupling density by magnetic resonance poroelastography, *Magn Reson Med* 85(3) (2021) 1655-1668.
- [51] S. Hirsch, J. Guo, R. Reiter, E. Schott, C. Büning, R. Somasundaram, J. Braun, I. Sack, T.J. Kroencke, Towards compression-sensitive magnetic resonance elastography of the liver: Sensitivity of harmonic volumetric strain to portal hypertension, *Journal of Magnetic Resonance Imaging* 39(2) (2014) 298-306.
- [52] H. Tzschätzsch, J. Guo, F. Dittmann, S. Hirsch, E. Barnhill, K. Jöhrens, J. Braun, I. Sack, Tomoelastography by multifrequency wave number recovery from time-harmonic propagating shear waves, *Medical image analysis* 30 (2016) 1-10.
- [53] L.J. O'Donnell, C.-F. Westin, An introduction to diffusion tensor image analysis, *Neurosurgery Clinics* 22(2) (2011) 185-196.

- [54] S. Lewis, H. Dyvorne, Y. Cui, B. Taouli, Diffusion-weighted imaging of the liver: techniques and applications, *Magn Reson Imaging Clin N Am* 22(3) (2014) 373-95.
- [55] Y. Safraou, K. Krehl, T. Meyer, S. Mehrgan, J.E.L. Jordan, H. Tzschätzsch, T. Fischer, P. Asbach, J. Braun, I. Sack, The influence of static portal pressure on liver biophysical properties, *Acta Biomaterialia* 169 (2023) 118-129.
- [56] M. Shahyari, S. Keller, D. Meierhofer, I. Wallach, Y. Safraou, J. Guo, S.R. Marticorena Garcia, J. Braun, M.R. Makowski, I. Sack, On the relationship between metabolic capacities and in vivo viscoelastic properties of the liver, *Frontiers in Bioengineering and Biotechnology* 10 (2023) 1042711.
- [57] J.E.L. Jordan, G. Bertalan, T. Meyer, H. Tzschätzsch, A. Gauert, L. Bramè, H. Herthum, Y. Safraou, L. Schröder, J. Braun, Microscopic multifrequency MR elastography for mapping viscoelasticity in zebrafish, *Magnetic Resonance in Medicine* 87(3) (2022) 1435-1445.
- [58] S. Goshima, M. Kanematsu, H. Kondo, R. Yokoyama, K. Kajita, Y. Tsuge, H. Watanabe, Y. Shiratori, M. Onozuka, N. Moriyama, Diffusion-weighted imaging of the liver: optimizing b value for the detection and characterization of benign and malignant hepatic lesions, *J Magn Reson Imaging* 28(3) (2008) 691-7.
- [59] H. Tzschätzsch, J. Guo, F. Dittmann, S. Hirsch, E. Barnhill, K. Jöhrens, J. Braun, I. Sack, Tomoelastography by multifrequency wave number recovery from time-harmonic propagating shear waves, *Med Image Anal* 30 (2016) 1-10.
- [60] S. Papazoglou, S. Hirsch, J. Braun, I. Sack, Multifrequency inversion in magnetic resonance elastography, *Physics in Medicine & Biology* 57(8) (2012) 2329.
- [61] J.L. Shivers, J. Feng, A.S.G. van Oosten, H. Levine, P.A. Janmey, F.C. MacKintosh, Compression stiffening of fibrous networks with stiff inclusions, *Proc Natl Acad Sci U S A* 117(35) (2020) 21037-21044.
- [62] A.S. van Oosten, M. Vahabi, A.J. Licup, A. Sharma, P.A. Galie, F.C. MacKintosh, P.A. Janmey, Uncoupling shear and uniaxial elastic moduli of semiflexible biopolymer networks: compression-softening and stretch-stiffening, *Sci Rep* 6 (2016) 19270.
- [63] R. Cheng, F. Zhang, M. Li, X. Wo, Y.W. Su, W. Wang, Influence of Fixation and Permeabilization on the Mass Density of Single Cells: A Surface Plasmon Resonance Imaging Study, *Front Chem* 7 (2019) 588.
- [64] R. Thavarajah, V.K. Mudimbaimannar, J. Elizabeth, U.K. Rao, K. Ranganathan, Chemical and physical basics of routine formaldehyde fixation, *J Oral Maxillofac Pathol* 16(3) (2012) 400-5.
- [65] F.-R.E. Curry, R.H. Adamson, Vascular permeability modulation at the cell, microvessel, or whole organ level: towards closing gaps in our knowledge, *Cardiovascular Research* 87(2) (2010) 218-229.
- [66] N. Berndt, H.-G. Holzhütter, Dynamic metabolic zonation of the hepatic glucose metabolism is accomplished by sinusoidal plasma gradients of nutrients and hormones, *Frontiers in physiology* 9 (2018) 419724.
- [67] J. Gao, X.J. Qin, H. Jiang, J.F. Chen, T. Wang, T. Zhang, S.Z. Xu, J.M. Song, Detecting serum and urine metabolic profile changes of CCl₄-liver fibrosis in rats at 12 weeks based on gas chromatography-mass spectrometry, *Exp Ther Med* 14(2) (2017) 1496-1504.
- [68] M.-L. Chang, S.-S. Yang, Metabolic signature of hepatic fibrosis: from individual pathways to systems biology, *Cells* 8(11) (2019) 1423.
- [69] W.-I. Ai, L.-y. Dong, J. Wang, Z.-w. Li, X. Wang, J. Gao, Y. Wu, W. An, Deficiency in augmenter of liver regeneration accelerates liver fibrosis by promoting migration of hepatic stellate cell, *Biochimica et Biophysica Acta (BBA)-Molecular Basis of Disease* 1864(11) (2018) 3780-3791.

- [70] C. Bastard, M.R. Bosisio, M. Chabert, A.D. Kalopissis, M. Mahrouf-Yorgov, H. Gilgenkrantz, S. Mueller, L. Sandrin, Transient micro-elastography: A novel non-invasive approach to measure liver stiffness in mice, *World J Gastroenterol* 17(8) (2011) 968-75.
- [71] M.H. Wang, M.L. Palmeri, C.D. Guy, L. Yang, L.W. Hedlund, A.M. Diehl, K.R. Nightingale, In vivo quantification of liver stiffness in a rat model of hepatic fibrosis with acoustic radiation force, *Ultrasound in medicine & biology* 35(10) (2009) 1709-1721.
- [72] M. Agarwal, M. Goheen, S. Jia, S. Ling, E.S. White, K.K. Kim, Type I collagen signaling regulates opposing fibrotic pathways through $\alpha 2\beta 1$ integrin, *American Journal of Respiratory Cell and Molecular Biology* 63(5) (2020) 613-622.
- [73] S. Hui, A.J. Cowan, X. Zeng, L. Yang, T. TeSlaa, X. Li, C. Bartman, Z. Zhang, C. Jang, L. Wang, Quantitative fluxomics of circulating metabolites, *Cell metabolism* 32(4) (2020) 676-688. e4.
- [74] M. Rahim, C.M. Hasenour, T.K. Bednarski, C.C. Hughey, D.H. Wasserman, J.D. Young, Multitissue $2\text{H}/13\text{C}$ flux analysis reveals reciprocal upregulation of renal gluconeogenesis in hepatic PEPCK-C-knockout mice, *JCI insight* 6(12) (2021).
- [75] C.M. Hasenour, M.L. Wall, D.E. Ridley, C.C. Hughey, F.D. James, D.H. Wasserman, J.D. Young, Mass spectrometry-based microassay of 2H and 13C plasma glucose labeling to quantify liver metabolic fluxes in vivo, *American Journal of Physiology-Endocrinology and Metabolism* 309(2) (2015) E191-E203.
- [76] N. Berndt, J. Eckstein, N. Heucke, T. Wuensch, R. Gajowski, M. Stockmann, D. Meierhofer, H.G. Holzhütter, Metabolic heterogeneity of human hepatocellular carcinoma: implications for personalized pharmacological treatment, *The FEBS Journal* 288(7) (2021) 2332-2346.
- [77] N. Berndt, C.A. Hudert, J. Eckstein, C. Loddenkemper, S. Henning, P. Bufler, D. Meierhofer, I. Sack, S. Wiegand, I. Wallach, Alterations of central liver metabolism of pediatric patients with non-alcoholic fatty liver disease, *International Journal of Molecular Sciences* 23(19) (2022) 11072.
- [78] A.S. Morr, H. Herthum, F. Schrank, S. Görner, M.S. Anders, M. Lerchbaumer, H.-P. Müller, T. Fischer, K.-V. Jenderka, H.H. Hansen, Liquid-liver phantom: mimicking the viscoelastic dispersion of human liver for ultrasound-and MRI-based elastography, *Investigative Radiology* 57(8) (2022) 502-509.
- [79] R.G. Barr, S.R. Wilson, D. Rubens, G. Garcia-Tsao, G. Ferraioli, Update to the society of radiologists in ultrasound liver elastography consensus statement, *Radiology* 296(2) (2020) 263-274.
- [80] S.M. Seyedpour, M. Nabati, L. Lambers, S. Nafisi, H.M. Tautenhahn, I. Sack, J.R. Reichenbach, T. Ricken, Application of Magnetic Resonance Imaging in Liver Biomechanics: A Systematic Review, *Front Physiol* 12 (2021) 733393.
- [81] H. Tzschätzsch, S. Ipek-Ugay, J. Guo, K.J. Streitberger, E. Gentz, T. Fischer, R. Klaua, M. Schultz, J. Braun, I. Sack, In vivo time-harmonic multifrequency elastography of the human liver, *Phys Med Biol* 59(7) (2014) 1641-54.
- [82] F. Bazerbachi, S. Haffar, Z. Wang, J. Cabezas, M.T. Arias-Loste, J. Crespo, S. Darwish-Murad, M.A. Ikram, J.K. Olynyk, E. Gan, Range of normal liver stiffness and factors associated with increased stiffness measurements in apparently healthy individuals, *Clinical Gastroenterology and Hepatology* 17(1) (2019) 54-64. e1.
- [83] S. Abuhattum, P. Kotzbeck, R. Schlußler, A. Harger, A. Ariza de Schellenberger, K. Kim, J.-C. Escolano, T. Müller, J. Braun, M. Wabitsch, Adipose cells and tissues soften with lipid accumulation while in diabetes adipose tissue stiffens, *Scientific Reports* 12(1) (2022) 10325.

- [84] L. Hodson, P.J. Gunn, The regulation of hepatic fatty acid synthesis and partitioning: the effect of nutritional state, *Nature Reviews Endocrinology* 15(12) (2019) 689-700.
- [85] F.A. Chaudhry, R.J. Reimer, R.H. Edwards, The glutamine commute: take the N line and transfer to the A, *J Cell Biol* 157(3) (2002) 349-55.
- [86] N. Salameh, B. Larrat, J. Abarca-Quinones, S. Pallu, M. Dorvillius, I. Leclercq, M. Fink, R. Sinkus, B.E. Van Beers, Early detection of steatohepatitis in fatty rat liver by using MR elastography, *Radiology* 253(1) (2009) 90-7.
- [87] Q. Luo, D. Kuang, B. Zhang, G. Song, Cell stiffness determined by atomic force microscopy and its correlation with cell motility, *Biochimica et Biophysica Acta (BBA)-General Subjects* 1860(9) (2016) 1953-1960.
- [88] Y. Qiu, C.C. Chien, B. Maroulis, J. Bei, A. Gaitas, B. Gong, Extending applications of AFM to fluidic AFM in single living cell studies, *Journal of cellular physiology* 237(8) (2022) 3222-3238.
- [89] A. Gauert, N. Oik, H. Pimentel-Gutiérrez, K. Astrahantseff, L.D. Jensen, Y. Cao, A. Eggert, C. Eckert, A.I.H. Hagemann, Fast, In Vivo Model for Drug-Response Prediction in Patients with B-Cell Precursor Acute Lymphoblastic Leukemia, *Cancers (Basel)* 12(7) (2020).
- [90] M.B. Orger, The cellular organization of zebrafish visuomotor circuits, *Current Biology* 26(9) (2016) R377-R385.
- [91] L.A. Heap, G.C. Vanwalleghem, A.W. Thompson, I. Favre-Bulle, H. Rubinsztein-Dunlop, E.K. Scott, Hypothalamic projections to the optic tectum in larval zebrafish, *Frontiers in neuroanatomy* 11 (2018) 135.
- [92] F. Sauer, S. Grosser, M. Shahryari, A. Hayn, J. Guo, J. Braun, S. Briest, B. Wolf, B. Aktas, L.C. Horn, Changes in tissue fluidity predict tumor aggressiveness in vivo, *Advanced Science* 10(26) (2023) 2303523.
- [93] S. Vanderbeck, J. Bockhorst, D. Kleiner, R. Komorowski, N. Chalasani, S. Gawrieh, Automatic quantification of lobular inflammation and hepatocyte ballooning in nonalcoholic fatty liver disease liver biopsies, *Hum Pathol* 46(5) (2015) 767-75.
- [94] Z.M. Younossi, R. Loomba, Q.M. Anstee, M.E. Rinella, E. Bugianesi, G. Marchesini, B.A. Neuschwander-Tetri, L. Serfaty, F. Negro, S.H. Caldwell, V. Ratziu, K.E. Corey, S.L. Friedman, M.F. Abdelmalek, S.A. Harrison, A.J. Sanyal, J.E. Lavine, P. Mathurin, M.R. Charlton, Z.D. Goodman, N.P. Chalasani, K.V. Kowdley, J. George, K. Lindor, Diagnostic modalities for nonalcoholic fatty liver disease, nonalcoholic steatohepatitis, and associated fibrosis, *Hepatology* 68(1) (2018) 349-360.
- [95] E. Altinmakas, O. Bane, S.J. Hectors, R. Issa, G. Carbonell, G. Abboud, T.D. Schiano, S. Thung, A. Fischman, M.D. Kelly, S.L. Friedman, P. Kennedy, B. Taouli, Performance of native and gadoxetate-enhanced liver and spleen T(1) mapping for noninvasive diagnosis of clinically significant portal hypertension: preliminary results, *Abdom Radiol (NY)* 47(11) (2022) 3758-3769.
- [96] N. Palaniyappan, E. Cox, C. Bradley, R. Scott, A. Austin, R. O'Neill, G. Ramjas, S. Travis, H. White, R. Singh, P. Thurley, I.N. Guha, S. Francis, G.P. Aithal, Non-invasive assessment of portal hypertension using quantitative magnetic resonance imaging, *J Hepatol* 65(6) (2016) 1131-1139.
- [97] K. Uehara, J. Sostre-Colón, M. Gavin, D. Santoleri, K.-A. Leonard, R.L. Jacobs, P.M. Titchenell, Activation of liver mTORC1 protects against NASH via dual regulation of VLDL-TAG secretion and de novo lipogenesis, *Cellular and Molecular Gastroenterology and Hepatology* 13(6) (2022) 1625-1647.

- [98] E.E. Patton, L.I. Zon, D.M. Langenau, Zebrafish disease models in drug discovery: from preclinical modelling to clinical trials, *Nature Reviews Drug Discovery* 20(8) (2021) 611-628.
- [99] M. Ortega-Ribera, A. Gibert-Ramos, L. Abad-Jordà, M. Magaz, L. Téllez, L. Paule, E. Castillo, R. Pastó, B. de Souza Basso, P. Olivas, L. Orts, J.J. Lozano, R. Villa, J. Bosch, A. Albillos, J.C. García-Pagán, J. Gracia-Sancho, Increased sinusoidal pressure impairs liver endothelial mechanosensing, uncovering novel biomarkers of portal hypertension, *JHEP Rep* 5(6) (2023) 100722.
- [100] J. Jordan, N. Jaitner, T. Meyer, L. Brahmè, M. Ghayeb, J. Köppke, S.K. Chandia, V. Zaburdaev, L. Chai, H. Tzschätzsch, Optical time-harmonic elastography for multiscale stiffness mapping across the phylogenetic tree, *arXiv preprint arXiv:2312.07380* (2023).

Statutory declaration

Quantification of the biophysical properties of the liver in correlation with microstructural and vascular changes using multimodal imaging

Quantifizierung der biophysikalischen Eigenschaften der Leber in Korrelation mit mikrostrukturellen und vaskulären Veränderungen unter Verwendung multimodaler Bildgebungstechniken.

“I, Yasmine Safraou, by personally signing this document in lieu of an oath, hereby affirm that I prepared the submitted dissertation on the topic [title of your dissertation in English and German], independently and without the support of third parties, and that I used no other sources and aids than those stated.

All parts which are based on the publications or presentations of other authors, either in letter or in spirit, are specified as such in accordance with the citing guidelines. The sections on methodology (in particular regarding practical work, laboratory regulations, statistical processing) and results (in particular regarding figures, charts and tables) are exclusively my responsibility.

Furthermore, I declare that I have correctly marked all of the data, the analyses, and the conclusions generated from data obtained in collaboration with other persons, and that I have correctly marked my own contribution and the contributions of other persons (cf. declaration of contribution). I have correctly marked all texts or parts of texts that were generated in collaboration with other persons.

My contributions to any publications to this dissertation correspond to those stated in the below joint declaration made together with the supervisor. All publications created within the scope of the dissertation comply with the guidelines of the ICMJE (International Committee of Medical Journal Editors; <http://www.icmje.org>) on authorship. In addition, I declare that I shall comply with the regulations of Charité – Universitätsmedizin Berlin on ensuring good scientific practice.

I declare that I have not yet submitted this dissertation in identical or similar form to another Faculty.

The significance of this statutory declaration and the consequences of a false statutory declaration under criminal law (Sections 156, 161 of the German Criminal Code) are known to me.”

Date

Signature

Declaration of my contribution to the publications

I, Yasmine Safraou, contributed the following to the below listed publications:

Publication 1: Y. Safraou, K. Krehl, T. Meyer, S. Mehrgan, J.E.L. Jordan, H. Tzschätzsch, T. Fischer, P. Asbach, J. Braun, I. Sack, J. Guo, The influence of static portal pressure on liver biophysical properties, *Acta Biomaterialia* 169 (2023) 118-129.

<https://doi.org/10.1016/j.actbio.2023.07.033>

Contributions:

Under the supervision of Prof. Dr.rer.nat Guo and Prof. Dr.rer.nat Sack, I contributed significantly to all aspects of this project with the primary objective of achieving a first author publication. Together, we carefully designed different scenarios to investigate the effects of static portal pressure on ex vivo rat livers under different experimental conditions.

Firstly, I worked with Dr. Krehl and Prof. Guo on establishing a protocol for the in-situ preparation of rat livers. This involved rigorous testing and validation of protocols dedicated to post-mortem organ decoagulation, in-situ perfusion and organ static cold storage preservation prior to imaging. I have explored and standardized various ex vivo organ embedding methods to optimize the effectiveness of liver confinement during liver perfusion with increasing portal pressures. Prof. Guo and I investigated different MRI and MRE parameters to relevantly evaluate the biophysical properties of the ex vivo perfused livers for all experimental scenarios.

For vessel segmentation in T2w images, I developed a dedicated algorithm together with Prof. Tzschätzsch. Furthermore, in collaboration with my colleague Tom Meyer and Prof. Tzschätzsch, we adapted the post-processing pipeline for MRE data analysis specifically for these datasets. Finally, I was responsible for conducting the statistical analysis of the data and the preparation of all relevant figures for the manuscript.

Publication 2: M. Shahryari, S. Keller, D. Meierhofer, I. Wallach, **Y. Safrdou**, J. Guo, S.R. Marticorena Garcia, J. Braun, M.R. Makowski, I. Sack, N. Berndt, On the relationship between metabolic capacities and in vivo viscoelastic properties of the liver, *Frontiers in Bioengineering and Biotechnology* 10 (2023) 1042711.

<https://doi.org/10.3389/fbioe.2022.1042711>

Contributions:

Drawing from my previous experience in conducting preclinical in vivo liver imaging, and performing ex vivo multifrequency MRE on rabbit liver tissue samples using a tabletop scanner, I contributed significantly in advancing this research project. Together with the first author Dr. Shahryari, we designed a protocol to anesthetize and control the health state of the rabbits during the acquisition of imaging data. I have assisted my colleague in acquiring elastography data, including the selection of the vibration frequencies suitable to vibrate the rabbit abdomen. Furthermore, I helped with sacrificing the rabbits after completing the imaging protocol, and prepared liver samples destined for proteomics analyses. Later, I contributed to the analysis of the proteomics results to identify potential correlations between metabolic functions of the liver and imaging-based biophysical parameters. This analysis was essential for a comprehensive interpretation of the study's main findings. Finally, I have also contributed to the redaction of the paper.

Publication 3: J.E.L. Jordan, G. Bertalan, T. Meyer, H. Tzschätzsch, A. Gauert, L. Bramè, H. Herthum, **Y. Safraou**, L. Schröder, J. Braun, Microscopic multifrequency MR elastography for mapping viscoelasticity in zebrafish, *Magnetic Resonance in Medicine* 87(3) (2022) 1435-1445.

<https://doi.org/10.1002/mrm.29066>

Contributions:

In this study, my collaboration was focused on designing experiments to obtain groundtruth data. Within this context, I conducted tabletop MRE measurements on different embedding gels and analyzed the ensuing results. Consequently, I proceeded to post-process the data and generated the unfiltered wave images and maps shown on Figure 2 in the 'Phantom experiments' subsection of the manuscript. The ground truth measurements played a key role in validating the accuracy of the 7T MRE measurements. They allowed to verify the post-processing pipeline performance in accurately quantifying shear wave speed (SWS) and phase angle (φ) across varying resolutions and frequencies. Additionally, I provided specific guidance on how to handle ex vivo zebrafish during experiments, including their sacrifice and embedding. My contribution helped maintaining the integrity and reliability of the experimental protocols and results. Finally, I have contributed to writing this manuscript.

Publications

Publication 1: Y. Safraou, K. Krehl, T. Meyer, S. Mehrgan, J.E.L. Jordan, H. Tzschätzsch, T. Fischer, P. Asbach, J. Braun, I. Sack, J. Guo, The influence of static portal pressure on liver biophysical properties, *Acta Biomaterialia* 169 (2023) 118-129.
<https://doi.org/10.1016/j.actbio.2023.07.033>

Selected Categories: **“ENGINEERING, BIOMEDICAL”** Selected Category
 Scheme: WoS
Gesamtanzahl: 97 Journale

Rank	Full Journal Title	Total Cites	Journal Impact Factor	Eigenfaktor
1	Nature Biomedical Engineering	13,517	28.1	0.03531
2	Bioactive Materials	15,010	18.9	0.01305
3	IEEE Reviews in Biomedical Engineering	2,473	17.6	0.00244
4	BIOMATERIALS	119,835	14.0	0.05728
5	Biomaterials Research	2,418	11.3	0.00216
6	MEDICAL IMAGE ANALYSIS	19,500	10.9	0.02646
7	IEEE TRANSACTIONS ON MEDICAL IMAGING	34,640	10.6	0.03384
8	Advanced Healthcare Materials	27,799	10.0	0.03105
9	Acta Biomaterialia	59,339	9.7	0.04106
10	Annual Review of Biomedical Engineering	5,819	9.7	0.00387
11	Biofabrication	8,095	9.0	0.00659
12	International Journal of Bioprinting	1,324	8.4	0.00121
13	Materials Today Bio	2,072	8.2	0.00185
14	Bio-Design and Manufacturing	1,163	7.9	0.00136
15	Photoacoustics	2,551	7.9	0.00361
16	COMPUTERS IN BIOLOGY AND MEDICINE	21,417	7.7	0.02108
17	Artificial Intelligence in Medicine	6,556	7.5	0.00647
18	Bioengineering & Translational Medicine	2,144	7.4	0.00237
19	npj Regenerative Medicine	1,765	7.2	0.00340
20	Biocybernetics and Biomedical Engineering	3,069	6.4	0.00296

Publication 1: Y. Safraou, K. Krehl, T. Meyer, S. Mehrgan, J.E.L. Jordan, H. Tzschätzsch, T. Fischer, P. Asbach, J. Braun, I. Sack, J. Guo, The influence of static portal pressure on liver biophysical properties, *Acta Biomaterialia* 169 (2023) 118-129. <https://doi.org/10.1016/j.actbio.2023.07.033>

Publication 1: Y. Safraou, K. Krehl, T. Meyer, S. Mehrgan, J.E.L. Jordan, H. Tzschätzsch, T. Fischer, P. Asbach, J. Braun, I. Sack, J. Guo, The influence of static portal pressure on liver biophysical properties, *Acta Biomaterialia* 169 (2023) 118-129. <https://doi.org/10.1016/j.actbio.2023.07.033>

Publication 1: Y. Safraou, K. Krehl, T. Meyer, S. Mehrgan, J.E.L. Jordan, H. Tzschätzsch, T. Fischer, P. Asbach, J. Braun, I. Sack, J. Guo, The influence of static portal pressure on liver biophysical properties, *Acta Biomaterialia* 169 (2023) 118-129. <https://doi.org/10.1016/j.actbio.2023.07.033>

Publication 1: Y. Safraou, K. Krehl, T. Meyer, S. Mehrgan, J.E.L. Jordan, H. Tzschätzsch, T. Fischer, P. Asbach, J. Braun, I. Sack, J. Guo, The influence of static portal pressure on liver biophysical properties, *Acta Biomaterialia* 169 (2023) 118-129. <https://doi.org/10.1016/j.actbio.2023.07.033>

Publication 1: Y. Safraou, K. Krehl, T. Meyer, S. Mehrgan, J.E.L. Jordan, H. Tzschätzsch, T. Fischer, P. Asbach, J. Braun, I. Sack, J. Guo, The influence of static portal pressure on liver biophysical properties, *Acta Biomaterialia* 169 (2023) 118-129. <https://doi.org/10.1016/j.actbio.2023.07.033>

Publication 1: Y. Safraou, K. Krehl, T. Meyer, S. Mehrgan, J.E.L. Jordan, H. Tzschätzsch, T. Fischer, P. Asbach, J. Braun, I. Sack, J. Guo, The influence of static portal pressure on liver biophysical properties, *Acta Biomaterialia* 169 (2023) 118-129. <https://doi.org/10.1016/j.actbio.2023.07.033>

Publication 1: Y. Safraou, K. Krehl, T. Meyer, S. Mehrgan, J.E.L. Jordan, H. Tzschätzsch, T. Fischer, P. Asbach, J. Braun, I. Sack, J. Guo, The influence of static portal pressure on liver biophysical properties, *Acta Biomaterialia* 169 (2023) 118-129. <https://doi.org/10.1016/j.actbio.2023.07.033>

Publication 1: Y. Safraou, K. Krehl, T. Meyer, S. Mehrgan, J.E.L. Jordan, H. Tzschätzsch, T. Fischer, P. Asbach, J. Braun, I. Sack, J. Guo, The influence of static portal pressure on liver biophysical properties, *Acta Biomaterialia* 169 (2023) 118-129. <https://doi.org/10.1016/j.actbio.2023.07.033>

Publication 1: Y. Safraou, K. Krehl, T. Meyer, S. Mehrgan, J.E.L. Jordan, H. Tzschätzsch, T. Fischer, P. Asbach, J. Braun, I. Sack, J. Guo, The influence of static portal pressure on liver biophysical properties, *Acta Biomaterialia* 169 (2023) 118-129. <https://doi.org/10.1016/j.actbio.2023.07.033>

Publication 1: Y. Safraou, K. Krehl, T. Meyer, S. Mehrgan, J.E.L. Jordan, H. Tzschätzsch, T. Fischer, P. Asbach, J. Braun, I. Sack, J. Guo, The influence of static portal pressure on liver biophysical properties, *Acta Biomaterialia* 169 (2023) 118-129. <https://doi.org/10.1016/j.actbio.2023.07.033>

Publication 1: Y. Safraou, K. Krehl, T. Meyer, S. Mehrgan, J.E.L. Jordan, H. Tzschätzsch, T. Fischer, P. Asbach, J. Braun, I. Sack, J. Guo, The influence of static portal pressure on liver biophysical properties, *Acta Biomaterialia* 169 (2023) 118-129. <https://doi.org/10.1016/j.actbio.2023.07.033>

Publication 1: Y. Safraou, K. Krehl, T. Meyer, S. Mehrgan, J.E.L. Jordan, H. Tzschätzsch, T. Fischer, P. Asbach, J. Braun, I. Sack, J. Guo, The influence of static portal pressure on liver biophysical properties, *Acta Biomaterialia* 169 (2023) 118-129. <https://doi.org/10.1016/j.actbio.2023.07.033>

Publication 1: Y. Safraou, K. Krehl, T. Meyer, S. Mehrgan, J.E.L. Jordan, H. Tzschätzsch, T. Fischer, P. Asbach, J. Braun, I. Sack, J. Guo, The influence of static portal pressure on liver biophysical properties, *Acta Biomaterialia* 169 (2023) 118-129. <https://doi.org/10.1016/j.actbio.2023.07.033>

Publication 2: M. Shahryari, S. Keller, D. Meierhofer, I. Wallach, Y. Safraou, J. Guo, S.R. Marticorena Garcia, J. Braun, M.R. Makowski, I. Sack, N. Berndt, On the relationship between metabolic capacities and in vivo viscoelastic properties of the liver, *Frontiers in Bioengineering and Biotechnology* 10 (2023) 1042711.

<https://doi.org/10.3389/fbioe.2022.1042711>

Selected Categories: **“MULTIDISCIPLINARY SCIENCES”** Selected Category
Scheme: WoS

Gesamtanzahl: 73 Journale

Rank	Full Journal Title	Total Cites	Journal Impact Factor	Eigenfaktor
1	NATURE	964,876	64.8	1.10309
2	SCIENCE	818,308	56.9	0.80079
3	Nature Human Behaviour	14,216	29.9	0.05276
4	National Science Review	13,369	20.6	0.02511
5	Science Bulletin	15,992	18.9	0.02733
6	Nature Communications	675,323	16.6	1.40879
7	Science Advances	126,246	13.6	0.33133
8	PROCEEDINGS OF THE NATIONAL ACADEMY OF SCIENCES OF THE UNITED STATES OF AMERICA	788,686	11.1	0.67974
9	Research	4,694	11.0	0.00775
10	Journal of Advanced Research	9,575	10.7	0.00813
11	Research Synthesis Methods	6,362	9.8	0.01080
12	Scientific Data	22,811	9.8	0.04464
13	GigaScience	9,104	9.2	0.02101
14	Machine Learning-Science and Technology	1,538	6.8	0.00386
15	iScience	21,604	5.8	0.04795
16	Frontiers in Bioengineering and Biotechnology	25,676	5.7	0.03082
17	ANNALS OF THE NEW YORK ACADEMY OF SCIENCES	47,360	5.2	0.01806
18	NPJ Microgravity	1,055	5.1	0.00158



OPEN ACCESS

EDITED BY
Salavat Aglyamov,
University of Houston, United States

REVIEWED BY
Meng Yin,
Mayo Clinic, United States
Mohsin Rahim,
Vanderbilt University, United States

*CORRESPONDENCE
Nikolaus Berndt,
✉ Nikolaus.berndt@charite.de

SPECIALTY SECTION
This article was submitted to
Biomechanics,
a section of the journal
Frontiers in Bioengineering and
Biotechnology

RECEIVED 12 September 2022
ACCEPTED 21 December 2022
PUBLISHED 09 January 2023

CITATION
Shahryari M, Keller S, Meierhofer D,
Wallach I, Safraou Y, Guo J,
Marticorena Garcia SR, Braun J,
Makowski MR, Sack J and Berndt N (2023),
On the relationship between metabolic
capacities and *in vivo* viscoelastic
properties of the liver.
Front. Bioeng. Biotechnol. 10:1042711.
doi: 10.3389/fbioe.2022.1042711

COPYRIGHT
© 2023 Shahryari, Keller, Meierhofer,
Wallach, Safraou, Guo, Marticorena Garcia,
Braun, Makowski, Sack and Berndt. This is
an open-access article distributed under
the terms of the Creative Commons
Attribution License (CC BY). The use,
distribution or reproduction in other
forums is permitted, provided the original
author(s) and the copyright owner(s) are
credited and that the original publication in
this journal is cited, in accordance with
accepted academic practice. No use,
distribution or reproduction is permitted
which does not comply with these terms.

On the relationship between metabolic capacities and *in vivo* viscoelastic properties of the liver

Mehrgan Shahryari¹, Sarah Keller¹, David Meierhofer²,
Iwona Wallach³, Yasmine Safraou¹, Jing Guo¹,
Stephan R. Marticorena Garcia¹, Jürgen Braun⁴,
Marcus R. Makowski⁵, Ingolf Sack¹ and Nikolaus Berndt^{3*}

¹Department of Radiology, Charité—Universitätsmedizin Berlin, Corporate Member of Freie Universität Berlin and Humboldt-Universität zu Berlin, Berlin, Germany, ²Mass Spectrometry Facility, Max Planck Institute for Molecular Genetics, Berlin, Germany, ³Institute of Computer-Assisted Cardiovascular Medicine, Charité—Universitätsmedizin Berlin, Corporate Member of Freie Universität Berlin and Humboldt-Universität zu Berlin, Berlin, Germany, ⁴Institute of Medical Informatics, Charité—Universitätsmedizin Berlin, Corporate Member of Freie Universität Berlin and Humboldt-Universität zu Berlin, Berlin, Germany, ⁵Department of Diagnostic and Interventional Radiology, Technical University of Munich, Faculty of Medicine, Munich, Germany

The liver is the central metabolic organ. It constantly adapts its metabolic capacity to current physiological requirements. However, the relationship between tissue structure and hepatic function is incompletely understood; this results in a lack of diagnostic markers in medical imaging that can provide information about the liver's metabolic capacity. Therefore, using normal rabbit livers, we combined magnetic resonance elastography (MRE) with proteomics-based kinetic modeling of central liver metabolism to investigate the potential role of MRE for predicting the liver's metabolic function *in vivo*. Nineteen New Zealand white rabbits were investigated by multifrequency MRE and positron emission tomography (PET). This yielded maps of shear wave speed (SWS), penetration rate (PR) and standardized uptake value (SUV). Proteomic analysis was performed after the scans. Hepatic metabolic functions were assessed on the basis of the HEPATOKIN1 model in combination with a model of hepatic lipid-droplet metabolism using liquid chromatography–mass spectrometry. Our results showed marked differences between individual livers in both metabolic functions and stiffness properties, though not in SUV. When livers were divided into 'stiff' and 'soft' subgroups (cutoff SWS = 1.6 m/s), stiff livers showed a lower capacity for triacylglycerol storage, while at the same time showing an increased capacity for gluconeogenesis and cholesterol synthesis. Furthermore, SWS was correlated with gluconeogenesis and PR with urea production and glutamine exchange. In conclusion, our study indicates a close relationship between the viscoelastic properties of the liver and metabolic function. This could be used in future studies to predict non-invasively the functional reserve capacity of the liver in patients.

KEYWORDS

viscoelasticity, MRE, PET, stiffness, liver metabolism, proteomics, reserve capacity, hepatic function model

1 Introduction

The liver is the key metabolic organ of the human body. It has a wide range of metabolic functions including homeostatic regulation of numerous plasma metabolites (glucose, amino acids and lipoproteins), detoxification of endogenously formed metabolic end products (e.g., ammonia, urea), and storage of nutrients in the form of glycogen or triacylglycerol. It continuously adapts its metabolic capacities to the current physiological status of the individual. For example, after a carbohydrate-rich meal, the liver takes up a substantial amount of glucose from the plasma; this is then transiently converted into glycogen and triacylglycerol. Conversely, under fasting conditions the liver produces glucose by phosphorylation of glycogen and synthesis *de novo* from amino acids, lactate and glycerol to prevent a potentially life-threatening drop in plasma glucose below 55 mg/dl (Mathew et al., 2022). Metabolic alterations become permanent as a result of long-term life habits such as overnutrition, as in metabolic syndrome (MetS). MetS—with its hallmarks of obesity, insulin resistance and dyslipidaemia (Bussler et al., 2017)—is an epidemic disease that is often triggered by childhood overnutrition. Non-alcoholic fatty liver disease (NAFLD) is recognized as the hepatic manifestation of MetS (Lonardo et al., 2015) and can progress silently into liver fibrosis and cirrhosis without apparent clinical symptoms (Sivell, 2019). Today, non-alcoholic steatohepatitis is the most common etiology among waiting-list candidates for liver transplantation (Wong and Singal, 2020). Nevertheless, early diagnosis and differentiation of liver diseases remains a major challenge. While cirrhosis and liver tumors represent the end-stage of liver pathology, with life-threatening complications and clear clinical manifestation, most patients with NAFLD have a stable and relatively benign fatty liver for a long time (Caldwell and Argo, 2010).

Evaluation of liver function is a diagnostic challenge because there are only few techniques that can directly quantify metabolic functions *in vivo*. Quantitative liver function test, which use specific metabolites, such as indocyanine green clearance test or methacetin breath-test are complex and costly, and they entail considerable discomfort for the subject (Lalazar et al., 2008; Seyama and Kokudo, 2009). Furthermore, they assess only very specific pathways under very restricted conditions and cannot be used for a general evaluation of metabolic capacities (Vos et al., 2014; De Gasperi et al., 2016; Gorowska-Kowolik et al., 2017). New computational methods such as proteomics-based evaluation of metabolic liver function by large-scale kinetic modelling allows the assessment of metabolic capacities under a wide range of physiological and pathological conditions (Berndt et al., 2018a; Berndt et al., 2019; Berndt et al., 2020; Kespohl et al., 2020; Berndt et al., 2021a; Berndt et al., 2021b). However, these require biopsies, which are limited in follow-up examinations owing to pain, risk of bleeding and sampling errors (Ratziu et al., 2005; Boyd et al., 2020). Despite advances in quantitative medical imaging, there is still no reliable non-invasive imaging marker that can detect metabolic changes occurring in seemingly healthy livers during the 'silent progression' phase of NAFLD (Chalasanani et al., 2018). Positron emission tomography (PET) is a versatile technique for the assessment of glucose metabolism in lesions or neurodegenerative diseases, where it can be used to investigate changes in various neurotransmitter systems, neuroinflammation, and protein aggregates that characterize the disease. However, PET scans are expensive, they result in exposure of the patient to ionizing

radiation and they address only specific metabolic pathways that are not necessarily fully suited for assessment of the liver's metabolic capacity. Ultrasound-based elastography and magnetic resonance elastography (MRE) have become successful in addressing structural changes such as like degree of fibrosis and steatosis, and they therefore have the potential to replace biopsy-based histological evaluation of structural alteration (Singh et al., 2015; Castera et al., 2019; Hudert et al., 2021; Qu et al., 2021; Selvaraj et al., 2021). Liver fibrosis increases liver stiffness through accumulation and cross-linking of matrix proteins (Huwart et al., 2008; Singh et al., 2015; Reiter et al., 2020). However, beyond fibrosis, the liver's biomechanical properties are also affected by non-fibrotic alterations such as prandial states (Yin et al., 2011; Jajamovich et al., 2014; Petzold et al., 2019; Obrzut et al., 2021), hydration (Ipek-Ugay et al., 2016; Dittmann et al., 2017), blood perfusion (Ipek-Ugay et al., 2016; Meyer et al., 2022a), cell hypertrophy (Garczyńska et al., 2020), fat accumulation (Hudert et al., 2019) or inflammation (Qu et al., 2021; Selvaraj et al., 2021), making elastography unspecifically sensitive to a variety of pathophysiological processes that occur in the course of NAFLD. Only little is known about the correlation between liver biomechanical parameters and liver metabolism. In cancer patients, liver function has been correlated with stiffness measured by ultrasound-based elastography (Heucke et al., 2019) and with viscoelastic parameters measured by MRE (Lin et al., 2022). However, it remains unclear which specific metabolic function may influence viscoelastic parameters in the liver and whether apparently normal livers display a range of biomechanical properties that are correlated with the variability of metabolic functions.

Therefore, in this study we used a comprehensive kinetic model of central liver metabolism (Berndt et al., 2018a) to characterize metabolic states and capacities of healthy rabbit livers on the basis of proteomic data. We performed *in vivo* MRE in a clinical hybrid PET/MRI scanner to investigate the relationship between viscoelasticity and liver metabolism. In addition, we analyzed the *in vivo* glucose metabolism using ¹⁸F-fluorodesoxyglucose (FDG)-based PET to test the sensitivity of this imaging marker toward small variations in liver metabolism in correlation with MRE.

2 Materials and methods

2.1 Animal model

This study and all procedures involving animals were approved by the local authority (Landesamt für Gesundheit und Soziales Berlin, Reg. No. 0178/17). The experimental protocols were performed in accordance with the regulations and guidelines of the Federation of Laboratory Animal Science Association (FELASA) as well as our institutional guidelines.

Nineteen female New Zealand white rabbits (Charles River Laboratories, Sulzfeld, Germany) at the age of 11–15 weeks with a mean weight $3.22 \pm .27$ kg were used for this study. All rabbits were housed in a pathogen-free animal facility, in rooms with laminar flow, constant temperature and constant humidity. Food and water were provided *ad libitum*. However, the rabbits were fasted 2 h before the measurements and blood glucose (BG) level, as well as animal weight was measured prior to MRI scans (Table 1). Imaging was performed at the same daytime under deep-sedation of rabbits by subcutaneous injections of medetomidin hydrochlorid (Cepetor, 200 mg/kg body

TABLE 1 Descriptive data of rabbits. Parameters with group mean values given as mean \pm standard deviation for all 19 rabbits, including weight, BG, SWS, PR, SUV. BG, blood glucose; SWS, shear wave speed; PR, penetration rate; SUV, standardized uptake value.

ID	Weight in kg	BG in mg/dl	SWS in m/s	PR in m/s	SUV
3	3.6	107	1.45 \pm .11	1.04 \pm .33	2.50 \pm .21
1	2.6	178	1.65 \pm .16	1.16 \pm .26	2.26 \pm .36
15	3.5	168	1.60 \pm .15	.99 \pm .31	3.06 \pm .28
4	3.0	139	1.51 \pm .14	.96 \pm .23	2.34 \pm .37
9	3.5	154	1.70 \pm .17	1.01 \pm .35	3.00 \pm .36
16	3.3	187	1.56 \pm .13	.87 \pm .24	2.88 \pm .21
4	3.4	140	1.39 \pm .10	.84 \pm .22	2.73 \pm .18
5	3.4	158	1.41 \pm .13	.88 \pm .28	2.74 \pm .16
2	3.1	184	1.70 \pm .12	1.21 \pm .39	2.82 \pm .10
22	3.2	132	1.65 \pm .14	1.06 \pm .29	2.89 \pm .18
13	3.6	191	1.64 \pm .16	1.03 \pm .28	
7	3.2	150	1.69 \pm .12	1.03 \pm .30	
6	3.5	135	1.57 \pm .15	1.09 \pm .44	
14	2.9	159	1.56 \pm .11	1.03 \pm .38	
12	3.1	123	1.64 \pm .12	1.02 \pm .29	
8	2.9	144	1.55 \pm .16	.83 \pm .29	
18	3.2		1.68 \pm .11	.99 \pm .35	
17	3.2		1.71 \pm .16	1.00 \pm .44	
19	3.2		1.51 \pm .14	.80 \pm .18	
Mean	3.23 \pm .26	153.06 \pm 24.1	1.59 \pm .1	.99 \pm .11	2.72 \pm .27

weight) and Ketamin (Anesketin, 300 mg/kg body weight). Immediately after experimental imaging, euthanasia was performed by intravenous injection of pentobarbital sodium (Narcoren, 300 mg/kg body weight) and liver explantation was conducted. Tissues were dissected and snap frozen in liquid nitrogen for further proteomics analysis.

2.2 Imaging

2.2.1 MRI

All experiments were performed on a clinical 3-Tesla hybrid PET/MR scanner (Magnetom Biograph mMR, Siemens Healthineers, Erlangen, Germany) with a 20-channel head coil. Rabbits were positioned head first in prone position. For anatomic orientation, a transversal T1-weighted fat-saturated Dixon sequence (repetition time [TR] 4.76, echo time [TE] 1.49 ms, matrix 512 \times 512 mm, voxel size .5 \times .5 \times 2.0 mm³ and coverage of the complete liver) was performed in the abdominal region of the rabbits before MRE and PET scans.

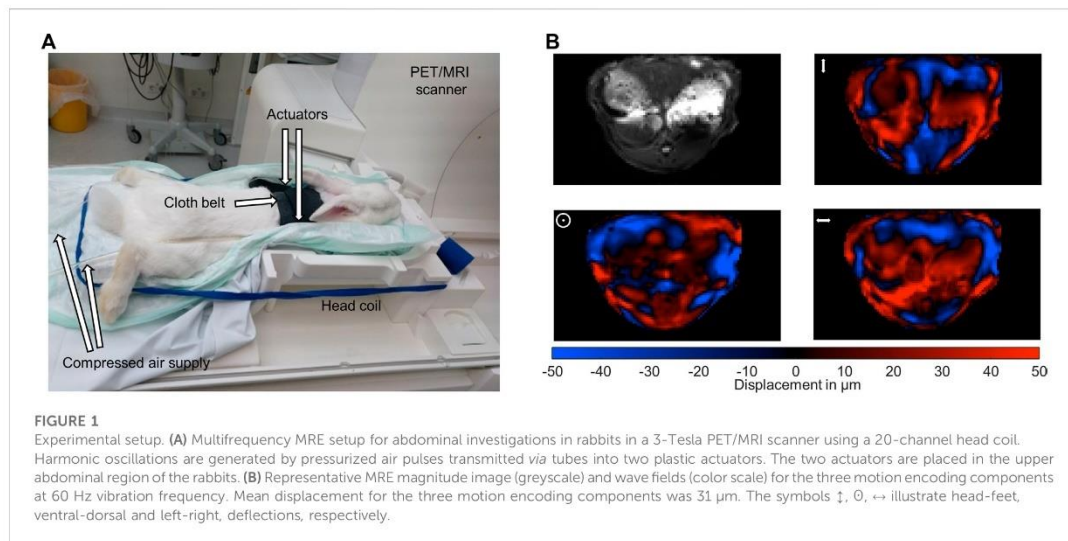
2.2.2 Multifrequency MRE

The used multifrequency MRE setup was similar to previous *in vivo* studies in patients with driver fixation adapted to rabbits (Shahryari et al., 2019; Shahryari et al., 2021). 8 phase offsets equally distributed over full vibration cycle of 40 Hz, 50 Hz, 60 Hz, 70 Hz and 80 Hz mechanical

vibrations were recorded for all three Cartesian-motion field directions in a transversal plane using a single-shot spin-echo echo-planar-imaging (EPI) sequence (Tzschätzsch et al., 2016; Dittmann et al., 2017). Oscillations were induced by two pressurized air drivers attached onto the upper abdominal region of the rabbits. The drivers were powered by air pulses of .2 bar maximum amplitude. A cloth belt around the abdomen was used to improve the contact of the drivers to the rabbits and the efficiency of shear wave excitation. Vibrations were started 2 s prior to image acquisition to ensure a steady-state flux of harmonic shear wave energy. Imaging parameters were: TE 40 ms, TR 1000 ms, matrix 104 \times 60, voxel size 1.55 \times 1.55 \times 5 mm³, 6 contiguous slices in a transversal view, 4 averages, parallel imaging with GRAPPA-factor 2, motion encoding gradient (MEG) frequency 78.61 Hz for all vibration frequencies, MEG amplitude 42 mT/m with first order moment nulling. Total MRE acquisition time was approximately 8 min. Cloth belt and actuators were removed prior to PET image acquisition. Figures 1A, B show the experimental MRE setup along with wave field components at 60 Hz vibration frequency.

2.2.3 PET

PET measurement was conducted in a subgroup of 10 rabbits injecting ¹⁸F-FDG as radiotracer intravenously (mean 75.88 \pm 14.35 MBq, min 38.59 MBq, max 91.42 MBq). The PET scan was performed, covering the entire thorax and abdomen. PET image reconstruction was conducted by ordered-subset expectation maximization (OSEM) algorithm with 3 iterations and 21 subsets, 512 \times 512 \times 127 image matrix and 1 \times 1 \times



2 mm³ voxel size. Ultrashort echo-time sequence (UTE) implemented by the vendor was used for attenuation and scatter correction (AC).

2.2.4 Image processing

MRE data were processed in MATLAB Release 2021a (The Mathworks Inc. Natick, MN, United States) using wavenumber-based inversion method (k-MDEV) (Tzschätzsch et al., 2016) publicly available at <https://bioqic-apps.charite.de> (Meyer et al., 2022b). A Butterworth low-pass filter of order 3 with a threshold of 250 m⁻¹ was used to suppress noise prior to image unwrapping (Herthum et al., 2022) while a spatial bandpass Butterworth filter of order 3 with thresholds of 15 m⁻¹ and 300 m⁻¹ was used for directional filtering (Herthum et al., 2022). Frequency-compound maps of shear wave speed (SWS in m/s) and penetration rate (PR in m/s) were computed as surrogates for tissue stiffness and inverse viscosity (Reiter et al., 2020). MRE magnitude images, SWS-, PR- and attenuation-corrected PET maps were further analyzed and used for manually drawing 3D regions of interest (ROIs) covering the liver. Mean liver SWS and PR values were calculated for each rabbit. Mean standardized uptake values (SUV) was calculated for 10 rabbits based on activity concentration (A(t)) in kBq/mL, body weight (W) in kg, injected dose (ID) in MBq, dose and decay correction factor d derived by the half-life of the radiotracer ¹⁸F-FDG and the time delay between injection and start of the measurement:

$$SUV_{\text{ROI}} = \frac{A(t) \cdot W}{ID \cdot d}$$

2.3 Shotgun proteome profiling and data analysis

2.3.1 Proteomics sample preparation with label-free quantification (LFQ)

Between 11 and 100 mg of each liver tissue were homogenized under denaturing conditions with a FastPrep (two times for 60 s, 6.5 m × s⁻¹) in 1 mL of a fresh buffer containing 3 M guanidinium chloride

(GdmCl), 10 mM Tris (2-carboxyethyl)phosphine, 20 mM chloroacetamide and 100 mM Tris-HCl pH 8.5. Lysates were boiled at 95°C for 10 min in a thermal shaker, followed by sonication for 10 min and centrifuged at 10,000 rcf for 5 min at 4°C. The supernatant was transferred into new protein low binding tubes (Eppendorf, Germany). 30 μg protein per sample were diluted to 1 M GdmCl by adding 10% acetonitrile and 25 mM Tris, 8.5 pH, followed by a Lys C digestion (Roche, Basel, Switzerland; enzyme to protein ratio 1:50, MS-grade) at 37°C for 2 h. This was followed by another dilution to .5 M GdmCl and a tryptic digestion (Roche, 1:50) at 37°C, at 800 rpm, and overnight. Subsequently, peptides were desalted with C18 columns and reconstituted in 2% formic acid in water and further separated into five fractions by strong cation exchange chromatography (SCX, 3 M Purification, Meriden, CT). Eluates were first dried in a SpeedVac, then dissolved in 5% acetonitrile and 2% formic acid in water, briefly vortexed, and sonicated in a water bath for 30 s prior to injection to nano-Liquid chromatography–mass spectrometry (LC-MS).

2.3.2 LC-MS/MS instrument settings for shotgun proteome profiling and data analysis

LC-MS/MS was carried out by nanoflow reverse-phase liquid chromatography (Dionex Ultimate 3000, Thermo Scientific) coupled online to a Q-Exactive HF Orbitrap mass spectrometer (Thermo Scientific), as reported previously (Gielisch and Meierhofer, 2015). Briefly, the LC separation was performed using a PicoFrit analytical column (75 μm ID × 50 cm long, 15 μm Tip ID; New Objectives, Woburn, MA) in-house packed with 3 μm C18 resin (Reprosil-AQ Pur, Dr. Maisch, Ammerbuch, Germany). Peptides were eluted using a gradient from 3.8% to 38% solvent B in solvent A over 120 min at a 266 nL per minute flow rate. Solvent A was .1% formic acid and solvent B was 79.9% acetonitrile, 20% H₂O, and .1% formic acid. For the IP samples, a 1-h gradient was used. Nano-electrospray was generated by applying 3.5 kV. A cycle of one full Fourier transformation scan mass spectrum (300–1750 m/z, resolution of

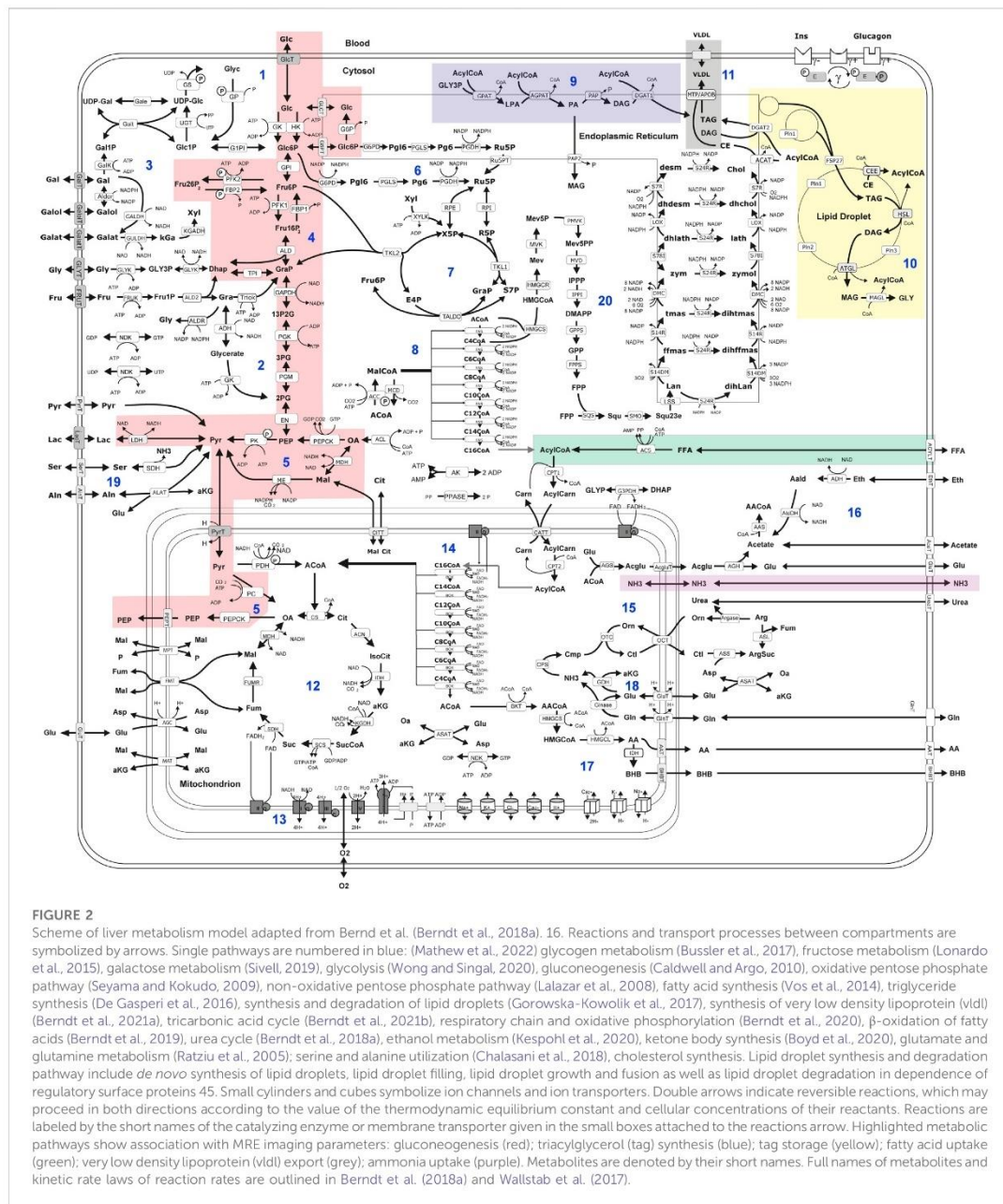


FIGURE 2 Scheme of liver metabolism model adapted from Berndt et al. (Berndt et al., 2018a). 16. Reactions and transport processes between compartments are symbolized by arrows. Single pathways are numbered in blue: (Mathew et al., 2022) glycogen metabolism (Bussler et al., 2017), fructose metabolism (Lonardo et al., 2015), galactose metabolism (Sivell, 2019), glycolysis (Wong and Singal, 2020), gluconeogenesis (Caldwell and Argo, 2010), oxidative pentose phosphate pathway (Seyama and Kokudo, 2009), non-oxidative pentose phosphate pathway (Lalazar et al., 2008), fatty acid synthesis (Vos et al., 2014), triglyceride synthesis (De Gasperi et al., 2016), synthesis and degradation of lipid droplets (Gorowska-Kowolik et al., 2017), synthesis of very low density lipoprotein (vldl) (Berndt et al., 2021a), tricarboxylic acid cycle (Berndt et al., 2021b), respiratory chain and oxidative phosphorylation (Berndt et al., 2020), β -oxidation of fatty acids (Berndt et al., 2019), urea cycle (Berndt et al., 2018a), ethanol metabolism (Kespohl et al., 2020), ketone body synthesis (Boyd et al., 2020), glutamate and glutamine metabolism (Ratzju et al., 2005); serine and alanine utilization (Chalasanani et al., 2018), cholesterol synthesis. Lipid droplet synthesis and degradation pathway include *de novo* synthesis of lipid droplets, lipid droplet filling, lipid droplet growth and fusion as well as lipid droplet degradation in dependence of regulatory surface proteins 45. Small cylinders and cubes symbolize ion channels and ion transporters. Double arrows indicate reversible reactions, which may proceed in both directions according to the value of the thermodynamic equilibrium constant and cellular concentrations of their reactants. Reactions are labeled by the short names of the catalyzing enzyme or membrane transporter given in the small boxes attached to the reactions arrow. Highlighted metabolic pathways show association with MRE imaging parameters: gluconeogenesis (red); triacylglycerol (tag) synthesis (blue); tag storage (yellow); fatty acid uptake (green); very low density lipoprotein (vldl) export (grey); ammonia uptake (purple). Metabolites are denoted by their short names. Full names of metabolites and kinetic rate laws of reaction rates are outlined in Berndt et al. (2018a) and Wallstab et al. (2017).

60,000 at m/z 200, automatic gain control (AGC) target 1×10^6 was followed by 12 data-dependent MS/MS scans (resolution of 30,000, AGC target 5×10^5) with a normalized collision energy of 25 eV.

Raw MS data were processed with MaxQuant software (v 1.6.1.43) and searched against the *Oryctolagus cuniculus* (rabbit) proteome

database UniProtKB (UP000001811) with 21,178 entries, released in September 2019. Parameters of MaxQuant database searching were a false discovery rate (FDR) of .01 for proteins and peptides, cysteine carbamidomethylation was set as fixed modification, while N-terminal acetylation and methionine oxidation were set as variable

modifications. The mass spectrometry proteomics data have been deposited to the ProteomeXchange Consortium via the PRIDE (Perez-Riverol et al., 2022) partner repository with the dataset identifier PXD036659.

2.4 Assessment of metabolic capacities

Hepatic metabolic capacities were assessed using HEPATOKIN1 (Berndt et al., 2018a) in combination with a molecular-resolution model of hepatic lipid droplet metabolism (Wallstab et al., 2017). It comprises the major metabolic pathways of carbohydrate, lipid and amino-acid metabolism in hepatocytes (see Figure 2). Electrophysiological processes at the inner mitochondrial membrane describing the generation and utilization of the proton motive force were modelled by kinetic equations of the Goldman-Hodgkin-Katz type (Berndt et al., 2015). Hormone-dependent regulation of the liver metabolism by reversible enzyme phosphorylation was taken into account by a phenomenological transfer function (Bulik et al., 2016). Individual model instantiations were generated based on proteomic profiles as described in Berndt et al. (2019).

Physiological metabolic functions were defined as maximal fluxes obtained under a wide range of physiological conditions (3–12 mM plasma glucose), where plasma metabolite concentrations are not independent from each other. The interdependence between plasma glucose, plasma hormone and plasma fatty acid concentration was taken into account by using experimentally determined transfer functions (Bulik et al., 2016; Berndt et al., 2018a).

2.5 Statistical analysis

Statistical analysis and cluster analysis were done MATLAB Release 2021a (The MathWorks, Inc., Natick, MA, United States) with the bioinformatics toolbox. Group values were checked for normality based on quantile-quantile plots (qqPlots) with a 95% confidence interval margins. For normal distributed grouped values, unpaired two-sided students' *t*-test was used to calculate group differences. Otherwise, Wilcoxon signed-ranked test was used. Statistical analysis was performed using R version 4.0.2 (R-Foundation, Vienna, Austria). The level of significance was $p < .05$. Cluster analysis was performed using clustergram function. Row-wise normalization was used transforming values so that the mean of each metabolic function is 0 and the standard deviation is 1.

3 Results

3.1 Metabolic modelling

For the assessment of metabolic capabilities, we used personalized kinetic models to compute steady-state load characteristics describing the metabolic functions under a wide range of physiological conditions ranging from fasted state (low glucose, high fatty acids, low insulin and high glucagon) to a fed state (high glucose, low fatty acids, high insulin,

low glucagon). The remaining plasma nutrients (e.g., lactate, amino acids, ketone bodies, ammonia) were kept fixed at mean diurnal values (see Section 2.4 for more details).

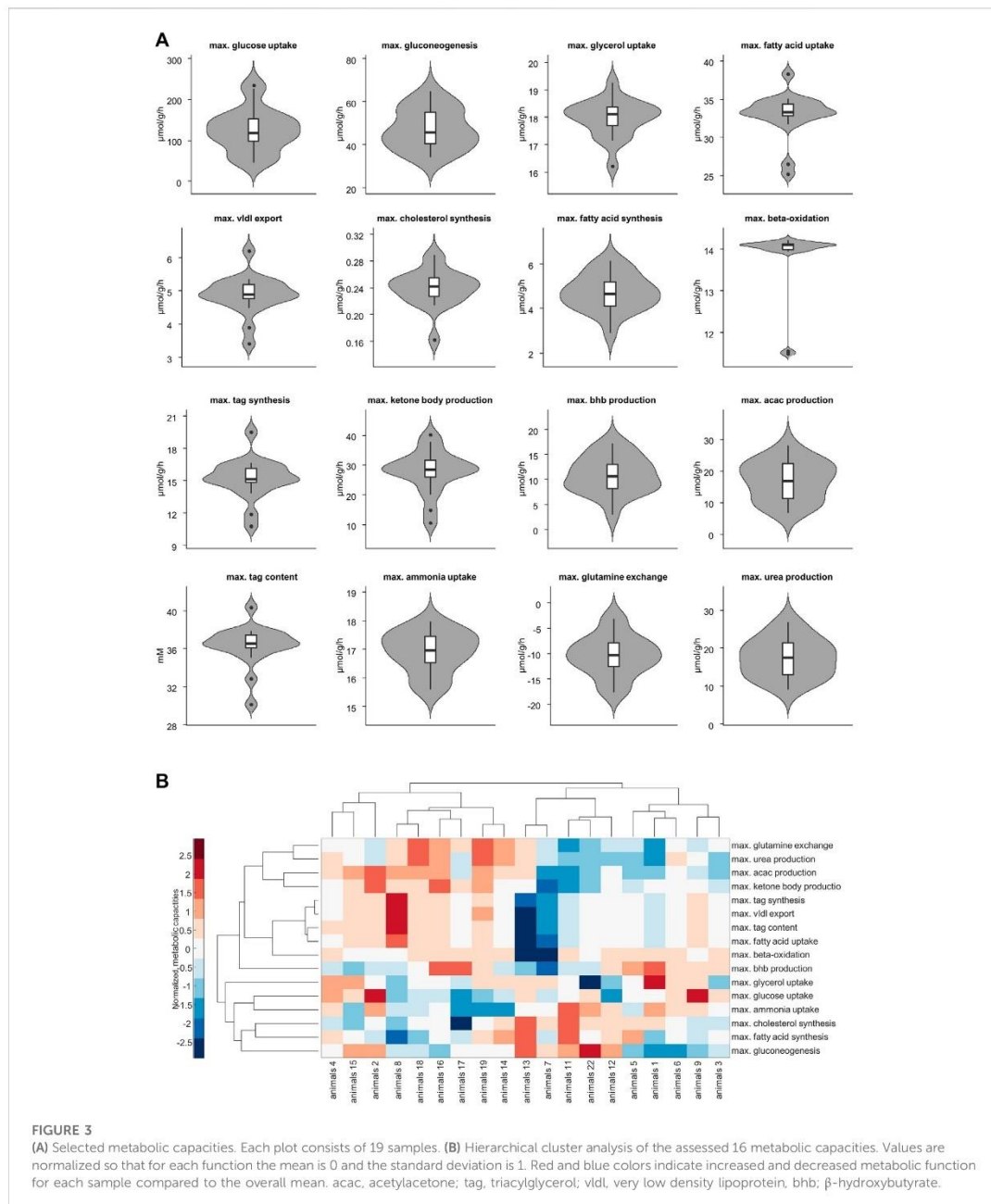
Figure 3A shows the panel of investigated metabolic capacities. Our analysis revealed strong metabolic differences among the individual livers. Individual livers differed in metabolic functions regarding carbohydrate metabolism, including glycolysis and gluconeogenesis, ketone body synthesis and fatty acid metabolism such as fatty acid uptake, lipoproteins production, triacylglycerol (tag) storage and fatty acid synthesis. We performed an unbiased cluster analysis to group the livers according to similarities in their metabolic functions. The cluster analysis depicted in Figure 3B shows that two main groups could be identified. Compared with the mean of all livers, metabolic cluster 2 is characterized by a less active metabolism of fatty acids, including reduced fatty acid uptake, reduced tag synthesis and storage as well as reduced ketone body synthesis. Instead, it has a higher synthetic capacity for glucose, fatty acids and cholesterol. Complementary, the metabolic cluster 1 has a more pronounced fatty acid metabolism and reduced biosynthetic activity than the mean of all livers.

We used the two metabolic clusters to define subgroups and investigated whether metabolic functions differ significantly between the two clusters. Cluster 1 consisted of 9 samples, whereas cluster 2 consisted of 10 samples. Figure 4 shows that the two groups differed significantly with respect to fatty acid uptake (34.7 ± 1.54 vs. 31.51 ± 3.1 $\mu\text{mol/g/h}$, $p = .001$), very low density lipoprotein (vldl) export (5.22 ± 0.42 vs. $4.56 \pm .54$ $\mu\text{mol/g/h}$, $p = .002$), cholesterol synthesis ($.22 \pm 0.03$ vs. $.25 \pm .02$ $\mu\text{mol/g/h}$, $p = .01$), tag synthesis (16.32 ± 1.35 vs. 14.15 ± 1.67 $\mu\text{mol/g/h}$, $p = .001$), ketone body production (32.91 ± 4.04 vs. 23.23 ± 6.31 $\mu\text{mol/g/h}$, $p = .001$), acetylaceton (acac) production (21.95 ± 3.6 vs. 12.53 ± 4.28 , $p < .001$ $\mu\text{mol/g/h}$), tag content (37.48 ± 1.24 vs. 35.31 ± 2.24 mM, $p = .01$), ammonia uptake ($16.49 \pm .73$ vs. $17.3 \pm .46$ $\mu\text{mol/g/h}$, $p = .013$), glutamine exchange (-7.54 ± 2.94 vs. -12.98 ± 3.12 $\mu\text{mol/g/h}$, $p = .001$), and urea production (20.96 ± 3.93 vs. 14.26 ± 3.88 $\mu\text{mol/g/h}$, $p = .002$).

We also checked whether the metabolic subgroups are characterized by significant differences in imaging markers. Figure 5 shows a representative slice of MRE and PET imaging parameters of rabbit's liver. SWS, PR and SUV values are given in Table 1. While no significant differences could be detected, PR shows a tendency to be lower in the livers with increased fatty acid metabolism and decreased biosynthetic capacities, hinting at a connection between non-invasive imaging markers and metabolic functionality.

Another approach to investigate the association of liver metabolism to liver mechanics was the clustering based on liver mechanics. Therefore, we divided the livers into two groups according to liver stiffness. Stiff livers were defined by SWS >1.6 m/s ($n = 10$), while soft livers were defined by a SWS <1.6 m/s ($n = 9$), corresponding to the median of all SWS values of the rabbits. Using this classification, we again compared metabolic functions and non-invasive imaging markers between these two groups to see, whether liver stiffness can be used to differentiate hepatic metabolic functionality.

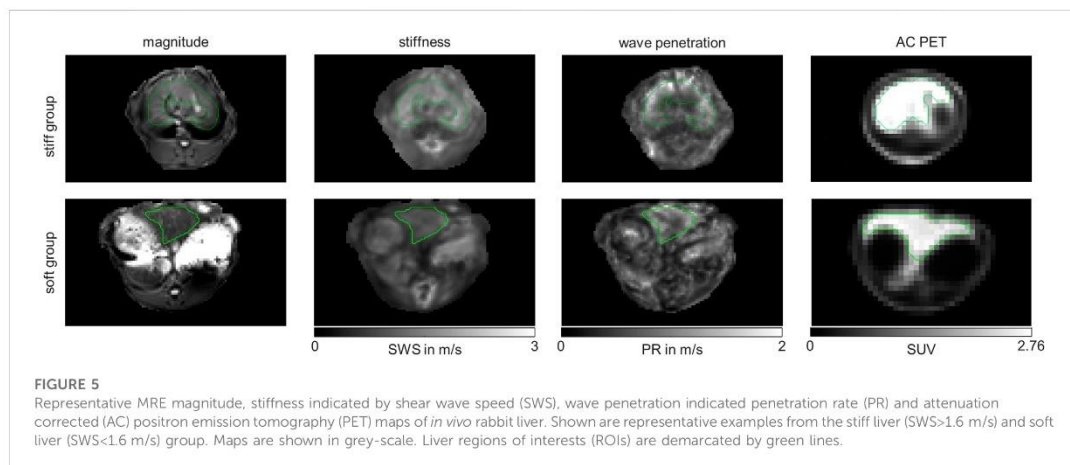
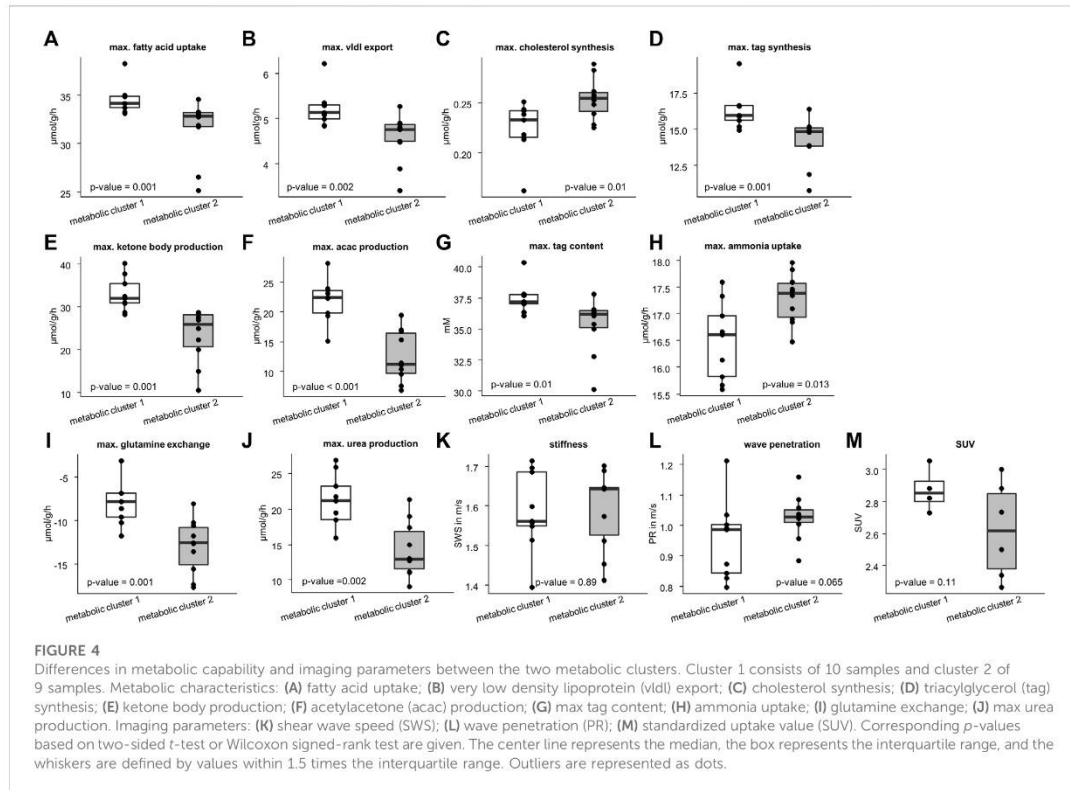
Figure 6 shows that stiff livers had a significantly higher capacity for gluconeogenesis (-52.81 ± 9.48 vs. -42.55 ± 6.17 $\mu\text{mol/g/h}$, $p = .016$), cholesterol synthesis ($.25 \pm .04$ vs. $.23 \pm .01$ $\mu\text{mol/g/h}$, $p = .035$),



and tag content (35.32 ± 2.45 vs. 37.26 ± 1.25 mM, $p = .043$). Besides increased SWS, the parameter PR was also significantly higher in stiff livers than in soft livers ($1.06 \pm .08$ vs. $.93 \pm .1$ m/s, $p = .02$) and a linear correlation between SWS and PR was observed ($r = .59$, $p = .008$, Figure 7A).

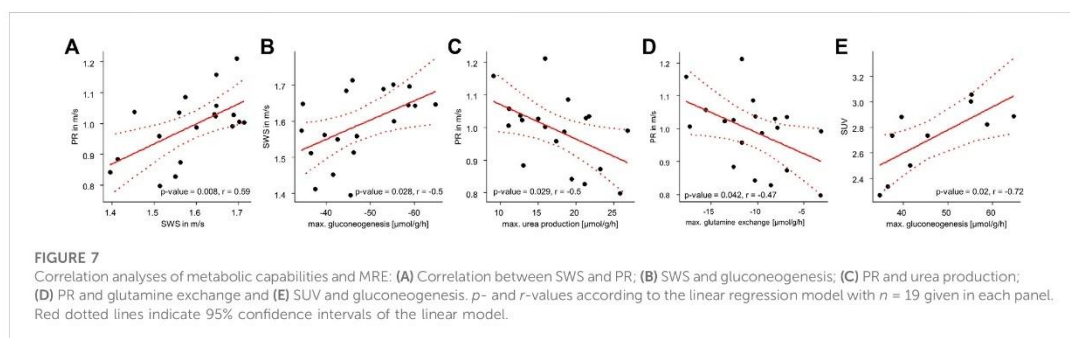
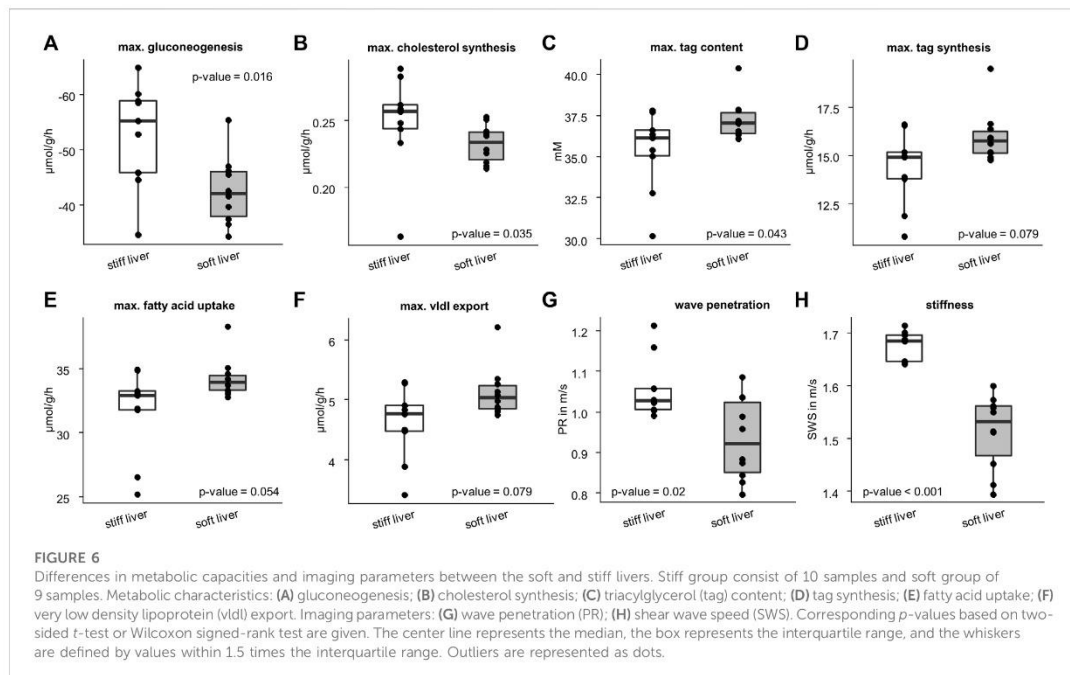
3.2 Correlations of metabolic functions with MRE parameters

So far, we have shown, that metabolic functionality can be used to define metabolic subclasses in healthy livers and that these subclasses



can be detected by MRE based on liver viscosity. Vice versa we showed, that differentiating between stiff and soft livers allows classification of metabolic functionality. While subgroups enable the metabolic and biomechanical classification of livers, the question remains, whether individual metabolic functions can possibly be assessed by MRE. To

answer this question, we correlated individual metabolic liver functions with liver SWS and PR. SWS was significantly correlated with gluconeogenesis ($r = -.5, p = .028$, Figure 7B), while PR was correlated with urea production ($r = -.5, p = .029$, Figure 7C) and glutamine exchange ($r = -.47, p = .042$, Figure 7D). Interestingly, SUV



was correlated with gluconeogenesis ($r = -0.72$, $p = .02$, Figure 7E), although not with glucose uptake.

4 Discussion

In this study, we demonstrated for the first time the feasibility of MRE in small animals using a clinical hybrid PET/MRI scanner. This PET/MRE system allowed us to generate maps related to stiffness and viscosity, as well as ^{18}F -FDG uptake simultaneously; this allowed the first-ever investigation of the correlation between metabolism and viscoelasticity. Furthermore, we harvested liver tissue after euthanasia for

modeling liver metabolism of key metabolic markers for each individual rabbit.

The first important finding of our study was a surprisingly large heterogeneity in metabolic capacities among the healthy rabbit livers. Although all the rabbits were genetically identical and received the same nutrition, there were clear differences in fatty-acid metabolism, ketone-body synthesis and urea metabolism. While this is the first time we studied rabbit liver, variability in metabolic capacities were also shown in healthy mouse liver as well as human pediatric patients with moderate liver fibrosis (Berndt et al., 2021b; Berndt et al., 2022).

Direct evaluation of metabolic fluxes *in vivo* remains an expensive experimental challenge. Estimation of *in vivo* fluxes by measuring time series of labeled nutrients (Hasenour et al., 2015; Hui et al., 2020;

Rahim et al., 2021) is restricted to the analysis of very few pathways and gives the average flux rate during the time of measurement, but it is not suited for monitoring metabolic fluxes over a longer period of varying physical activity and plasma profiles of nutrients. Furthermore, metabolic flux rates depend not only on the availability of the substrate of interest but also on the overall plasma nutrient and hormone composition making it hard to assess all the information necessary to define the observed metabolic state.

In our approach we assessed metabolic capacities rather than actual fluxes. We evaluated 16 different metabolic capacities under a wide range of physiological conditions ranging from fasted state (low glucose, high fatty acids, low insulin, and high glucagon) to a fed state (high glucose, low fatty acids, high insulin, low glucagon). The remaining plasma nutrients (e.g., lactate, amino acids, ketone bodies, ammonia) were kept fixed at mean diurnal values (see Berndt et al., 2018a for more details).

In this study, we circumvented these problems by evaluation of metabolic capacities based on protein abundances under pre-described conditions rather than actual fluxes. This allowed us to robustly assess the metabolic differences which are not prone to short-term variations due to varying metabolic conditions because metabolic enzymes are stable for hours (see Berndt and Holzthutter, 2018 and references within). It is important to note that the metabolic capacities assessed in this way do not themselves form a consistent metabolic state, since conditions under which they are realized are not the same. For example, maximal gluconeogenesis is reached under low glucose conditions, while maximal glycolysis is reached under high glucose conditions.

The differences in metabolic capacities allowed a rough classification of the livers into two clusters. Cluster 2 was characterized by reduced fatty-acid metabolism and increased biosynthetic capacity, while cluster 1 displayed the opposite metabolic characteristics. While statistically not significant, probably owing to the low sample number, a similar trend was seen in ^{18}F -FDG uptake as measured by PET ($p = .11$). Importantly, the two metabolic clusters showed a clear distinction in mechanical properties: cluster 1 was more viscous (lower PR) than cluster 2, albeit again without statistical significance ($p = .065$).

Alternatively, classification of livers according to their biomechanical properties may provide an indication of metabolic functions. Therefore, we classified livers according to their mechanical properties. The clustering in two groups based on the cutoff value of 1.6 m/s for the liver SWS agrees with SWS values of a healthy human liver, i.e., approximately 1.4 m/s for 30–60 Hz when considering the dispersion of SWS in the liver as analyzed by Morr et al. (2022). This biomechanical classification revealed that stiff livers differ significantly from soft livers in their metabolic capacities. Specifically, stiff livers have a markedly reduced tag content, while showing increased capacity for gluconeogenesis and cholesterol synthesis. This observation agrees with recent findings in adipose tissue, where a decrease in stiffness was associated with excessive accumulation of lipids (Abuhattum et al., 2022). In future studies, it would be interesting to investigate whether increased gluconeogenesis activity associated with increased liver stiffness is an early marker of pathologically altered metabolism toward NAFLD.

We also studied which liver functions are directly associated with mechanical parameters. Figure 7 shows that PR is

significantly correlated with hepatic capacities of urea production and glutamine exchange. It is noteworthy that these metabolic capacities are not independent of one another, as ammonia detoxification can take place either by urea production or by glutamine synthesis.

One may speculate whether the observed correlations indicate a causal relationship between liver biomechanics and metabolic function. However, it is important to note that short-term physiological changes such as prandial state or perfusion rate induce acute changes in the liver's mechanical properties within seconds or minutes (Yin et al., 2011; Jajamovich et al., 2014; Dittmann et al., 2017; Manduca et al., 2021; Obrzut et al., 2021). In contrast, alterations in metabolic capacities due to variable protein abundance represent long-term adaptations taking place over hours or days (Berndt and Holzthutter, 2018). To reduce the confounding influence of physiological fluctuations on the mechanical properties of the liver, rabbits were fasted before the measurements. Sedation of rabbits reduced heart rate and breathing frequency while physiological short-term effects should have averaged out during the 8 min MRE examination time. Overall, the coefficient of variation of liver stiffness was 6% which is lower than in other MRE studies in healthy rabbit livers (14%–42%, [Zou et al., 2016; Zou et al., 2020; Zou et al., 2022]), suggesting a minor effect of physiological fluctuations on the measured mechanical properties.

Long-term architectural changes related to metabolism are conceivable when one considers ultrastructural liver properties such as extracellular collagen deposition or cellular fat accumulation. As discussed earlier, these structural changes directly affect mechanical properties but could also be associated with metabolic capacities (Sasso et al., 2016; Hudert et al., 2019). For example, excessive storage of tag might indicate an increased capacity for fatty-acid uptake and concomitant production of lipoproteins from these fatty acids. Collagen deposition and liver fibrosis, on the other hand, might alter substrate availability by alterations in hepatic blood flow and perfusion pressure, and thereby alter the capacities of glucose metabolism that respond directly to glucose availability (Berndt et al., 2018b). Hence, a close interaction between liver structure and metabolism would result in a correlation between viscoelastic properties and clusters of metabolic markers, as indeed observed in this study.

It should be emphasized that our results were obtained from healthy rabbit livers. We anticipate larger effects in livers with diseases such as NAFLD, and would expect such diseases to be readily detectable by *in vivo* MRE. For example, PR was shown by MRE to correlate negatively with the degree of hepatic steatosis in children with NAFLD at the same time that liver stiffness increased (Hudert et al., 2019). This is consistent with our analysis, in which stiffer livers were associated with reduced fatty-acid metabolism and increased biosynthetic capacity. Hence, the results of our study may explain findings in the literature, and they put MRE forward as a potentially sensitive tool for further studies on the relationship between liver function and viscoelastic properties.

Although encouraging, our study has limitations. First, only a small portion of the liver was used for proteomic analysis, whereas the MRE investigation covered most of the liver. Regional heterogeneity or different fractions of portal and central liver regions could affect proteomics-based metabolic capacities (Berndt et al., 2021b). Because healthy livers were used, we

assume no regional heterogeneity. Secondly, MRE measurements were performed under free breathing, which could have led to respiratory artifacts. However, the rabbits in our study were under deep sedation to minimize any respiration-induced distortions. Furthermore, in earlier work we showed that MRE performed under free breathing yields values similar to those obtained by MRE under breath hold (Shahryari et al., 2021). Thirdly, this pilot study included only 19 healthy rabbits. Future studies with more animals and disease models such as NASH are needed to further investigate the association of liver mechanical parameters with metabolism. Furthermore, PET measurements were performed only in a subset of rabbits for cost reasons. Therefore, metabolic cluster group 1 consists of only four data points, which does not allow statistical conclusions.

In summary, this study has revealed the relationship between liver metabolism analyzed by proteomics-based modeling and viscoelastic parameters measured with MRE *in vivo*. We demonstrate for the first time the feasibility of MRE in small animals using a clinical hybrid PET/MRI scanner. A surprisingly large heterogeneity of metabolic capacities was found in healthy rabbit livers, manifested by marked differences in carbohydrate metabolism, ketone body synthesis and fatty-acid metabolism. Biomechanical classification revealed that stiff livers are distinctly different from soft livers in that they have a lower capacity for triacylglycerol storage, while at the same time showing an increased capacity for gluconeogenesis and cholesterol synthesis. The sensitivity of MRE parameters to key metabolic functions in the liver suggests that MRE holds promise as a potentially useful noninvasive method for the assessment of liver function capacity in the future.

Data availability statement

The mass spectrometry proteomics dataset presented in this study can be found in an online repository. The name of the repository and accession number can be found below: <https://www.ebi.ac.uk/pride/archive/>, PXD036659. The raw imaging dataset presented in this study will be made available by the authors upon reasonable request.

References

- Abuhattum, S., Kotzbeck, P., Schlüßler, R., Harger, A., Ariza de Schellenberger, A., Kim, K., et al. (2022). Adipose cells and tissues soften with lipid accumulation while in diabetes adipose tissue stiffens. *Sci. Rep.* 12 (1), 10325. doi:10.1038/s41598-022-13324-9
- Berndt, N., and Holzhütter, H. G. (2018). Dynamic metabolic zonation of the hepatic glucose metabolism is accomplished by sinusoidal plasma gradients of nutrients and hormones. *Front. Physiol.* 9, 1786. doi:10.3389/fphys.2018.01786
- Berndt, N., Kann, O., and Holzhütter, H. G. (2015). Physiology-based kinetic modeling of neuronal energy metabolism unravels the molecular basis of NAD(P)H fluorescence transients. *J. Cereb. Blood Flow. Metab.* 35 (9), 1494–1506. doi:10.1038/jcbfm.2015.70
- Berndt, N., Bulik, S., Wallach, I., Wünsch, T., König, M., Stockmann, M., et al. (2018a). HEPATOKIN1 is a biochemistry-based model of liver metabolism for applications in medicine and pharmacology. *Nat. Commun.* 9 (1), 2386. doi:10.1038/s41467-018-04720-9
- Berndt, N., Horgor, M. S., Bulik, S., and Holzhütter, H. G. (2018b). A multiscale modelling approach to assess the impact of metabolic zonation and microperfusion on the hepatic carbohydrate metabolism. *PLoS Comput. Biol.* 14 (2), e1006005. doi:10.1371/journal.pcbi.1006005
- Berndt, N., Eckstein, J., Heucke, N., Gajowski, R., Stockmann, M., Meierhofer, D., et al. (2019). Characterization of lipid and lipid droplet metabolism in human HCC. *Cells* 8 (5), 512. doi:10.3390/cells8050512
- Berndt, N., Egners, A., Mastrobuoni, G., Vvedenskaya, O., Fragoulis, A., Dugourd, A., et al. (2020). Kinetic modelling of quantitative proteome data predicts metabolic reprogramming of liver cancer. *Br. J. Cancer* 122 (2), 233–244. doi:10.1038/s41416-019-0659-3
- Berndt, N., Kolbe, E., Gajowski, R., Eckstein, J., Ott, F., Meierhofer, D., et al. (2021a). Functional consequences of metabolic zonation in murine livers: Insights for an old story. *Hepatology* 73 (2), 795–810. doi:10.1002/hep.31274
- Berndt, N., Eckstein, J., Heucke, N., Wuensch, T., Gajowski, R., Stockmann, M., et al. (2021b). Metabolic heterogeneity of human hepatocellular carcinoma: implications for personalized pharmacological treatment. *FEBS J.* 288 (7), 2332–2346. doi:10.1111/febs.15587
- Berndt, N., Hudert, C. A., Eckstein, J., Loddikenper, C., Henning, S., Bufler, P., et al. (2022). Alterations of central liver metabolism of pediatric patients with non-alcoholic fatty liver disease. *Int. J. Mol. Sci.* 23 (19), 11072. doi:10.3390/ijms231911072
- Boyd, A., Cain, O., Chauhan, A., and Webb, G. J. (2020). Medical liver biopsy: Background, indications, procedure and histopathology. *Frontline Gastroenterol.* 11 (1), 40–47. doi:10.1136/flgastro-2018-101139
- Bulik, S., Holzhütter, H.-G., and Berndt, N. (2016). The relative importance of kinetic mechanisms and variable enzyme abundances for the regulation of hepatic glucose metabolism – insights from mathematical modeling. *BMC Biol.* 14 (1), 15. doi:10.1186/s12915-016-0237-6

Ethics statement

The animal study was reviewed and approved by Landesamt für Gesundheit und Soziales Berlin (Reg. No. 0178/17).

Author contributions

Conceptualization: MS, SK, MM, IS and NB; methodology: MS, SK, DM, IW, JB, NB and IS; software: MS, IW and NB; validation: MS, IW and NB; formal analysis: MS, IW and NB; investigation: MS, SK, DM, IW, NB and IS; resources: MS, SK, DM, IW, JB, MM, IS and NB; data curation: MS, IW, DM and NB; writing—original draft: MS, IS and NB; writing—review and editing: MS, SK, DM, IW, YS, JG, SRMG, JB, MM, IS and NB; visualization: MS, NB; supervision: MM, IS and NB; funding acquisition: JB, MM and IS.

Acknowledgments

We acknowledge financial support from the Open Access Publication Fund of Charité—Universitätsmedizin Berlin and the German Research Foundation (DFG, SFB1340 Matrix in Vision, GRK2260 BIOQIC).

Conflict of interest

The authors declare that the research was conducted in the absence of any commercial or financial relationships that could be construed as a potential conflict of interest.

Publisher's note

All claims expressed in this article are solely those of the authors and do not necessarily represent those of their affiliated organizations, or those of the publisher, the editors and the reviewers. Any product that may be evaluated in this article, or claim that may be made by its manufacturer, is not guaranteed or endorsed by the publisher.

- Bussler, S., Penke, M., Flemming, G., Elhassan, Y. S., Kratzsch, J., Sergeyev, E., et al. (2017). Novel insights in the metabolic syndrome in childhood and adolescence. *Horm. Res. Paediatr.* 88 (3–4), 181–193. doi:10.1159/000479510
- Caldwell, S., and Argo, C. (2010). The natural history of non-alcoholic fatty liver disease. *Dig. Dis.* 28 (1), 162–168. doi:10.1159/000282081
- Castera, L., Friedrich-Rust, M., and Loomba, R. (2019). Noninvasive assessment of liver disease in patients with nonalcoholic fatty liver disease. *Gastroenterology* 156 (5), 1264–1281.e4. doi:10.1053/j.gastro.2018.12.036
- Chalasan, N., Younossi, Z., Lavine, J. E., Charlton, M., Cusi, K., Rinella, M., et al. (2018). The diagnosis and management of nonalcoholic fatty liver disease: Practice guidance from the American Association for the Study of Liver Diseases. *Hepatology* 67 (1), 328–357. doi:10.1002/hep.29367
- De Gasperi, A., Mazza, E., and Prosperi, M. (2016). Indocyanine green kinetics to assess liver function: Ready for a clinical dynamic assessment in major liver surgery? *World J. Hepatol.* 8, 355. doi:10.4254/wjvh.v8.i7.355
- Dittmann, F., Tzschätzsch, H., Hirsch, S., Barnhill, E., Braun, J., Sack, I., et al. (2017). Tomoelastography of the abdomen: Tissue mechanical properties of the liver, spleen, kidney, and pancreas from single MR elastography scans at different hydration states. *Magnetic Reson. Med.* 78 (3), 976–983. doi:10.1002/mrm.26484
- Garczyńska, K., Tzschätzsch, H., Kühn, A. A., Morr, A. S., Lilaj, L., Häckel, A., et al. (2020). Changes in liver mechanical properties and water diffusivity during normal pregnancy are driven by cellular hypertrophy. *Front. Physiol.* 11, 605205. doi:10.3389/fphys.2020.605205
- Gielisch, L., and Meierhofer, D. (2015). Metabolome and proteome profiling of complex I deficiency induced by rotenone. *J. Proteome Res.* 14 (1), 224–235. doi:10.1021/pr500894v
- Gorowska-Kowolik, K., Chobot, A., and Kwiecien, J. (2017). ^{13}C methacetin breath test for assessment of microsomal liver function: Methodology and clinical application. *Gastroenterol. Res. Pract.* 2017, 1–5. doi:10.1155/2017/7397840
- Hasenour, C. M., Wall, M. L., Ridley, D. E., Hughey, C. C., James, F. D., Wasserman, D. H., et al. (2015). Mass spectrometry-based microassay of 2H and 13C plasma glucose labeling to quantify liver metabolic fluxes *in vivo*. *Am. J. Physiol.-Endocrinol. Metab.* 309 (2), E191–E203. doi:10.1152/ajpendo.00003.2015
- Herthum, H., Hetzer, S., Scheel, M., Shahryari, M., Braun, J., Paul, F., et al. (2022). *In vivo* stiffness of multiple sclerosis lesions is similar to that of normal-appearing white matter. *Acta Biomater.* 138, 410–421. doi:10.1016/j.actbio.2021.10.038
- Heucke, N., Wuensch, T., Mohr, J., Kaffarnik, M., Arsenic, R., Sinn, B., et al. (2019). Non-invasive structure-function assessment of the liver by 2D time-harmonic elastography and the dynamic Liver MAXimum capacity (LiMAx) test. *J. Gastroenterol. Hepatol.* 34 (9), 1611–1619. doi:10.1111/jgh.14629
- Hudert, C. A., Tzschätzsch, H., Rudolph, B., Bläker, H., Loddenkemper, C., Müller, H-P., et al. (2019). Tomoelastography for the evaluation of pediatric nonalcoholic fatty liver disease. *Investig. Radiol.* 54 (4), 198–203. doi:10.1097/rli.0000000000000529
- Hudert, C. A., Tzschätzsch, H., Rudolph, B., Loddenkemper, C., Holzhütter, H-G., Kalveram, L., et al. (2021). How histopathologic changes in pediatric nonalcoholic fatty liver disease influence *in vivo* liver stiffness. *Acta Biomater.* 123, 178–186. doi:10.1016/j.actbio.2021.01.019
- Hui, S., Cowan, A. J., Zeng, X., Yang, L., TeLsa, T., Li, X., et al. (2020). Quantitative fluxomics of circulating metabolites. *Cell Metab.* 32 (4), 676–688.e4. doi:10.1016/j.cmet.2020.07.013
- Huwart, L., Sempoux, C., Vicaut, E., Salameh, N., Annet, L., Danse, E., et al. (2008). Magnetic resonance elastography for the noninvasive staging of liver fibrosis. *Gastroenterology* 135 (1), 32–40. doi:10.1053/j.gastro.2008.03.076
- Ipek-Uğay, S., Tzschätzsch, H., Hudert, C., Marticorena Garcia, S. R., Fischer, T., Braun, J., et al. (2016). Time harmonic elastography reveals sensitivity of liver stiffness to water ingestion. *Ultrasound Med. Biol.* 42 (6), 1289–1294. doi:10.1016/j.ultrasmedbio.2015.12.026
- Jajamovich, G. H., Dyvorne, H., Donnerhack, C., and Taouli, B. (2014). Quantitative liver MRI combining phase contrast imaging, elastography, and DWI: Assessment of reproducibility and postprandial effect at 3.0 T. *PLOS ONE* 9 (5), e97355. doi:10.1371/journal.pone.0097355
- Kesphol, M., Bredow, C., Klingel, K., Voss, M., Paeschke, A., Zickler, M., et al. (2020). Protein modification with ISG15 blocks coxsackievirus pathology by antiviral and metabolic reprogramming. *Sci. Adv.* 6 (11), eaay1109. doi:10.1126/sciadv.aay1109
- Lalazar, G., Pappo, O., Hershcovici, T., Hadjaj, T., Shubi, M., Ohana, H., et al. (2008). A continuous 13C methacetin breath test for noninvasive assessment of intrahepatic inflammation and fibrosis in patients with chronic HCV infection and normal ALT. *J. Viral Hepat.* 15 (10), 716–728. doi:10.1111/j.1365-2893.2008.01007.x
- Lin, H., Wang, Y., Zhou, J., Yang, Y., Xu, X., Ma, D., et al. (2022). Tomoelastography based on multifrequency MR elastography predicts liver function reserve in patients with hepatocellular carcinoma: a prospective study. *Insights into Imaging* 13 (1), 95. doi:10.1186/s13244-022-01232-5
- Lonardo, A., Ballestri, S., Marchesini, G., Angulo, P., and Loria, P. (2015). Nonalcoholic fatty liver disease: a precursor of the metabolic syndrome. *Dig. Liver Dis.* 47 (3), 181–190. doi:10.1016/j.dld.2014.09.020
- Manduca, A., Bayly, P. J., Ehman, R. L., Kolipaka, A., Royston, T. J., Sack, I., et al. (2021). MR elastography: Principles, guidelines, and terminology. *Magnetic Reson. Med.* 85 (5), 2377–2390. doi:10.1002/mrm.28627
- Mathew, P., and Thoppil, D. Hypoglycemia (2022). *StatPearls*. Treasure Island (FL): StatPearls Publishing LLC. StatPearls Publishing Copyright © 2022.
- Meyer, T., Tzschätzsch, H., Wellge, B., Sack, I., Kröncke, T., and Mard, A. (2022a). Valsalva maneuver decreases liver and spleen stiffness measured by time-harmonic ultrasound elastography. *Front. Bioeng. Biotechnol.* 10, 886363. doi:10.3389/fbioe.2022.886363
- Meyer, T., Marticorena Garcia, S., Tzschätzsch, H., Herthum, H., Shahryari, M., Stencil, L., et al. (2022b). Comparison of inversion methods in MR elastography: An open-access pipeline for processing multifrequency shear-wave data and demonstration in a phantom, human kidneys, and brain. *Magn. Reson. Med.* 88, 1840–1850. doi:10.1002/mrm.29320
- Morr, A. S., Herthum, H., Schrank, F., Görner, S., Anders, M. S., Lerchbaumer, M., et al. (2022). Liquid-liver phantom: Mimicking the viscoelastic dispersion of human liver for ultrasound- and MRI-based elastography. *Investig. Radiol.* 57 (8), 502–509. doi:10.1097/rli.0000000000000862
- Obrzut, M., Atamaniuk, V., Chen, J., Obrzut, B., Ehman, R. L., Cholewa, M., et al. (2021). Postprandial hepatic stiffness changes on magnetic resonance elastography in healthy volunteers. *Sci. Rep.* 11 (1), 19786. doi:10.1038/s41598-021-99243-7
- Perez-Riverol, Y., Bai, J., Bandla, C., Garcia-Seisdedos, D., Hewapathirana, S., Kamatchinathan, S., et al. (2022). The PRIDE database resources in 2022: a hub for mass spectrometry-based proteomics evidences. *Nucleic Acids Res.* 50 (D1), D543–D552. doi:10.1093/nar/gkab1038
- Petzold, G., Porsche, M., Ellenrieder, V., Kunsch, S., and Neesse, A. (2019). Impact of food intake on liver stiffness determined by 2-D shear wave elastography: Prospective interventional study in 100 healthy patients. *Ultrasound Med. Biol.* 45 (2), 402–410. doi:10.1016/j.ultrasmedbio.2018.09.021
- Qu, Y., Middleton, M. S., Loomba, R., Glaser, K. J., Chen, J., Hooker, J. C., et al. (2021). Magnetic resonance elastography biomarkers for detection of histologic alterations in nonalcoholic fatty liver disease in the absence of fibrosis. *Eur. Radiol.* 31 (11), 8408–8419. doi:10.1007/s00330-021-07988-6
- Rahim, M., Hasenour, C. M., Bednarski, T. K., Hughey, C. C., Wasserman, D. H., and Young, J. D. (2016). Multitissue 2H/13C flux analysis reveals reciprocal upregulation of renal gluconeogenesis in hepatic PEPC-K-knockout mice. *JCI Insight* 6 (12), e149278. doi:10.1172/jci.insight.149278
- Ratziu, V., Charlotte, F., Heurtier, A., Gombert, S., Giral, P., Bruckert, E., et al. (2005). Sampling variability of liver biopsy in nonalcoholic fatty liver disease. *Gastroenterology* 128 (7), 1898–1906. doi:10.1053/j.gastro.2005.03.084
- Reiter, R., Tzschätzsch, H., Schwahofer, F., Haas, M., Bayerl, C., Muehle, M., et al. (2020). Diagnostic performance of tomoeelastography of the liver and spleen for staging hepatic fibrosis. *Eur. Radiol.* 30 (3), 1719–1729. doi:10.1007/s00330-019-06471-7
- Sasso, M., Audière, S., Kemgang, A., Gaouar, F., Corpechot, C., Chazouillères, O., et al. (2016). Liver steatosis assessed by controlled attenuation parameter (CAP) measured with the XL probe of the FibroScan: A pilot study assessing diagnostic accuracy. *Ultrasound Med. Biol.* 42 (1), 92–103. doi:10.1016/j.ultrasmedbio.2015.08.008
- Shvaraj, E. A., Mózes, F. E., Jayaswal, A. N. A., Zafarmand, M. H., Vali, Y., Lee, J. A., et al. (2021). Diagnostic accuracy of elastography and magnetic resonance imaging in patients with NAFLD: A systematic review and meta-analysis. *J. Hepatol.* 75 (4), 770–785. doi:10.1016/j.jhep.2021.04.044
- Seyama, Y., and Kokudo, N. (2009). Assessment of liver function for safe hepatic resection. *Hepatology* 49 (2), 107–116. doi:10.1016/j.jhep.2008.04.041.x
- Shahryari, M., Tzschätzsch, H., Guo, J., Marticorena Garcia, S. R., Böning, G., Fehrenbach, U., et al. (2019). Tomoelastography distinguishes noninvasively between benign and malignant liver lesions. *Cancer Res.* 79 (22), 5704–5710. doi:10.1158/0008-5472.can-19-2150
- Shahryari, M., Meyer, T., Warmuth, C., Herthum, H., Bertalan, G., Tzschätzsch, H., et al. (2021). Reduction of breathing artifacts in multifrequency magnetic resonance elastography of the abdomen. *Magn. Reson. Med.* 85 (4), 1962–1973. doi:10.1002/mrm.28558
- Singh, S., Venkatesh, S. K., Wang, Z., Miller, F. H., Motosugi, U., Low, R. N., et al. (2015). Diagnostic performance of magnetic resonance elastography in staging liver fibrosis: A systematic review and meta-analysis of individual participant data. *Clin. Gastroenterol. Hepatol.* 13 (3), 440–451.e6. doi:10.1016/j.cgh.2014.09.046
- Sivell, C. (2019). Nonalcoholic fatty liver disease: A silent epidemic. *Gastroenterol. Nurs.* 42 (5), 428–434. doi:10.1097/sga.0000000000000443
- Tzschätzsch, H., Guo, J., Dittmann, F., Hirsch, S., Barnhill, E., Jöhrens, K., et al. (2016). Tomoelastography by multifrequency wave number recovery from time-harmonic propagating shear waves. *Med. Image Anal.* 30, 1–10. doi:10.1016/j.media.2016.01.001
- Vos, J. J., Wietasch, J. K. G., Absalom, A. R., Hendriks, H. G. D., and Scheeren, T. W. L. (2014). Green light for liver function monitoring using indocyanine green? An overview of current clinical applications. *Anaesthesia* 69 (12), 1364–1376. doi:10.1111/anae.12755
- Wallstab, C., Eleftheriadou, D., Schulz, T., Damm, G., Seehofer, D., Borlak, J., et al. (2017). A unifying mathematical model of lipid droplet metabolism reveals key molecular players in the development of hepatic steatosis. *FEBS J.* 284, 3245–3261. doi:10.1111/febs.14189
- Wong, R. J., and Singal, A. K. (2020). Trends in liver disease etiology among adults awaiting liver transplantation in the United States, 2014–2019. *JAMA Netw. Open* 3 (2), e1920294–e. doi:10.1001/jamanetworkopen.2019.20294
- Yin, M., Talwalkar, J. A., Glaser, K. J., Venkatesh, S. K., Chen, J., Manduca, A., et al. (2011). Dynamic postprandial hepatic stiffness augmentation assessed with MR elastography in patients with chronic liver disease. *Am. J. Roentgenol.* 197 (1), 64–70. doi:10.2214/ajr.10.5989
- Zou, L., Jiang, J., Zhong, W., Wang, C., Xing, W., and Zhang, Z. (2016). Magnetic resonance elastography in a rabbit model of liver fibrosis: a 3-T longitudinal validation for clinical translation. *Am. J. Transl. Res.* 8 (11), 4922–4931.
- Zou, L.-Q., Zhao, F., Zhang, H., Zhang, K., and Xing, W. (2020). Staging liver fibrosis on multiparametric MRI in a rabbit model with elastography, susceptibility-weighted imaging and T1 ρ imaging: a preliminary study. *Acta Radiol.* 62 (2), 155–163. doi:10.1177/0284185120917117
- Zou, L., Jiang, J., Zhang, H., Zhong, W., Xiao, M., Xin, S., et al. (2022). Comparing and combining MRE, T1 ρ , SWI, IVIM, and DCE-MRI for the staging of liver fibrosis in rabbits: Assessment of a predictive model based on multiparametric MRI. *Magn. Reson. Med.* 87 (5), 2424–2435. doi:10.1002/mrm.29126

Publication 3: J.E.L. Jordan, G. Bertalan, T. Meyer, H. Tzschätzsch, A. Gauert, L. Bramè, H. Herthum, **Y. Safrou**, L. Schröder, J. Braun, Microscopic multifrequency MR elastography for mapping viscoelasticity in zebrafish, *Magnetic Resonance in Medicine* 87(3) (2022) 1435-1445.

<https://doi.org/10.1002/mrm.29066>

Journal Data Filtered By: **Selected JCR Year: 2022** Selected Editions: SCIE,SSCI
Selected Categories: **“RADIOLOGY, NUCLEAR MEDICINE and MEDICAL IMAGING”** Selected Category Scheme: WoS
Gesamtanzahl: 135 Journale

Rank	Full Journal Title	Total Cites	Journal Impact Factor	Eigenfaktor
40	JOURNAL OF NEURORADIOLOGY	1,505	3.5	0.00183
41	PHYSICS IN MEDICINE AND BIOLOGY	29,272	3.5	0.01938
42	SEMINARS IN RADIATION ONCOLOGY	2,801	3.5	0.00226
43	Biomedical Optics Express	14,699	3.4	0.01758
44	CANCER BIOTHERAPY AND RADIOPHARMACEUTICALS	2,857	3.4	0.00221
45	Physica Medica-European Journal of Medical Physics	5,488	3.4	0.00739
46	RADIATION RESEARCH	9,234	3.4	0.00370
47	ULTRASCHALL IN DER MEDIZIN	2,686	3.4	0.00262
48	DENTOMAXILLOFACIAL RADIOLOGY	4,025	3.3	0.00231
49	EUROPEAN JOURNAL OF RADIOLOGY	17,302	3.3	0.01536
50	JOURNAL OF THORACIC IMAGING	2,018	3.3	0.00199
51	MAGNETIC RESONANCE IN MEDICINE	32,434	3.3	0.02128
52	Practical Radiation Oncology	2,793	3.3	0.00482
53	EJNMMI Research	2,875	3.2	0.00429
54	CANADIAN ASSOCIATION OF RADIOLOGISTS JOURNAL- JOURNAL DE L ASSOCIATION CANADIENNE DES RADIOLOGISTES	1,513	3.1	0.00185
55	Clinical and Translational Radiation Oncology	1,540	3.1	0.00325
56	INTERNATIONAL JOURNAL OF HYPERTHERMIA	6,456	3.1	0.00520
57	MOLECULAR IMAGING AND BIOLOGY	3,530	3.1	0.00407
58	NUCLEAR MEDICINE AND BIOLOGY	3,714	3.1	0.00158
59	STRAHLENTHERAPIE UND ONKOLOGIE	3,580	3.1	0.00298



Received: 7 July 2021 | Revised: 12 October 2021 | Accepted: 14 October 2021

DOI: 10.1002/mrm.29066

RESEARCH ARTICLE

Magnetic Resonance in Medicine

Microscopic multifrequency MR elastography for mapping viscoelasticity in zebrafish

Jakob Ernst Luis Jordan¹ | Gergely Bertalan¹ | Tom Meyer¹ |
Heiko Tzschätzsch¹ | Anton Gauert^{2,3} | Luca Bramè^{2,3} | Helge Herthum⁴ |
Yasmine Safrou¹ | Leif Schröder⁵ | Jürgen Braun⁴ | Anja I. H. Hagemann² |
Ingolf Sack¹

¹Department of Radiology, Charité–Universitätsmedizin Berlin, Berlin, Germany

²Department of Hematology/Oncology, Charité–Universitätsmedizin Berlin, Berlin, Germany

³German Cancer Consortium (DKTK), German Cancer Research Center (DKFZ), Heidelberg, Germany

⁴Institute of Medical Informatics, Charité–Universitätsmedizin Berlin, Berlin, Germany

⁵Molecular Imaging, Leibniz-Forschungsinstitut für Molekulare Pharmakologie (FMP), Berlin, Germany

Correspondence

Ingolf Sack, Department of Radiology,
Charité–Universitätsmedizin Berlin,
Charitéplatz 1, 10117 Berlin, Germany.
Email: Ingolf.sack@charite.de

Funding information

Deutsche Forschungsgemeinschaft,
Grant/Award Number: BIOQIC, CRC
Matrix in Vision, GRK2260, SFB1340 and
Sa901/17-2

Purpose: The zebrafish (*Danio rerio*) has become an important animal model in a wide range of biomedical research disciplines. Growing awareness of the role of biomechanical properties in tumor progression and neuronal development has led to an increasing interest in the noninvasive mapping of the viscoelastic properties of zebrafish by elastography methods applicable to bulky and non-translucent tissues.

Methods: Microscopic multifrequency MR elastography is introduced for mapping shear wave speed (SWS) and loss angle (φ) as markers of stiffness and viscosity of muscle, brain, and neuroblastoma tumors in postmortem zebrafish with 60 μm in-plane resolution. Experiments were performed in a 7 Tesla MR scanner at 1, 1.2, and 1.4 kHz driving frequencies.

Results: Detailed zebrafish viscoelasticity maps revealed that the midbrain region (SWS = 3.1 ± 0.7 m/s, $\varphi = 1.2 \pm 0.3$ radian [rad]) was stiffer and less viscous than telencephalon (SWS = 2.6 ± 0.5 m/s, $\varphi = 1.4 \pm 0.2$ rad) and optic tectum (SWS = 2.6 ± 0.5 m/s, $\varphi = 1.3 \pm 0.4$ rad), whereas the cerebellum (SWS = 2.9 ± 0.6 m/s, $\varphi = 0.9 \pm 0.4$ rad) was stiffer but less viscous than both (all $p < .05$). Overall, brain tissue (SWS = 2.9 ± 0.4 m/s, $\varphi = 1.2 \pm 0.2$ rad) had similar stiffness but lower viscosity values than muscle tissue (SWS = 2.9 ± 0.5 m/s, $\varphi = 1.4 \pm 0.2$ rad), whereas neuroblastoma (SWS = 2.4 ± 0.3 m/s, $\varphi = 0.7 \pm 0.1$ rad, all $p < .05$) was the softest and least viscous tissue.

Conclusion: Microscopic multifrequency MR elastography-generated maps of zebrafish show many details of viscoelasticity and resolve tissue regions, of great

This is an open access article under the terms of the Creative Commons Attribution-NonCommercial-NoDerivs License, which permits use and distribution in any medium, provided the original work is properly cited, the use is non-commercial and no modifications or adaptations are made.

© 2021 The Authors. *Magnetic Resonance in Medicine* published by Wiley Periodicals LLC on behalf of International Society for Magnetic Resonance in Medicine.

interest in neuromechanical and oncological research and for which our study provides first reference values.

KEYWORDS

MR elastography, neuroblastoma, stiffness, tumors, viscoelasticity, zebrafish

1 | INTRODUCTION

Over the past 4 decades, zebrafish have emerged as a versatile animal model^{1,2} for a wide range of research areas, including embryology,³ oncology,⁴ tissue regeneration,⁵ and toxicology.⁶ The zebrafish genome is remarkably similar to that of humans: 70% of its genes are homologous to the human genome, and 82% of genes associated with human diseases have also been found in zebrafish.⁷ In addition, the optical transparency during embryonic development and in some adult genetically modified zebrafish lines, high fecundity, rapid growth rate, and comparative ease of husbandry make zebrafish an attractive animal model for biomedical research. Due to its early transparency, the accessibility of the offspring for tissue manipulations, and the diverse options of genetic manipulation, optical microscopy up to subcellular levels presents the most common method of investigation in the zebrafish.^{4,8,9} Combined with genetic analyses even on a single cell level, the zebrafish provides an optimal tool for tissue fate mapping in vivo.^{10,11} Mapping of the biophysical properties of zebrafish, however, is still in its infancy. Stiffness values of some zebrafish tissues have been reported based on invasively administered beads¹² and local optical tweezer experiments,¹³ which do not provide spatially resolved maps. Preliminary elastography data from zebrafish were obtained using ultrasonic elastography, but only averaged stiffness values for the central region of the fish were reported.¹⁴

MR elastography (MRE) is a versatile method that allows the noninvasive and 3D, spatially resolved mapping of viscoelasticity parameters in soft tissues for clinical diagnosis,¹⁵ and biomedical research.^{16–20} High-field MRE in small animal scanners has been applied to a wide variety of animal models, including Yucatan mini-pigs,²¹ ferrets,²² mice,^{18,23–25} rats,^{26,27} and frog oocytes.²⁸ In small animal models, MRE can provide maps of viscoelasticity with a pixel size on the order of 180 μm .²⁴ Higher resolution wave-encoding with 34 μm pixel size was demonstrated in gel phantoms and frog oocytes but without mapping the heterogeneity of viscoelastic parameters.²⁸ Given the very complex anatomy of zebrafish, high-resolution wave-encoding and viscoelasticity mapping based on multi-frequency inversion methods^{29,30} may promote MRE in zebrafish for biomedical research.

To this end, we developed a multifrequency MRE technique for a 7 Tesla small-animal MRI scanner, a cylindrical actuator in which a zebrafish can be placed, a piezoelectrical actuator that induced predominantly cylindrical waves, and a spin-echo MRE sequence. Together, these provide an in-plane resolution of 60 μm for depicting details of zebrafish mechanical anatomy. The relevance of this method for oncological research will be demonstrated in wild-type and a transgenic neuroblastoma zebrafish model (Tg(dbh:MYCN;dbh:EGFP). The transgenic fish develop neuroblastoma tumors together with a fluorescence reporter mainly in the interrenal gland orthologues to the human adrenal medulla.³¹ Subregional analysis was performed to provide first reference values of stiffness in terms of shear wave speed (SWS in m/s) and viscosity in terms of loss angle of complex shear modulus (ϕ in radians) of the zebrafish brain, neuroblastoma tumor, and muscle tissue.

Our study has 3 objectives: (1) demonstrate the feasibility of MRE in zebrafish, (2) provide initial reference values for the viscoelastic properties of zebrafish muscles and brains, and (3) outline the prospect of using zebrafish as a model for biomechanically oriented oncology research. To this end, we first used a soft-viscous phantom, which was previously characterized by tabletop MRE to validate our sequence and inversion technique. We then studied both wild-type and transgenic zebrafish using high-field MRE. In a final step, we performed a histopathological examination in comparison with the heterogeneities visible in MRE maps.

2 | METHODS

2.1 | Phantom

To test the setup and to determine optimal image resolution as well as SNR, we produced a simple ultrasound gel (Gello GmbH Geltechnik, Germany) phantom. The phantom consists of ultrasound gel packed into a glass cylinder of 4 mm inner diameter, analogous to the one used in the animal experiment. Both ends of the glass cylinder were sealed off with rubber plugs (1.5 mm thickness). Ultrasound gel provides a good MRI signal (with T_1/T_2 relaxation times of 2600 ± 50 ms/ 42 ± 2 ms at 7 Tesla) and

transmits shear waves well. Its homogeneity also allows the use of global fits to determine SWS and φ values instead of the more error prone inversion algorithms needed for heterogeneous media. To optimize MRE image resolution based on ground truth values, we predetermined the viscoelastic parameters of the phantom over a wide frequency range from 200 to 1400 Hz using compact tabletop MRE and Bessel fitting of wave data.³² This method was used previously as reference method for soft gel analysis in the desired frequency range.^{24,33,34}

2.2 | Animals

Animals used in this study were kept under controlled conditions at the Pediatric Department of Oncology/Hematology and Stem Cell Transplantation, Charité University Hospital, Berlin, Germany, under the licenses ZH76 and G0325/19 approved by the local animal ethics committee (Landesamt für Gesundheit und Soziales, Berlin, Germany) (G0325/19) and was conducted in accordance with the European Community Council Directive of November 24, 1986 (86/609/EEC). A total of 22 adult wild type zebrafish (Tüpfel Long Fin) and 18 transgenic zebrafish (Tg(dbh:MYCN;dbh:EGFP) were investigated.³¹ The final groups consisted of 15 wild type fish (median age: 19 months, mean age: 14 months, range: 2 to 24 months) and 11 MYCN-transgenic fish (median age: 23 months, mean age 14 months, range: 6 to 25 months) due to technical failures (oversized: 2 wild type, 5 transgenic fish; incorrect imaging parameter settings: 3 wild type, transgenic fish; insufficient shear wave amplitudes: 2 wild type, 1 transgenic fish). Before MRE, the fish were euthanized by hypothermal shock, as suggested by Wallace et al.³⁵ For MRI and MRE, the zebrafish were placed inside a glass cylinder of 4 mm inner diameter and embedded in ultrasound gel (Gello GmbH Geltechnik, Germany) to minimize tissue-air interfaces and susceptibility artifacts. Shear waves propagated into the fish by direct contact with the glass wall and through the ultrasound gel. The front end of the glass tube was sealed with a rubber plug (1.5 mm thickness).

2.3 | MRE actuator

Shear waves were induced through the walls of a cylindrical glass tube on which an air-cooled, nonmagnetic, piezoelectric actuator (ATA 200, Cedrat Technologies, France) was mounted. The main vibration direction was parallel to the cylinder axis to ensure that cylindrical shear waves with single polarization direction were predominantly

excited while compression waves were not excited or minimized by this geometry. This setup was designed to be similar to the vertical actuator of the MRE tabletop device but to allow excitation of waves in a horizontal orientation.³² The experimental setup is shown in Figure 1A. The actuator was driven by a function generator (CGC Instruments, Chemnitz, Germany) synchronized with the clock of the MRI scanner to avoid any latency between MRI and function generator while continuously vibrating the sample. Three vibration frequencies of 1000, 1200, and 1400 Hz were induced in consecutive experiments. All experiments were performed at $23 \pm 0.5^\circ\text{C}$.

2.4 | MRE image acquisition

All experiments were performed in a 7 Telsa preclinical MRI scanner (Bruker Biospec, Germany) equipped with a 5-mm bore, transverse electromagnetic, quadrature volume-resonator coil (Rapid Biomedical, Germany) shown in Figure 1. The MRE sequence was implemented using ParaVision 6.0.1 based on an existing spin-echo sequence that was sensitized to motion by including motion-encoding gradients of the same frequency, as used for mechanical vibrations. Motion-encoding gradients direction was along the main axis of the glass cylinder so that the predominant component of the cylindrical waves was encoded. Four dynamics of the wave cycle, evenly spaced over 1 vibration period, were encoded using a TE of 38 ms and a TR of 3000 ms. The motion-encoding gradients amplitude was 392 mT/m. Numbers of motion-encoding gradients periods were 14, 17, and 19, corresponding to 1000, 1200, and 1400 Hz vibration frequencies, respectively. Although this frequency range is too limited for analysis of viscoelastic dispersion in zebrafish tissue, previous work has shown that even minimal variation of excitation frequency enhances the stability of the inverse problems solution for the reconstruction of MRE maps using our k-MDEV (multifrequency dual elasto-visco) algorithm.^{36,37} For testing spatial resolution and SNR using the ultrasound gel phantom, matrix sizes of 100×100 , 67×67 , 50×50 , and 40×40 were used with a $4 \times 4 \text{ mm}^2$ FOV, resulting in in-plane pixel sizes of $40 \times 40 \mu\text{m}^2$, $60 \times 60 \mu\text{m}^2$, $80 \times 80 \mu\text{m}^2$, and $100 \times 100 \mu\text{m}^2$, respectively. Based on the results of the phantom experiment, we used the following parameters to measure the fish: 8 axial slices of $600 \mu\text{m}$ thickness, 67×67 matrix size, $4 \times 4 \text{ mm}^2$ FOV, and an in-plane resolution of $60 \times 60 \mu\text{m}^2$. The total acquisition time per frequency was approximately 16 min, and each fish was sampled from snout to swim bladder.

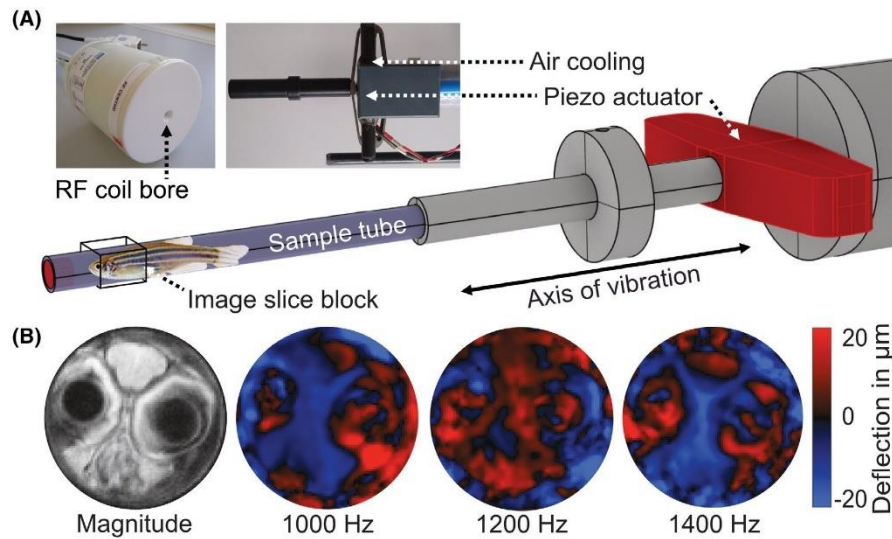


FIGURE 1 Setup for MRE of zebrafish in a 7T preclinical MRI scanner. (A) A piezoelectric actuation unit, shown in red, generates harmonic oscillations synchronized to the MRE sequence. The principal vibration direction is along the cylinder axis, which results in predominantly cylindrical waves. The box demarcates the area covered by the imaging slice slab. The custom volume resonator coil is also shown. (B) MRE magnitude image (grayscale) and wave images of different frequencies (color scale) showing the through-plane wave component, which was encoded by the sequence. MRE, MR elastography; T, tesla

2.5 | MRE data processing

After phase unwrapping and Fourier transformation across the 4 time steps over a wave cycle, the resulting complex-valued wave images at fundamental frequency. Examples shown in Figure 1B were reconstructed to maps of loss angle of complex shear modulus (φ in radian) using multifrequency dual elasto-visco (MDEV) inversion²⁹ and SWS using wave-number (k)-MDEV inversion.³⁰ The spatial bandpass filter of k-MDEV was adapted to the small field of view and minor impact of compression waves with our cylindrical actuator using a Butterworth filter of seventh order with 250/m threshold for the high pass. To facilitate comparison of values with the literature, we also tabulated shear stiffness in terms of the magnitude shear modulus $|G^*|$ assuming a material density ρ of 1000 kg/m³¹⁶:

$$|G^*| = \frac{SWS^2 \rho (1 + \cos\varphi)}{2}. \quad (1)$$

In ultrasound gel, SWS ground truth was determined by fitting Bessel functions as described previously.^{32,38,39} We consider Bessel function analysis of cylindrical waves as ground truth because it provides analytical solutions to the inverse problem in homogeneous media without artifact due to the dispersion-by-inversion bias.³⁸ Wave displacement SNR was

derived using the blind noise estimation method proposed by Donoho et al.⁴⁰ This method defines SNR as normalized log ratio of signal and median absolute deviation of the finest band of wavelet coefficients. The wavelet coefficients are calculated using Farras nearly symmetric filters.⁴¹ Both signal and noise are calculated only for regions of interest (ROI). Wavelet analysis is well suited for the differentiation of spatial frequencies of harmonic waves and noise in MRE, as shown previously.⁴² The method is implemented on an open access server for MRE data analysis (<https://bioqic-apps.charite.de>).

In zebrafish, φ and SWS maps were analyzed for sub-regional differences by manually delineating ROIs in the magnitude maps corresponding to the following anatomical regions: telencephalon, optic tectum, midbrain, cerebellum, whole brain, and skeletal muscle. Additionally, we defined ROIs over the neuroblastoma of the transgenic zebrafish.

2.6 | Histology

Immunohistochemistry was performed for intraorganismal orientation and special distribution of tumors immediately after MRE (approx. 1 h after death) in 2 formaldehyde-fixed paraffin-embedded whole mount zebrafish. Tyrosine hydroxylase (TH) is an enzyme found

in adrenergic tissues; therefore, it can be used as marker confirming the identity of the tumor.⁴³ To improve distribution of the fixative inside the tissue, 5 mm of the caudal fin was removed before the carcass was fixed in 4% paraformaldehyde in 1× phosphate buffered saline on a rocker for 48 h at 4°C. After fixation, paraformaldehyde was replaced by decalcification buffer (0.5 M EDTA, pH: 7.2), and fish were incubated on a rocker for 24 h at 4°C. The fish were paraffin-embedded and sectioned (12 μm) as described in Her et al.⁴⁴ Cancerous tissue was identified using a TH as well as hematoxylin and eosin staining. Prior to TH staining, sections were rehydrated with subsequent baths of 5 min each in xylene (2 times), 100% EtOH (2 times), and 70% EtOH. Sections were then rinsed in water and placed in TBS-T for 5 min. Slides were heated to approximately 90°C for 20 min in citrate buffer, incubated 1 h in blocking buffer and incubated overnight with primary antibody (anti-TH: Pel-Freeze, cat # P40101-150) at a dilution of 1:200. The next day, slides were rinsed with TBS-T and incubated for 1 h with secondary antibody (goat anti-rabbit IgG H&L, conjugated with Alexa 488 (abcam, cat# ab150077) at 1:500. Glass slides were mounted using an antifade mounting agent (ProLong Gold Antifade Mounting Agent, Invitrogen; cat# P36935) to seal and preserve the fluorescently labeled tissue. For hematoxylin and eosin staining, which stains nuclei in dark purple and extracellular matrix in pink, the following protocol was used: formaldehyde-fixed paraffin-embedded fish were dewaxed 5 min in xylene, then again for 10 min in fresh xylene, 5 min in 100% EtOH, 2 min in 80% EtOH, 2 min in 70% EtOH, and 2 times in H₂O for 1 min. Next, the tissue was then stained with Mayer hematoxylin for 5 min and rinsed for 5 min in running tap water. Differentiation (10 dips in 0.3% acid alcohol) and blueing (20 dips in 95% EtOH) steps were performed, and formaldehyde-fixed paraffin-embedded tissue was then stained with Eosin-Phloxine solution for 2 min and dehydrated with subsequent baths of 5 min in 95% EtOH, 100% EtOH (2 times), and xylene (2 times). Slides were covered with mounting agent (Eukitt quick-hardening mounting agent, Sigma-Aldrich; cat# 03989) and mounted on glass slides.

2.7 | Statistical analysis

We tested the significance of population differences using the Wilcoxon rank sum test using MatLab 9.8.0.1380330 (R2020a) Update 2 (MathWorks, Natick, MA). Multiple comparisons were done using a 1-way analysis of variance in conjunction with the Bonferoni method. Therefore, we first defined 3 groups: wild type fish, tumor-bearing fish, and the pooled cohort of all fish. We then determined if region values in the brain were different between group

1 (wild type) and 2 (tumor). Because no difference was found, we further analyzed nontumor regions in the pooled group. In group 2 (tumor), we separately analyzed regional differences between tumor tissue, muscle tissue, and brain tissue. To test correlations between SWS or φ values and age or tumor size, we used the Pearson correlation. We did not test for sex effects on MRE parameters. *p* Values less than .05 were considered to indicate statistically significant differences. Unless otherwise indicated, the SD is used as an error estimation.

3 | RESULTS

3.1 | Phantom experiments

Comparison of inversion-based mapping at different resolutions with ground truth acquired by tabletop MRE in a wider frequency range and global Bessel fitting is presented in Figure 2. In Figure 2A, we show unfiltered wave images acquired in the gel phantom for each frequency and resolution. Wave fit analysis using Bessel functions resulted in a mean SWS of 0.77 ± 0.09 m/s and a mean φ of 0.30 ± 0.08 rad, which we considered ground truth. We then compared both ground truths with the results of our processing pipeline and found good agreement across all frequencies and resolutions, as shown in Figure 2B. Albeit phantom MRE values were unaffected by resolution, the SNR for $40 \times 40 \mu\text{m}^2$ was significantly lower than that obtained by larger voxel sizes ($p < .05$). Henceforth, we chose a resolution of $60 \times 60 \mu\text{m}^2$ for all animal experiments to ensure a stable range of SNR unaffected by resolution. Figure 2C shows the results of both the SWS recovered by Bessel fit as well as SWS recovered by our k-MDEV pipeline (both at $60 \times 60 \mu\text{m}^2$) compared to independent measurements of the same material at our 0.5 Telsa tabletop MRE system. At the relevant frequencies, the results fall closely together, validating our approach. A $60 \times 60 \mu\text{m}^2$ resolution provided SNRs of 19 ± 5 , 21 ± 4 , and 21 ± 4 for 1000, 1200, and 1400 Hz, respectively, which was close to the phantom SNR reported in Ref. 24 despite the higher resolution used in the present study.

3.2 | Zebrafish MRE

Group mean vibration amplitudes in the brains were $9 \pm 6 \mu\text{m}$ at 1000 Hz, $10 \pm 8 \mu\text{m}$ at 1200 Hz, and $12 \pm 6 \mu\text{m}$ at 1400 Hz. Mean displacement SNR averaged over all analyzed ROIs was 14 ± 7 , 16 ± 7 , and 19 ± 7 for 1000, 1200, and 1400 Hz, respectively, which is higher than reported in the literature based on single-shot MRE.²⁴ Coronal SWS and φ maps of a 1-year-old zebrafish are shown in

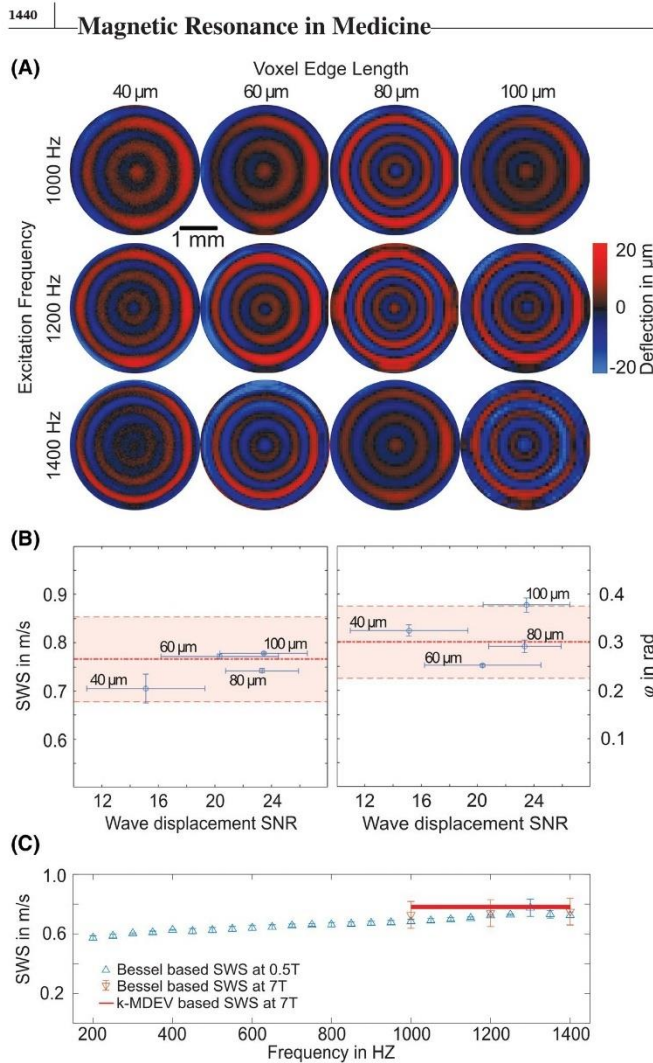


FIGURE 2 (A) Unfiltered wave images at different resolutions (columns) and frequencies (rows). (B) SWS (left) and φ (right) values determined by our processing pipeline plotted against wave displacement SNR. Bessel fits of the unfiltered complex-valued cylinder waves result in ground truths of $0.77 \text{ m/s} \pm 0.09 \text{ m/s}$ SWS and $0.30 \pm 0.08 \text{ rad}$ φ and are shown as dotted red line with SD as a shaded area. Both SWS values as well as φ determined by our pipeline fall within the ground truth for all resolutions. The percent error between the ground truth and the values at $60 \times 60 \mu\text{m}^2$ are 5% for the SWS and 10% for φ . (C) Comparison of tabletop MRE with 7T MRE both analyzed using frequency-resolved Bessel functions and frequency compounded k-MDEV inversion at $60 \times 60 \mu\text{m}^2$. Between 1000 and 1400 Hz, all measurements fall into the same SD range (thickness of the horizontal red line indicates SD). The percent error between the Bessel-based SWS at 7T and the k-MDEV based SWS was 5%, whereas the percent error between the Bessel-based SWS at 0.5T and the k-MDEV measurement was 9%. φ , loss angle; MDEV, multifrequency dual elastovisco; SWS, shear wave speed

Figure 3. Subregions of the brain, muscle, and tumor tissue can be identified in MRE maps, as indicated by the corresponding ROI boundaries, which are superimposed on the magnitude MRE images. To visualize the relative position of the MRE-slices, a composite microscopy image of a transgenic fish is shown overlaid with the approximate slice position, with green fluorescent protein marking the location of the tumor. Local, unphysical φ values greater than $\pi/2$ are most likely linked to inhomogeneities at tissue boundaries.⁴⁵

We observed no difference between brain regions of wild-type and tumor-bearing zebrafish. Henceforth, the results from both groups were pooled for group statistical analysis. SWS values were higher in the midbrain region

($3.1 \pm 0.7 \text{ m/s}$) than in the optic tectum ($2.6 \pm 0.5 \text{ m/s}$) and telencephalon ($2.6 \pm 0.5 \text{ m/s}$) ($p < .05$). φ values were lower in the cerebellum ($0.9 \pm 0.4 \text{ rad}$) than in the telencephalon ($1.4 \pm 0.2 \text{ rad}$) and optic tectum ($1.3 \pm 0.4 \text{ rad}$). We found no influence of age or tumor size on SWS or φ values in our fish using Pearson r ($p > .05$).

The sites of cancer cells identified by immunohistochemistry with TH antibody and hematoxylin and eosin staining agreed remarkably well with features visible in the SWS and φ maps, as shown in Figure 4. Comparing mean tumor values with muscle and brain tissue in the neuroblastoma-bearing fish, we found SWS and φ of cancerous tissue ($2.4 \pm 0.3 \text{ m/s}$, $0.7 \pm 0.1 \text{ rad}$) to be lower than those of skeletal muscle ($2.9 \pm 0.5 \text{ m/s}$, $1.4 \pm 0.2 \text{ rad}$)

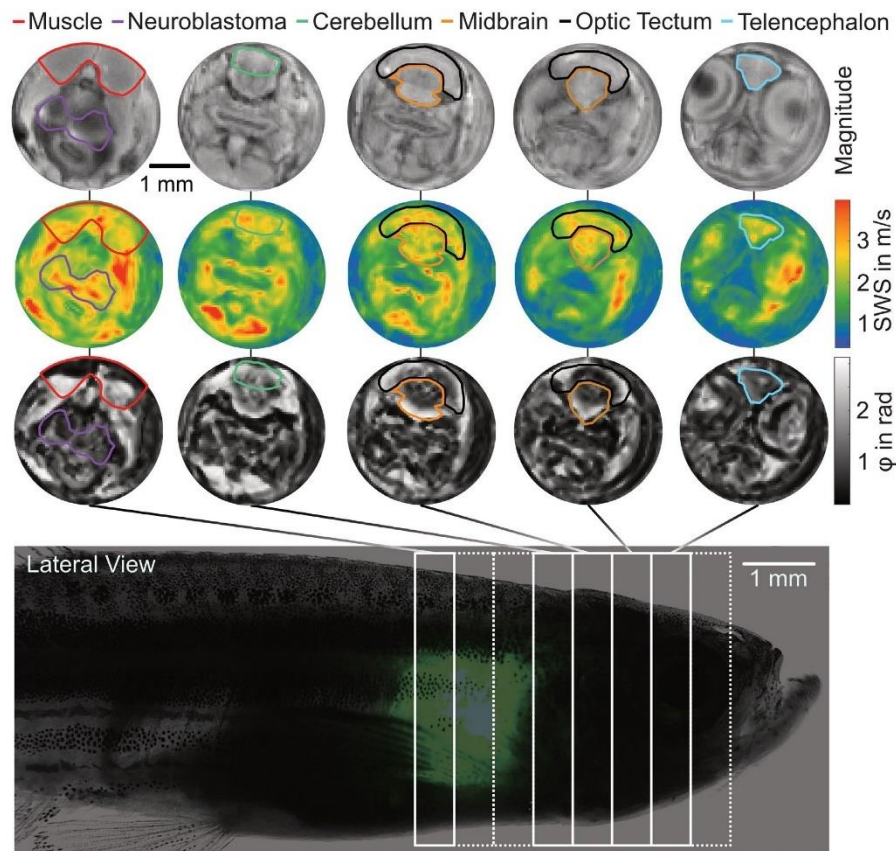


FIGURE 3 Representative data obtained in a transgenic zebrafish. The first row shows absolute wave magnitude maps, with coronal slices from posterior to anterior. SWS and φ maps of the respective slices are shown in the second and third rows, respectively. Anatomical regions relevant in our study are marked in all maps. The bottom row shows approximate slice positioning overlaid over a composite microscopy image of an anesthetized zebrafish that shows general anatomy, with GFP indicating the tumor through the semitransparent skin. GFP, green fluorescent protein

and brain tissue (2.9 ± 0.4 m/s, 1.2 ± 0.2 rad, all $p < .05$). Tumor volume based on multiple ROI was no confounder for SWS or loss angle. Group statistical data are plotted in Figure 5 and summarized in Table 1.

4 | DISCUSSION

To the best of our knowledge, this is the first study presenting spatially resolved maps of SWS and loss angle φ of the adult zebrafish. SWS is used in studies as a surrogate marker of stiffness.⁴⁶ Recently, SWS ranging from 2.5 to 5 m/s for frequencies of 300 to 500 Hz was found in anesthetized zebrafish, which is slightly above our results despite lower frequencies.¹⁴ However, the published values

do not account for the spatial heterogeneity of mechanical properties, as seen in our study, and reflect tissue properties in a central region of the fish not covered by our experiments.

Our results underline the great potential of MRE in generating viscoelasticity maps with a spatial resolution of $60 \mu\text{m}$, which to our knowledge is the highest resolution thus far reported for MRE parameter mapping. This high resolution was particularly favorable for investigating the heterogeneity of zebrafish anatomy by MRE. An interesting finding of our study is that stiffness is higher in the mesencephalon region than in the optic tectum, which could point to microstructural differences. For example, the optic tectum is characterized by the presence of fewer though better aligned neuronal fibers, whereas

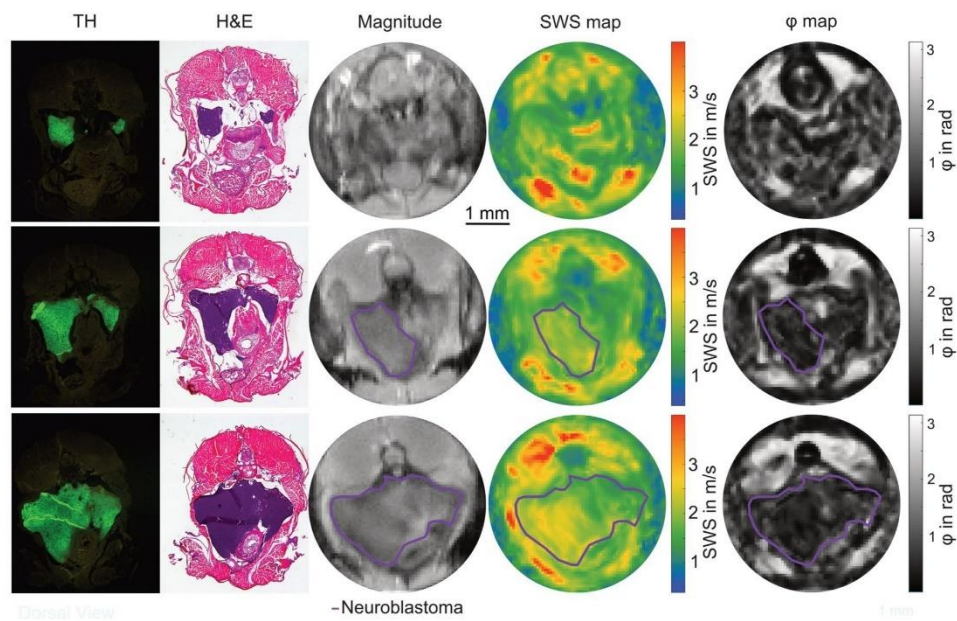


FIGURE 4 Comparison of SWS as well as φ maps and histology. TH and H&E staining reveal cancerous cells in green and purple, which can then be identified in the magnitude, SWS, and φ maps. Note the different thicknesses of the slices, with histology slices being significantly thinner ($<4 \mu\text{m}$) than MRE slices ($600 \mu\text{m}$). The cancerous region is marked in purple. H&E, hematoxylin and eosin; TH, tyrosine hydroxylase

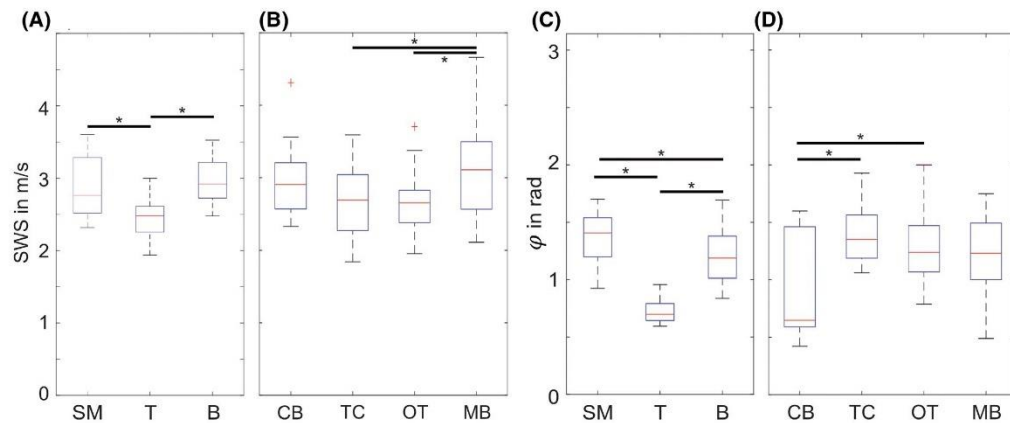


FIGURE 5 Group SWS (A,B) and loss angle values (C,D) for SM, T, B, CB, TC, OT, and MB. In (B) and (D), transgenic zebrafish and wild-type zebrafish were pooled, whereas (A) and (C) only show transgenic fish. Significant differences ($p < .05$) are indicated by asterisks. B, whole brain; CB, cerebellum; MB, midbrain; OT, optic tectum; SM, skeletal muscle; T, neuroblastoma; TC, telencephalon

the middle mesencephalon is dominated by distinct fibers and abundant fiber crossings, which might contribute to greater stiffness than in the optic tectum overall. Fish brain stiffness values seem to be similar to that of the murine brain as investigated by MRE in the same frequency

range,^{24,47–50} underscoring the viability of zebrafish as an animal model from a mechanical perspective. Another interesting finding of our experiments is that neuroblastoma tissue is markedly softer and less viscous than muscle and brain tissue. This suggests similar mechanical

TABLE 1 Shear wave speed loss angle and magnitude shear modulus of different tissue types in zebrafish

Region of Interest	SWS in m/s	φ in Rad	G* in kPa
<i>Transgenic fish only</i>			
Whole brain	2.9 ± 0.4	1.2 ± 0.2	5.7 ± 0.2
Skeletal muscle	2.9 ± 0.5	1.4 ± 0.2	4.9 ± 0.2
Neuroblastoma	2.4 ± 0.3	0.7 ± 0.1	5.0 ± 0.1
<i>All fish</i>			
Telencephalon	2.6 ± 0.5	1.4 ± 0.2	3.9 ± 0.3
Optic tectum	2.6 ± 0.5	1.3 ± 0.4	4.3 ± 0.2
Midbrain	3.1 ± 0.7	1.2 ± 0.3	6.5 ± 0.5
Cerebellum	2.9 ± 0.6	0.9 ± 0.4	6.8 ± 0.3

Note: Error is given as SD.

Abbreviations: φ , loss angle; G*, shear modulus; Rad, radian; SWS, shear wave speed.

properties of our tumor model as observed in invasively growing human brain tumors such as glioblastoma, which are characterized by a relatively low amount of collagen.⁵¹ This might provide a unique window into the soft signature of malignant tumor cells, which is typically masked by stiff properties of fibrous proteins in other tumors.⁵²

Comparing our methodology with other biomechanical methods underscores its relevance. Brillouin microscopy has revealed interesting details of mechanical phenomena during growth and repair of the spinal cord in zebrafish larvae with a microscopic resolution of up to 7 μm but cannot measure shear modulus.⁵³ Direct contact setups such as biocompatible cantilevers are able to measure mean total strain during the embryo stage and can be combined with finite-element analysis to estimate spatially resolved Young modulus, but they are invasive and rely on model assumptions.⁵⁴ Similarly, optical traps can be used to measure pointwise stiffness values.^{55,56} However, because this method is based on the deflecting responses off transparent beads, the invasive injection of foreign material is necessary, which might also change the elastic properties of the tissue. Another powerful method is scanning atomic force microscopy,⁵⁷ which, however, needs thin tissue slices and careful surface preparation, hindering its direct comparison with bulk parameters measured by MRE. Additionally, many methods exist to measure specific mechanical properties of individual parts of the fish, such as caudal fins,⁵⁸ heart sections,⁸ or neuromasts,⁵⁹ but these methods cannot easily be applied to heterogeneous tissues within the fish body as investigated in our study.

More experiments are needed to address viscoelastic dispersion and region-specific differences beyond those addressed in this paper. Another limitation is the small

number of zebrafish and their uneven age distribution. Finally, further technical developments are necessary to make MRE applicable to in vivo zebrafish. Similar to Refs. [14] and [60], MRE could be applied to anesthetized fish, which would greatly enhance the viability of the method in biomedical research. To further reduce acquisition time, frequencies could be acquired in a parallel fashion as proposed by Solanas et al.⁶¹ Nevertheless, this preliminary proof-of-concept study successfully adds the zebrafish to the group of disease models accessible by MRE and extends the resolution limit of multifrequency MRE to 60- μm voxel edge size.

5 | CONCLUSION

In summary, an MRE setup was developed for postmortem viscoelasticity mapping in zebrafish. High-resolution maps of SWS and loss angle were generated by multifrequency wave acquisition and inversion with an in-plane resolution of 60 μm . These maps revealed rich detail of viscoelastic heterogeneities across skeletal muscle tissue, brain, and a model neuroblastoma. Reference values of stiffness and viscosity were tabulated for brain subregions including the cerebellum, optic tectum, telencephalon, and mesencephalon. This study provides the basis for new applications of MRE in biomedical research using zebrafish disease models.

ACKNOWLEDGMENT


Open access funding enabled and organized by ProjektDEAL.

ORCID

Jakob Ernst Luis Jordan  <https://orcid.org/0000-0002-6081-7595>


Tom Meyer  <https://orcid.org/0000-0002-2171-6791>

Heiko Tzschätzsch  <https://orcid.org/0000-0001-9458-2221>


Anton Gauert  <https://orcid.org/0000-0002-3013-5374>


Helge Herthum  <https://orcid.org/0000-0001-6494-0833>

Leif Schröder  <https://orcid.org/0000-0003-4901-0325>

Jürgen Braun  <https://orcid.org/0000-0001-5183-7546>

Anja I. H. Hagemann  <https://orcid.org/0000-0001-5491-4607>

Ingolf Sack  <https://orcid.org/0000-0003-2460-1444>

Ingolf Sack  @bioqic

Ingolf Sack  @bioqic

TWITTER

Ingolf Sack  @bioqic

REFERENCES

1. Kinth P, Mahesh G, Panwar Y. Mapping of zebrafish research: a global outlook. *Zebrafish*. 2013;10:510-517.

2. Varga M. The doctor of delayed publications: the remarkable life of George Streisinger (1927-1984). *Zebrafish*. 2018;15:314-319.
3. Hagemann AIH, Kurz J, Kauffeld S, et al. In-vivo analysis of formation and endocytosis of the Wnt/ β -Catenin signaling complex in zebrafish embryos. *J Cell Sci*. 2014;127:3970-3982.
4. Gauert A, Olk N, Pimentel-Gutierrez H, et al. In vivo model for drug-response prediction in patients with B-cell precursor acute lymphoblastic leukemia. *Cancers (Basel)*. 2020;12:1883.
5. Marques JJ, Lupi E, Mercader N. Model systems for regeneration: zebrafish. *Development*. 2019;146:18.
6. Lammer E, Carr GJ, Wendler K, Rawlings JM, Belanger SE, Braunbeck T. Is the fish embryo toxicity test (FET) with the zebrafish (*Danio rerio*) a potential alternative for the fish acute toxicity test? *Comp Biochem Physiol C Toxicol Pharmacol*. 2009;149:196-209.
7. Howe K, Clark MD, Torroja CF, et al. The zebrafish reference genome sequence and its relationship to the human genome. *Nature*. 2013;496:498-503.
8. Yu JK, Sarathchandra P, Chester A, Yacoub M, Brand T, Butcher JT. Cardiac regeneration following cryoinjury in the adult zebrafish targets a maturation-specific biomechanical remodeling program. *Sci Rep*. 2018;8:15661.
9. Xiao J, Glasgow E, Agarwal S. Zebrafish xenografts for drug discovery and personalized medicine. *Trends Cancer*. 2020;6:569-579.
10. Spanjaard B, Hu B, Mitic N, et al. Simultaneous lineage tracing and cell-type identification using CRISPR-Cas9-induced genetic scars. *Nat Biotechnol*. 2018;36:469-473.
11. Holler K, Junker JP. RNA tomography for spatially resolved transcriptomics (Tomo-seq). In: Pelegri FJ, ed. *Vertebrate Embryogenesis: Embryological, Cellular, and Genetic Methods*. 2nd ed. Humana Press; 2019: 129-141.
12. Träber N, Uhlmann K, Girardo S, et al. Polyacrylamide bead sensors for in vivo quantification of cell-scale stress in zebrafish development. *Sci Rep*. 2019;9:17031.
13. Hörner F, Meissner R, Polali S, et al. Holographic optical tweezers-based in vivo manipulations in zebrafish embryos. *J Biophotonics*. 2017;10:1492-1501.
14. Zhang XM, Zhang AX, Zhou BR, Xu XL. A feasibility study for noninvasive measurement of shear wave speed in live zebrafish. *Ultrasonics*. 2020;107:106170.
15. Muthupillai R, Ehman RL. Magnetic resonance elastography. *Nature Med*. 1996;2:601-603.
16. Hirsch S, Braun J, Sack I. *Magnetic Resonance Elastography: Physical Background and Medical Applications*. Wiley-VCH; 2017.
17. Majumdar S, Klatt D. Longitudinal study of sub-regional cerebral viscoelastic properties of 5XFAD Alzheimer's disease mice using multifrequency MR elastography. *Magn Reson Med*. 2021;86:405-414.
18. Liu Y, Royston TJ, Klatt D, Lewandowski ED. Cardiac MR elastography of the mouse: initial results. *Magn Reson Med*. 2016;76:1879-1886.
19. Pagé G, Tardieu M, Gennisson JL, Besret L, Garteiser P, Van Beers BE. Tumor solid stress: assessment with MR elastography under compression of patient-derived hepatocellular carcinomas and cholangiocarcinomas xenografted in mice. *Cancers (Basel)*. 2021;13:1891.
20. Li J, Zormpas-Petridis K, Boulton JKR, et al. Investigating the contribution of collagen to the tumor biomechanical phenotype with noninvasive magnetic resonance elastography. *Cancer Res*. 2019;79:5874-5883.
21. Guertler CA, Okamoto RJ, Schmidt JL, Badachhapa AA, Johnson CL, Bayly PV. Mechanical properties of porcine brain tissue in vivo and ex vivo estimated by MR elastography. *J Biomech*. 2018;69:10-18.
22. Feng Y, Clayton EH, Chang Y, Okamoto RJ, Bayly PV. Viscoelastic properties of the ferret brain measured in vivo at multiple frequencies by magnetic resonance elastography. *J Biomech*. 2013;46:863-870.
23. Bertalan G, Klein C, Schreyer S, et al. Biomechanical properties of the hypoxic and dying brain quantified by magnetic resonance elastography. *Acta Biomater*. 2020;101:395-402.
24. Bertalan G, Guo J, Tzschätzsch H, et al. Fast tomoelelastography of the mouse brain by multifrequency single-shot MR elastography. *Magn Reson Med*. 2019;81:2676-2687.
25. Guo J, Bertalan G, Meierhofer D, et al. Brain maturation is associated with increasing tissue stiffness and decreasing tissue fluidity. *Acta Biomater*. 2019;99:433-442.
26. Ronot M, Lambert SA, Wagner M, et al. Viscoelastic parameters for quantifying liver fibrosis: three-dimensional multifrequency MR elastography study on thin liver rat slices. *PLoS One*. 2014;9:e94679.
27. Zhu B, Wei L, Rotile N, et al. Combined magnetic resonance elastography and collagen molecular magnetic resonance imaging accurately stage liver fibrosis in a rat model. *Hepatology*. 2017;65:1015-1025.
28. Othman SF, Xu H, Royston TJ, Magin RL. Microscopic magnetic resonance elastography (microMRE). *Magn Reson Med*. 2005;54:605-615.
29. Papazoglou S, Hirsch S, Braun J, Sack I. Multifrequency inversion in magnetic resonance elastography. *Phys Med Biol*. 2012;57:2329-2346.
30. Tzschätzsch H, Guo J, Dittmann F, et al. Tomoelelastography by multifrequency wave number recovery from time-harmonic propagating shear waves. *Med Image Anal*. 2016;30:1-10.
31. Tao T, Sondalle SB, Shi H, et al. The pre-rRNA processing factor DEF is rate limiting for the pathogenesis of MYCN-driven neuroblastoma. *Oncogene*. 2017;36:3852-3867.
32. Braun J, Tzschätzsch H, Korting C, et al. A compact 0.5 T MR elastography device and its application for studying viscoelasticity changes in biological tissues during progressive formalin fixation. *Magn Reson Med*. 2018;79:470-478.
33. Zampini MA, Guidetti M, Royston TJ, Klatt D. Measuring viscoelastic parameters in Magnetic Resonance Elastography: a comparison at high and low magnetic field intensity. *J Mech Behav Biomed Mater*. 2021;120:104587.
34. Sauer F, Oswald L, Ariza de Schellenberger A, et al. Collagen networks determine viscoelastic properties of connective tissues yet do not hinder diffusion of the aqueous solvent. *Soft Matter*. 2019;15:3055-3064.
35. Wallace CK, Bright LA, Marx JO, Andersen RP, Mullins MC, Carty AJ. Effectiveness of rapid cooling as a method of euthanasia for young zebrafish (*Danio rerio*). *J Am Assoc Lab Anim Sci*. 2018;57:58-63.
36. Li M, Guo J, Hu P, et al. Tomoelelastography based on multifrequency MR elastography for prostate cancer detection: comparison with multiparametric MRI. *Radiology*. 2021;299:201852.
37. Herthum H, Shahryari M, Tzschätzsch H, et al. Real-time multifrequency MR elastography of the human brain reveals rapid

- changes in viscoelasticity in response to the Valsalva Maneuver. *Front Bioeng Biotechnol.* 2021;9:666456.
38. Mura J, Schrank F, Sack I. An analytical solution to the dispersion-by-inversion problem in magnetic resonance elastography. *Magn Reson Med.* 2020;84:61-71.
 39. Okamoto RJ, Clayton EH, Bayly PV. Viscoelastic properties of soft gels: comparison of magnetic resonance elastography and dynamic shear testing in the shear wave regime. *Phys Med Biol.* 2011;56:6379-6400.
 40. Donoho DL, Johnstone IM, Kerkycharian G, Picard D. Wavelet shrinkage: asymptopia? *J R Stat Soc Series B-Methodol.* 1995;57:301-337.
 41. Abdelnour AF, Selesnick IW. Nearly symmetric orthogonal wavelet bases. In *Proceedings of the IEEE International Conference on Acoustics, Speech, & Signal Processing (ICASSP)*, Salt Lake City, UT, May 2001.
 42. Barnhill E, Hollis L, Sack I, et al. Nonlinear multiscale regularisation in MR elastography: towards fine feature mapping. *Med Image Anal.* 2017;35:133-145.
 43. Reynolds CP, Biedler JL, Spengler BA, et al. Characterization of human neuroblastoma cell lines established before and after therapy. *J Natl Cancer Inst.* 1986;76:375-387.
 44. Her ZP, Yeo KS, Howe C, Levee T, Zhu S. Zebrafish model of neuroblastoma metastasis. *J Vis Exp.* 2021. doi:10.3791/62416
 45. Dittmann F, Hirsch S, Tzschatsch H, Guo J, Braun J, Sack I. In vivo wideband multifrequency MR elastography of the human brain and liver. *Magn Reson Med.* 2016;76:1116-1126.
 46. Manduca A, Bayly PJ, Ehman RL, et al. MR elastography: principles, guidelines, and terminology. *Magn Reson Med.* 2021;85:2377-2390.
 47. Clayton EH, Garbow JR, Bayly PV. Frequency-dependent viscoelastic parameters of mouse brain tissue estimated by MR elastography. *Phys Med Biol.* 2011;56:2391-2406.
 48. Boulet T, Kelso ML, Othman SF. Long-term in vivo imaging of viscoelastic properties of the mouse brain after controlled cortical impact. *J Neurotrauma.* 2013;30:1512-1520.
 49. Schregel K, Wuerfel E, Garteiser P, et al. Demyelination reduces brain parenchymal stiffness quantified in vivo by magnetic resonance elastography. *Proc Natl Acad Sci U S A.* 2012;109:6650-6655.
 50. Jamin Y, Boulton JK, Li J, et al. Exploring the biomechanical properties of brain malignancies and their pathologic determinants in vivo with magnetic resonance elastography. *Cancer Res.* 2015;75:1216-1224.
 51. Streitberger KJ, Lilaj L, Schrank F, et al. How tissue fluidity influences brain tumor progression. *Proc Natl Acad Sci U S A.* 2020;117:128-134.
 52. Plodinec M, Loparic M, Monnier CA, et al. The nanomechanical signature of breast cancer. *Nat Nanotechnol.* 2012;7:757-765.
 53. Schlussler R, Mollmert S, Abuhattum S, et al. Mechanical mapping of spinal cord growth and repair in living zebrafish larvae by Brillouin imaging. *Biophys J.* 2018;115:911-923.
 54. Tomizawa Y, Dixit K, Daggett D, Hoshino K. Biocompatible cantilevers for mechanical characterization of zebrafish embryos using image analysis. *Sensors (Basel).* 2019;19:1506.
 55. Staunton JR, Blehm B, Devine A, Tanner K. In situ calibration of position detection in an optical trap for active microrheology in viscous materials. *Opt Express.* 2017;25:1746-1761.
 56. Blehm BH, Devine A, Staunton JR, Tanner K. In vivo tissue has non-linear rheological behavior distinct from 3D biomimetic hydrogels, as determined by AMOTIV microscopy. *Biomaterials.* 2016;83:66-78.
 57. Möllmert S, Kharlamova MA, Hoche T, et al. Zebrafish spinal cord repair is accompanied by transient tissue stiffening. *Biophys J.* 2020;118:448-463.
 58. Puri S, Aegerter-Wilmsen T, Jaźwińska A, Aegerter CM. In vivo quantification of mechanical properties of caudal fins in adult zebrafish. *J Exp Biol.* 2018;221:jeb171777.
 59. McHenry MJ, van Netten SM. The flexural stiffness of superficial neuromasts in the zebrafish (*Danio rerio*) lateral line. *J Exp Biol.* 2007;210:4244-4253.
 60. Kabli S, Spaink HP, De Groot HJ, Alia A. In vivo metabolite profile of adult zebrafish brain obtained by high-resolution localized magnetic resonance spectroscopy. *J Magn Reson Imaging.* 2009;29:275-281.
 61. Sango Solanas P, Tse Ve Koon K, Ratiney H, Millioz F, Causy C, Beuf O. Harmonic wideband simultaneous dual-frequency MR Elastography. *NMR Biomed.* 2021;34:e4442.

How to cite this article: Jordan JEL, Bertalan G, Meyer T, et al. Microscopic multifrequency MR elastography for mapping viscoelasticity in zebrafish. *Magn Reson Med.* 2022;87:1435-1445. doi:10.1002/mrm.29066

List of publications

Publication 1: C. Bayerl, Y. Safraou, R. Reiter, V. Proß, K. Lehmann, A.A. Kühl, M. Shahryari, B. Hamm, I. Sack, M.R. Makowski, J. Braun, P. Asbach. Investigation of hepatic inflammation via viscoelasticity at low and high mechanical frequencies-A magnetic resonance elastography study. *Journal of the Mechanical Behavior of Biomedical Materials*, 160 (2024) 106711. Impact Factor 3.6

<https://doi.org/10.1016/j.jmbbm.2024.106711>

Publication 2: J. Braun, J. Bernarding, J. Snelings, T. Meyer, P.A. Dantas de Moraes, Y. Safraou, R.G., Wells, J. Guo, H. Tzschätzsch, A. Zappe, K. Pagel, I.M Sauer, K.H. Hillebrandt, I. Sack. On the relationship between viscoelasticity and water diffusion in soft biological tissues. *Acta Biomaterialia* (2024). Impact Factor 9.7

<https://doi.org/10.1016/j.actbio.2024.05.007>

Publication 3: J. Guo, K. Krehl, Y. Safraou, I. Wallach, J. Braun, D. Meierhofer, I. Sack, N. Berndt. Pregnancy alters fatty acid metabolism, glucose regulation, and detoxification of the liver in synchrony with biomechanical property changes. *Heliyon* (2024) 10(20). Impact Factor 3.4

<https://doi.org/10.1016/j.heliyon.2024.e39674>

Publication 4: T. Meyer, M. Anders, A.Z. Pietzcker, M. Doyley, S. Gröner, O. Böhm, P. Engl, Y. Safraou, J. Braun, I. Sack, H. Tzschätzsch. Rapid wideband characterization of viscoelastic material properties by Bessel function-based time harmonic ultrasound elastography (B-THE). *Journal of the Mechanical Behavior of Biomedical Materials* (2024) 160, 106746. Impact Factor 3.6

<https://doi.org/10.1016/j.jmbbm.2024.106746>

Publication 5: Y. Safraou, K. Krehl, T. Meyer, S. Mehrgan, J.E.L. Jordan, H. Tzschätzsch, T. Fischer, P. Asbach, J. Braun, I. Sack, J. Guo, The influence of static portal pressure on liver biophysical properties, *Acta Biomaterialia* 169 (2023) 118-129.

<https://doi.org/10.1016/j.actbio.2023.07.033>

Publication 6: M. Shahryari, S. Keller, D. Meierhofer, I. Wallach, Y. Safraou, J. Guo, S.R. Marticorena Garcia, J. Braun, M.R. Makowski, I. Sack, N. Berndt, On the relationship between metabolic capacities and in vivo viscoelastic properties of the liver, *Frontiers in Bioengineering and Biotechnology* 10 (2023) 1042711.

<https://doi.org/10.3389/fbioe.2022.1042711>

Publication 7: J.E.L. Jordan, G. Bertalan, T. Meyer, H. Tzschätzsch, A. Gauert, L. Bramè, H. Herthum, **Y. Safraou**, L. Schröder, J. Braun, Microscopic multifrequency MR elastography for mapping viscoelasticity in zebrafish, *Magnetic Resonance in Medicine* 87(3) (2022) 1435-1445.

<https://doi.org/10.1002/mrm.29066>

Curriculum Vitae

My curriculum vitae does not appear in the electronic version of my thesis for reasons of data protection.

My curriculum vitae does not appear in the electronic version of my thesis for reasons of data protection.

My curriculum vitae does not appear in the electronic version of my thesis for reasons of data protection.

Acknowledgments

My journey through the Ph.D. program within the Elastography Research Group under the guidance of Professor Sack has been an exceptionally rewarding experience, surpassing all my expectations. I would like to express heartfelt gratitude to all those who have been crucial in shaping this remarkable learning journey.

First and foremost, I am deeply grateful to Professor Sack for granting me the opportunity to join his group, his unwavering confidence and support throughout my Ph.D. studies. I am profoundly grateful to Professor Jing Guo for instilling invaluable work ethics, perseverance, and scientific rigour through our close collaboration. Special gratitude is also due to Professor Tzschätzsch and Dr Braun for their indispensable supervision, which proved to be pivotal in the advancement of my research.

I would like to express my sincere appreciation to my colleagues in the MR Elastography group. The collaborative efforts of Anna, Bernhard, Biru, Carsten, Chiara, Helge, Judith, Karolina, Kristin, Ledia, Mahsa, Matthias, Mehrgan, Noah, Pedro, Stefan, and Steffen have greatly enriched my academic journey. I would be remiss not to express my deepest gratitude to Tom and Jakob, whose unwavering support and friendship created an exceptional working environment that spurred my progress.

I am deeply indebted to my beloved family in Tunis and Germany for their unwavering love and support. My heartfelt thanks go to my remarkable and loving family: my father, Khaled, mother, Faiza, and brother, Dali, whose endless encouragement has propelled me forward at every stage of my education.

Finally, I express my profound gratitude to my partner, Robert, whose unfailing support, and commitment have been my anchor throughout these transformative years.

Thank you all!